

VRIJE  
UNIVERSITEIT  
BRUSSEL

<sup>1</sup> **A search for flavour changing neutral currents  
2 involving a top quark and a Z boson, using the  
3 data collected by the CMS collaboration at a  
4 centre-of-mass energy of 13 TeV**

<sup>5</sup> Isis Van Parijs

<sup>6</sup> Proefschrift ingediend met het oog op het behalen van de academische graad  
<sup>7</sup> Doctor in de Wetenschappen.

Published in Faculteit Wetenschappen & Bio-ingenieurswetenschappen  
Vrije Universiteit Brussel  
At 10 November 2017.

<sup>8</sup>

Responsible Contact: Isis Van Parijs  
Intitute for High Energy Physics  
Promotor: Prof. Jorgen D'Hondt

9 First Referee: Prof. Dr. J. D'Hondt  
Date of Hand-in: 10 November 2017  
Date of Defense: 10 December 2017

# Contents

---

11	<b>1 Theoretical basis</b>	1
12	1.1 Elementary particles and forces . . . . .	1
13	1.2 Standard Model Lagrangian, connecting fields with particles . . . . .	2
14	1.3 Flavours in the SM . . . . .	5
15	1.4 The top quark in the SM . . . . .	6
16	1.5 Effective field theories . . . . .	10
17	1.6 Motivation for new physics . . . . .	14
18	1.7 An effective approach beyond the SM: FCNC involving a top quark . . . . .	15
19	1.8 Experimental constraints on top-FCNC . . . . .	18
20	<b>2 Experimental set-up</b>	23
21	2.1 The Large Hadron Collider . . . . .	23
22	2.2 The Compact Muon Solenoid . . . . .	27
23	2.2.1 CMS coordinate system . . . . .	27
24	2.2.2 Towards the heart of CMS . . . . .	28
25	2.2.3 Data acquisition . . . . .	37
26	2.2.4 Phase 1 upgrades . . . . .	37
27	2.2.5 CMS computing model . . . . .	39
28	<b>3 Analysis techniques</b>	41
29	3.1 Hadron collisions at high energies . . . . .	41
30	3.2 Event generation . . . . .	44
31	3.2.1 Fundamentals of simulating a proton collision . . . . .	44
32	3.2.2 Programs for event generation . . . . .	44
33	3.2.3 Generating FCNC top-Z interactions . . . . .	46
34	3.2.4 Generating SM background events . . . . .	48
35	3.3 Multivariate analysis techniques: Boosted Decision Trees . . . . .	50
36	3.4 Statistical methodology . . . . .	52
37	<b>4 Event reconstruction and identification</b>	55
38	4.1 Object Reconstruction . . . . .	55
39	4.1.1 Charged particle tracks . . . . .	57
40	4.1.2 Following the Muon's Footsteps . . . . .	57
41	4.1.3 The path of the Electron . . . . .	57

42	4.1.4 Primary Vertex Reconstruction . . . . .	58
43	4.1.5 Calorimeter clusters . . . . .	58
44	4.2 Particle flow identification . . . . .	59
45	4.3 Pileup mitigation and luminosity measurement . . . . .	59
46	4.4 Physics object reconstruction and identification . . . . .	60
47	4.4.1 Muons . . . . .	60
48	4.4.2 Electrons . . . . .	62
49	4.4.3 Jets . . . . .	63
50	4.4.4 Jets from b fragmentation . . . . .	66
51	4.4.5 Missing transverse energy . . . . .	69
52	4.5 Summary of corrections . . . . .	69
53	<b>5 Event selection and categorisation</b>	<b>71</b>
54	5.1 Baseline event selection and filters . . . . .	71
55	5.1.1 Event cleaning . . . . .	74
56	5.1.2 Estimation of the trigger efficiency . . . . .	76
57	5.1.3 Corrections . . . . .	77
58	5.2 Analysis Strategy . . . . .	82
59	5.3 Data driven NPL background simulation . . . . .	82
60	5.4 Regions and channels . . . . .	83
61	5.4.1 WZ control region . . . . .	85
62	5.4.2 TTCR and STCR . . . . .	86
63	5.4.3 TTSR and STSR . . . . .	87
64	<b>6 The search for FCNC involving a top quark and a Z boson</b>	<b>89</b>
65	6.1 Construction of template distributions . . . . .	89
66	6.2 Systematic uncertainties . . . . .	89
67	6.3 Limit setting procedure . . . . .	89
68	6.4 Result and discussion . . . . .	89
69	<b>7 Denouement of the top-Z FCNC hunt at 13 TeV</b>	<b>91</b>
70	<b>Appendices</b>	<b>91</b>
71	<b>A Trigger scale factors</b>	<b>93</b>
72	<b>B Dilepton controlplots</b>	<b>105</b>
73	<b>C Statistical independent regions</b>	<b>107</b>
74	<b>Bibliography</b>	<b>109</b>

# Theoretical basis

# 1

---

76 The Standard Model (SM) [1] is a name given in the 1970s to a theory describing the fun-  
 77 damental particles and their interactions. This quantum field theory describes the particles  
 78 and their interactions as fields and has successfully incorporated three of the four fundamental  
 79 forces in the universe. In [Section 1.1](#), the particle content of the SM is summarised, while  
 80 [Section 1.2](#) describes the SM Lagrangian and its symmetries. In [Section 1.3](#), the flavour content  
 81 of the SM is highlighted, and [Section 1.4](#) focusses on the top quark in the SM.

82 The successful theory of the SM has some shortcomings which are discussed in [Section 1.6](#)  
 83 and lead to searches for a more general theory. One of such is using an effective field theory  
 84 (EFT) approach [2] to search for new physics in a model independent way. In [Section 1.7](#) an  
 85 EFT model focussing on flavour changing neutral currents (FCNC) involving a top quark is  
 86 presented. Its current experimental constraints are given in [Section 1.8](#).

## 87 1.1 Elementary particles and forces

88 The interactions in nature can be described by four forces, the strong force, the electromagnetic  
 89 (EM) force, the weak force and the gravitational force. These interactions happen via particles  
 90 with an integer spin known as bosons. The strong interaction is mediated by eight gluons  $g$ ,  
 91 while the electromagnetic force is mediated by photons  $\gamma$ , and the weak force by  $Z$  and  $W^\pm$   
 92 bosons. In [Table 1.1](#), the forces and their characteristics are shown. The gravitational force is  
 93 the only force not included in the SM and can be neglected for energies lower than the Planck  
 scale ( $1.22 \times 10^{19}$  GeV).

**Table 1.1:** The four forces of nature and their characteristics.

	Range	Mediator
Strong force	$10^{-15}$ m	8 gluons
Electromagnetic force	$\infty$	photon
Weak force	$10^{-18}$ m	$W^\pm$ , Zbosons
Gravitational force	$\infty$	unknown

The fermions are the particles that make up the visible matter in the universe. They carry half integer spin and can be subdivided into leptons and quarks, where leptons do not interact strongly. Each fermion has a corresponding anti-fermion which has the same mass and is oppositely charged. The electron  $e$  is the first elementary particle discovered [3] and belongs to the first generation of leptons together with the electron neutrino  $\nu_e$ . The second generation comprises the muon  $\mu$  and muon neutrino  $\nu_\mu$ , whereas the third generation consists of the tau  $\tau$  and tau neutrino  $\nu_\tau$ . The neutrinos are neutral particles, while the other leptons have charge  $\pm q_e$  with  $q_e$  representing the elementary charge of  $1.602 \times 10^{-19}$  C. The masses of charged leptons differ by four orders of magnitude between the first and third generations. In the SM the neutrinos are assumed to be massless, nonetheless it is experimentally established that neutrinos do have a tiny non-zero mass [4, 5]. In Table 1.2, the leptons and their properties in the SM are summarised.

**Table 1.2:** The properties of the leptons in the three generations of the SM [6], where  $q_e$  represents the elementary charge.

Generation	Particle	Mass	Charge
First	$e^-$	0.511 MeV	$-q_e$
	$\nu_e$	$\approx 0$	0
Second	$\mu^-$	106 MeV	$-q_e$
	$\nu_\mu$	$\approx 0$	0
Third	$\tau^-$	1 777 MeV	$-q_e$
	$\nu_\tau$	$\approx 0$	0

106

The quarks can also be divided into three generations. Unlike the leptons, they carry colour charge and can interact via the strong interaction. The top quark, discovered in 1995 at the Tevatron [7, 8], is the heaviest SM particle with a mass<sup>1</sup> measured to be  $173.34 \pm 0.27(\text{stat}) \pm 0.71(\text{syst})$  GeV [9]. The quarks and their properties are summarised in Table 1.3. In nature, only colour neutral objects can exist. This has as consequence that quarks are bound through gluons into mesons (quark+anti-quark) and baryons (three quarks). These mesons and baryons are mostly short-lived and unstable particles that rapidly decay through  $W^\pm$  and  $Z$  bosons. The only known stable baryon is the proton, made up of two up quarks and one down quark.

The scalar boson, commonly known as the Higgs boson, is the last piece of the SM discovered in 2012 [10, 11]. It is responsible for the masses of the  $W^\pm$  and Z boson, and that of the fermions.

## 118 1.2 Standard Model Lagrangian, connecting fields with particles

The SM is a quantum field theory and thus describes the dynamics and kinematics of particles and forces by a Lagrangian  $\mathcal{L}$ . The theory is based on the  $SU(3)_C \times SU(2)_L \times U(1)_Y$  gauge symmetry, where  $SU(2)_L \times U(1)_Y$  describes the electroweak interaction and  $SU(3)_C$  the strong

---

<sup>1</sup>In this thesis all masses and energies are expressed in natural units, where the speed of light and  $\hbar$  are taken to be equal to one.

**Table 1.3:** The properties of the quarks in the three generations of the SM [6], where  $q_e$  represents the elementary charge.

	Generation	Particle	Mass	Charge
First	up u	$2.2^{+0.6}_{-0.4}$ MeV	$\frac{2}{3} q_e$	
	down d	$4.7^{+0.5}_{-0.4}$ MeV	$\frac{-1}{3} q_e$	
Second	charm c	$1.28 \pm 0.03$ GeV	$\frac{2}{3} q_e$	
	strange s	$96^{+8}_{-4}$ MeV	$\frac{-1}{3} q_e$	
Third	top t	$173.1 \pm 0.6$ GeV	$\frac{2}{3} q_e$	
	bottom b	$4.18^{+0.04}_{-0.03}$ GeV	$\frac{-1}{3} q_e$	

interaction. The indices refer to colour C, the left chiral nature of the  $SU(2)_L$  coupling L, and the weak hypercharge Y. Its Lagrangian is constructed such that contains symmetries representing physics conservation laws such as conservation of energy, momentum and angular momentum. The symmetries under local gauge transformations are sustained by demanding gauge invariance<sup>2</sup>.

The  $U(1)_Y$  group has one generator Y with an associated gauge field  $B_\mu$ . The three gauge fields  $W_\mu^1$ ,  $W_\mu^2$ , and  $W_\mu^3$ , are associated to  $SU(2)_L$  with three generators that can be written as half of the Pauli matrices:

$$T_1 = \frac{1}{2} \begin{pmatrix} 0 & 1 \\ 1 & 0 \end{pmatrix}, \quad T_2 = \frac{1}{2} \begin{pmatrix} 0 & -i \\ i & 0 \end{pmatrix}, \quad \text{and} \quad T_3 = \frac{1}{2} \begin{pmatrix} 1 & 0 \\ 0 & -1 \end{pmatrix}. \quad (1.1)$$

The generators  $T^a$  satisfy the Lie algebra:

$$[T_a, T_b] = i\epsilon_{abc} T^c \text{ and } [T_a, Y] = 0, \quad (1.2)$$

where  $\epsilon_{abc}$  is an antisymmetric tensor. The gauge fields of  $SU(2)_L$  only couple to left-handed fermions as required by the observed parity violating nature of the weak force. The  $SU(3)_C$  group represents quantum chromodynamics (QCD). It has eight generators corresponding to eight gluon fields  $G_\mu^{1\dots 8}$ . Unlike  $SU(2)_L \times U(1)_Y$ ,  $SU(3)_C$  is not chiral.

Under  $SU(3)_C$  quarks are colour triplets while leptons are colour singlets. This implies that the quarks carry a colour index ranging between one and three, whereas leptons do not take part in strong interactions. Based on the chirality, the quarks and leptons are organized in doublets or singlets. Each generation  $i$  of fermions consists of left-handed doublets and right-handed singlets:

$$l_{L,i} = \begin{pmatrix} e_{L,i} \\ \nu_{L,i} \end{pmatrix}, \quad e_{R,i}, \quad q_{L,i} = \begin{pmatrix} u_{L,i} \\ d_{L,i} \end{pmatrix}, \quad u_{R,i}, \quad \text{and} \quad d_{R,i} \quad (1.3)$$

The SM Lagrangian can be decomposed as a sum of four terms

$$\mathcal{L}_{SM} = \mathcal{L}_{gauge} + \mathcal{L}_f + \mathcal{L}_{Yuk} + \mathcal{L}_\phi, \quad (1.4)$$

<sup>2</sup>Different field configurations of unobservable fields can result in identical quantities. Transformations between such configurations are called gauge transformation and the absence of change in the measurable quantities is a characteristic called gauge invariance.

that are related to the gauge, fermion, Yukawa and scalar sectors. The gauge Lagrangian regroups the gauge fields of all three symmetry groups, and the fermionic part consists of kinetic energy terms for quarks and leptons. The interaction between fermions and the scalar doublet  $\phi$  gives rise to fermion masses and is described by the Yukawa Lagrangian. The scalar part of the Lagrangian is composed of a kinematic and potential component related to the scalar boson.

For the electroweak theory, two coupling constants are introduced, namely  $g'$  for  $U(1)_Y$  and  $g$  for  $SU(2)_L$ . The physically observable gauge bosons of this theory are the photon field  $A_\mu$ , the Z boson field  $Z_\mu^0$ , and the W boson fields  $W_\mu^\pm$ . These are a superposition of the four gauge fields of  $SU(2)_L \times U(1)_Y$ :

$$A_\mu = \sin\theta_W W_\mu^3 + \cos\theta_W B_\mu, \quad Z_\mu^0 = \cos\theta_W W_\mu^3 - \sin\theta_W B_\mu, \quad \text{and} \quad W_\mu^\pm = \sqrt{\frac{1}{2}} (W_\mu^1 \mp i W_\mu^2), \quad (1.5)$$

where  $\theta_W$  represents the weak mixing angle defined as  $\tan \theta_W = \frac{g'}{g}$ .

The coupling constant representing the strength of the QCD interactions is denoted as  $g_s$ . In QCD there is asymptotic freedom whereby the strong coupling constant becomes weaker as the energy with which the interaction between strongly interacting particles is probed increases, and stronger as the distance between the particles increases. A consequence of this is known as colour confinement, the quarks and gluons can not exist on their own and are not observed individually. They are bound in colour neutral states called hadrons, this process is known as hadronisation.

#### 144 Electroweak symmetry breaking

In  $\mathcal{L}_{\text{gauge}}$  and  $\mathcal{L}_f$  are no mass terms for fermions present because only singlets under  $SU(3)_C \times SU(2)_L \times U(1)_Y$  can acquire a mass with an interaction of the type  $m^2 \phi^\dagger \phi$  without breaking the gauge invariance. In order to accommodate mass terms for fermions and gauge fields, electroweak symmetry breaking, leading to  $\mathcal{L}_\phi$  is introduced.

The scalar doublet is introduced in the SM as

$$\phi = \frac{1}{\sqrt{2}} \begin{pmatrix} \varphi_1 + i\varphi_2 \\ \varphi_3 + i\varphi_4 \end{pmatrix}. \quad (1.6)$$

Its field potential is of the form

$$V(\phi) = \mu^2 \phi^\dagger \phi + \lambda (\phi^\dagger \phi)^2, \quad (1.7)$$

with  $\mu^2 < 0$  and  $\lambda$  a positive integer. This choice of parameters gives the potential a "Mexican hat" shape. It has an infinite set of minima (ground states) and by expanding the field around an arbitrary choice of ground state, the electroweak symmetry is broken (EW):

$$\phi = \begin{pmatrix} 0 \\ \frac{v}{\sqrt{2}} \end{pmatrix} + \hat{\phi}, \quad (1.8)$$

where  $v$  is the vacuum expectation value (vev), measured to be around 245 GeV and corresponds to  $\sqrt{\frac{-\mu}{\lambda}}$ . The scalar doublet's four degrees of freedom are reduced to three degrees of freedom

that couple to the gauge fields and fix the  $W^+$ ,  $W^-$  and Zbosons. The remaining fourth degree of freedom has given rise to a physically observable particle, called the Brout-Englert-Higgs (BEH) boson. This spontaneous symmetry breaking leaves the gauge invariance intact and gives masses to the  $W^\pm$  and Zbosons as:

$$m_W = \frac{1}{2}v|g| \quad \text{and} \quad m_Z = \frac{1}{2}v\sqrt{g'^2 + g^2}. \quad (1.9)$$

149 The Brout-Englert-Higgs field couples universally to fermions with a strength proportional to  
150 their masses, and to gauge bosons with a strength proportional to the square of their masses.

### 151 1.3 Flavours in the SM

Flavour changing charged currents are introduced in 1963 by Nicola Cabibbo [12]. Via interactions with a W boson the flavour of the quarks is changed. At the time of the postulation only up, down, and strange quarks were known and the charged weak current was described as a coupling between the up quark and  $d_{\text{weak}}$ , where  $d_{\text{weak}}$  is a linear combination of the down and strange quarks,  $d_{\text{weak}} = \cos\theta_c d + \sin\theta_c s$ . This linear combination is a direct consequence of the chosen rotation

$$\begin{pmatrix} d_{\text{weak}} \\ s_{\text{weak}} \end{pmatrix} = \begin{pmatrix} \cos\theta_c & \sin\theta_c \\ -\sin\theta_c & \cos\theta_c \end{pmatrix} \begin{pmatrix} d \\ s \end{pmatrix} = \mathcal{R} \begin{pmatrix} d \\ s \end{pmatrix}, \quad (1.10)$$

where the rotation angle  $\theta_c$  is known as the Cabibbo angle. This provides a definition for the charged weak current between u and d quarks,

$$J_\mu = \bar{u}\gamma_\mu(1 + \gamma_5)d_{\text{weak}}. \quad (1.11)$$

A consequence of Cabibbo's approach is that the  $s_{\text{weak}}$  is left uncoupled, leading to Glashow, Iliopoulos and Maiani (GIM) [13–15] to require the existence of a fourth quark with charge  $\frac{2}{3}q_e$ . This quark, known as the charm quark, couples to  $s_{\text{weak}}$  and a new definition of the charged weak current is modified to

$$J_\mu = (\bar{u} \quad \bar{c}) \gamma_\mu (1 + \gamma_5) \mathcal{R} \begin{pmatrix} d \\ s \end{pmatrix} = \bar{U} \gamma_\mu (1 + \gamma_5) \mathcal{R} D. \quad (1.12)$$

The neutral weak current is defined as

$$J_3 = \bar{U} \gamma_\mu (1 + \gamma_5) [\mathcal{R}, \mathcal{R}^\dagger] D, \quad (1.13)$$

152 and is diagonal in flavour space. This has as consequence that no flavour changing neutral  
153 currents occur at tree-level interactions [1].

Kobayashi and Maskawa generalised the Cabibbo rotation matrix to accommodate a third generation of quarks. The result is a  $3 \times 3$  unitary matrix known as the CKM matrix, responsible for the mixing of weak interaction states of down-type quarks:

$$\begin{pmatrix} d_{\text{weak}} \\ s_{\text{weak}} \\ b_{\text{weak}} \end{pmatrix} = \begin{pmatrix} V_{ud} & V_{us} & V_{ub} \\ V_{cd} & V_{cs} & V_{cb} \\ V_{td} & V_{ts} & V_{tb} \end{pmatrix} \begin{pmatrix} d \\ s \\ b \end{pmatrix} = \mathcal{V}_{\text{CKM}} \begin{pmatrix} d \\ s \\ b \end{pmatrix}, \quad (1.14)$$

where  $\mathcal{V}_{\text{CKM}}$  is unitary ( $\mathcal{V}_{\text{CKM}}^\dagger \mathcal{V}_{\text{CKM}} = \mathbb{1}$ ). A general  $3 \times 3$  unitary matrix depends on three real angles and six phases. For the CKM matrix, the freedom to redefine the phases of the quark eigenstates can remove five of the phases, leaving a single physical phase known as the Kobayashi-Maskawa phase. This phase is responsible for the charge parity violation in the SM [16]. Each element  $V_{ij}$  of  $\mathcal{V}_{\text{CKM}}$  represents the transition probability of a quark  $i$  going to a quark  $j$ , and is experimentally determined to be [6]

$$\mathcal{V}_{\text{CKM}} = \begin{pmatrix} 0.97425 \pm 0.00022 & 0.2253 \pm 0.0008 & (4.13 \pm 0.49) \times 10^{-3} \\ 0.225 \pm 0.008 & 0.986 \pm 0.016 & (41.1 \pm 1.3) \times 10^{-3} \\ (8.4 \pm 0.6) \times 10^{-3} & (40.0 \pm 2.7) \times 10^{-3} & 1.021 \pm 0.032 \end{pmatrix}. \quad (1.15)$$

From Equation 1.15 follows that top quarks predominantly decay via charged weak currents to bottom quarks, with a probability consistent with unity. In the SM, FCNC can only occur via higher loop interactions which are highly suppressed. The expected transition probabilities for a top quark decaying via a FCNC interaction in the SM are given in Table 1.4, where it is clear that the FCNC top quark interactions of the SM is still beyond the reach of the sensitivity of current experiments.

**Table 1.4:** The predicted branching ratios  $\mathcal{B}$  for FCNC decays involving the top quark in the SM [17].

Process	$\mathcal{B}$ in the SM	Process	$\mathcal{B}$ in the SM
$t \rightarrow uZ$	$8 \times 10^{-17}$	$t \rightarrow cZ$	$1 \times 10^{-14}$
$t \rightarrow u\gamma$	$4 \times 10^{-16}$	$t \rightarrow c\gamma$	$5 \times 10^{-14}$
$t \rightarrow ug$	$4 \times 10^{-14}$	$t \rightarrow cg$	$5 \times 10^{-12}$
$t \rightarrow uH$	$2 \times 10^{-17}$	$t \rightarrow cH$	$3 \times 10^{-15}$

159

## 160 1.4 The top quark in the SM

Discovered in 1995 by the CDF and D0 collaborations at the Tevatron with proton-antiproton data [18, 19], the top quark plays an important role in studying high energy physics. Its Yukawa interaction is given by

$$\mathcal{L}_{\text{top-Yukawa}} = -\frac{\lambda_t v}{\sqrt{2}} \bar{t}_L t_R - \frac{\lambda_t}{\sqrt{2}} H \bar{t}_L t_R + \text{h.c.}, \quad (1.16)$$

yielding a Yukawa coupling of [6]

$$\lambda_t = \frac{\sqrt{2} m_t}{v} = 0.991 \pm 0.003. \quad (1.17)$$

This Yukawa coupling is very large compared to the other Yukawa couplings in the SM ( $\mathcal{O}(10^{-2})$ ), leading to the belief that the top quark may have an important role in understanding the mechanism of electroweak symmetry breaking. On top of this, the very short lifetime of the top quark makes it an excellent candidate to study the properties of a bare quark. Its high mass, almost 40 times higher than the mass of the closest fermion in mass, leads to a large coupling

166 with the Higgs boson and makes the top quark an interesting candidate to investigate how  
 167 particles acquire mass.

168 The CKM matrix element  $V_{tb}$ , given in [Equation 1.15](#), is experimentally found to be much  
 169 larger than  $V_{ts}$ ,  $V_{td}$ , and close to unity. The top quark decays through electroweak interactions  
 170 since the W boson mass is smaller than the top quark mass and the W boson can be on shell. A  
 171 consequence of this is that the top quark has a very short lifetime of only  $1/\Gamma_t \approx 5 \cdot 10^{-25}$  s [6]  
 172 leading to the fact that the formation of bound states involving top quarks are not allowed.  
 173 This lifetime is even shorter than the typical hadronisation timescale of  $1/\Lambda_{QCD} \approx 10^{-23}$  s,  
 174 prohibiting gluons to radiate from the top quark and keeping its spin coherent. Since the  
 175 electroweak interactions have a vector-axial vector (V-A) coupling structure<sup>3</sup>, the top quark  
 176 spin orientation can be derived from the angular distributions of its decay products. This makes  
 177 it possible to study the polarisation of top quarks from the angular distributions in various  
 178 processes.

179 The massiveness of the top quark leads to the fact that a large amount of energy is needed to  
 180 create one. This is only the case for high energy collisions such as those happening in the Earth's  
 181 upper atmosphere when cosmic rays collide with particles in air, or by particle accelerators.  
 182 The production of top quarks happens in two ways: single via the electroweak interaction or in  
 183 pairs via the strong interaction. At hadron colliders, the dominant production mechanism is top  
 184 quark production via gluon ( $gg \rightarrow t\bar{t}$ ) or quark fusion ( $q\bar{q} \rightarrow t\bar{t}$ ). In [Figure 1.1](#), the different top  
 185 quark pair production mechanisms are shown. The production channel of gluon fusion is the  
 186 main contributor to the top quark pair cross section at the LHC compared to quark fusion at the  
 187 Tevatron. The  $gg \rightarrow t\bar{t}$  process contributes 80-90% to the total top quark pair cross section in  
 188 the LHC centre-of-mass energy regime of 7-14 TeV [6]. In [Table 1.5](#) the predicted top quark  
 189 pair production cross sections are given for the LHC and the Tevatron, while in [Figure 1.2](#), a  
 190 summary plot of the LHC and Tevatron top quark pair cross section measurements as a function  
 of the centre-of-mass energy can be found.

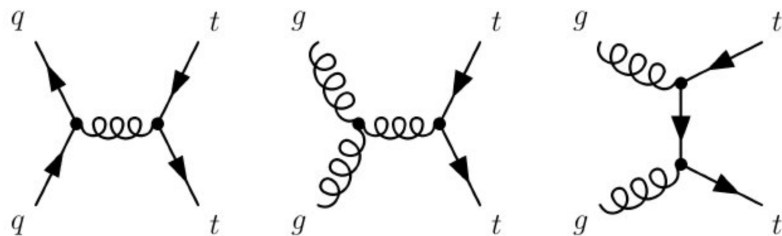


**Figure 1.1:** Leading order diagrams of the top quark pair production. Gluon fusion (right and middle) are the dominant processes at the LHC, while quark fusion (left) is the dominant one at the Tevatron.

191

192 The singly produced top quarks are produced via the electroweak interaction. These production  
 193 mechanisms are subdivided at leading order into three main channels based on the virtuality  
 194 ( $Q^2 = -p_\mu p^\mu$ ) of the exchanged W boson. In [Figure 1.3](#), the corresponding Feynman diagrams  
 195 are shown. The single top quark production cross sections, given in [Table 1.6](#), are smaller than

<sup>3</sup>In the SM a vector - axial vector coupling structure ( $\gamma^\mu - \gamma^\mu \gamma^5$ ) is predicted that only permits left-handed fermions or right-handed anti fermions to interact with a spin-1 particle.

**Table 1.5:** Predictions on the top quark pair production cross sections at next-to-next-to-leading order with next-to-next-to-leading log soft gluon resummation per centre-of-mass energy [6]. The first uncertainty is from scale dependence, while the second uncertainty originates from parton density functions.

Experiment	Top quark mass	Centre-of-mass energy	Cross section (pb)
Tevatron	$m_t = 173.3$ GeV	$\sqrt{s} = 1.96$ TeV	$\sigma_{t\bar{t}} = 7.16^{+0.11+0.17}_{-0.20-0.12}$
LHC	$m_t = 173.2$ GeV	$\sqrt{s} = 7$ TeV	$\sigma_{t\bar{t}} = 173.6^{+4.5+8.9}_{-5.9-8.9}$
LHC	$m_t = 173.2$ GeV	$\sqrt{s} = 8$ TeV	$\sigma_{t\bar{t}} = 247.7^{+6.3+11.5}_{-8.5-11.5}$
LHC	$m_t = 173.2$ GeV	$\sqrt{s} = 13$ TeV	$\sigma_{t\bar{t}} = 816.0^{+19.4+34.4}_{-28.6-34.4}$

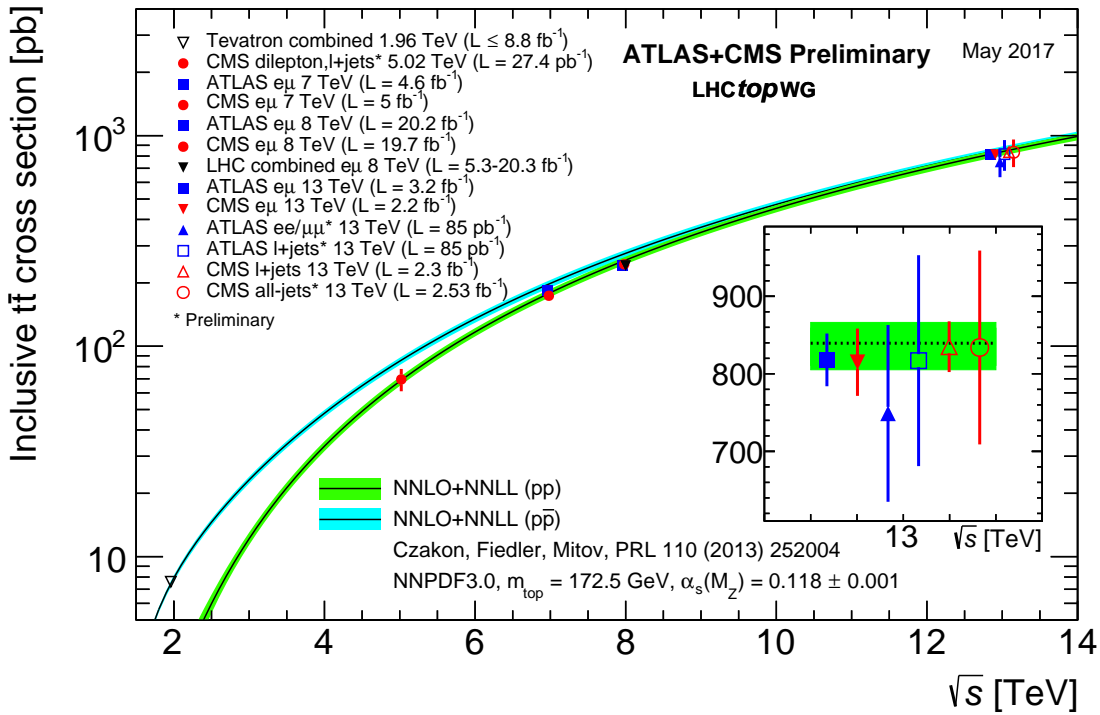


**Figure 1.2:** Summary of the LHC and the Tevatron measurements of the top quark pair production cross section as function of the centre-of-mass energy compared with the next-to-next-to-leading order QCD calculation. The theory bands are the uncertainties due to renormalization and factorisation scales, parton density functions and the strong coupling. The mass of the top quark is assumed to be 172.5 GeV. Measurements for the same centre-of-mass energy are slightly off-set for clarity. Figure taken from [20].

196 the top quark pair production cross sections since the electroweak coupling strength is smaller  
 197 than the strong coupling strength. In addition, for the single top quark production, there is the  
 198 need of sea quarks ( $b, \bar{q}$ ) in the initial states for which the parton density functions increase  
 less steeply at low momentum fractions compared to the gluon parton density functions.

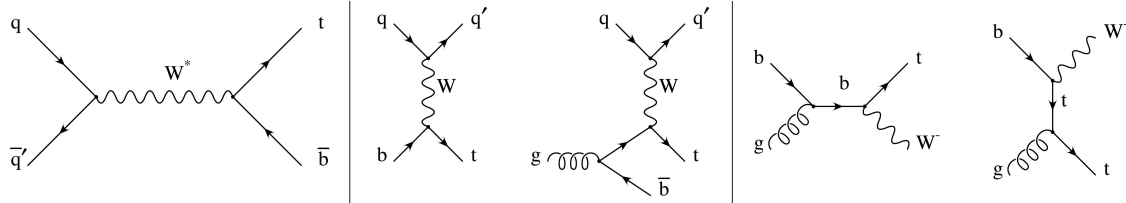


**Figure 1.3:** Leading order Feynman diagrams of the electroweak production of single top quarks in the  $s$ -channel (left),  $t$ -channel (middle), and for the  $tW$  associated production. Figure taken from [21].

199

200 The production via the  $t$ -channel has a virtuality of the  $W$  boson  $Q^2 > 0$ , making it space-like.  
 201 It is produced via the scattering of the  $W$  boson of a bottom quark coming from a proton  
 202 or from gluon splitting ( $g \rightarrow b\bar{b}$ ). It has the highest single top quark cross section in proton  
 203 collisions and the top quark production is roughly twice as large than the antitop quark. This is  
 204 a consequence of the up-down valence quark composition of the proton. This feature makes  
 205 the  $t$ -channel sensitive to the parton density functions of the proton. The  $s$ -channel is the  
 206 production mechanism with the smallest cross section. Here the  $W$  boson is time-like ( $Q^2 < 0$ )  
 207 which requires the  $W$  boson to have a large virtuality to produce the heavier top quark. It is  
 208 produced from two quarks belonging to the same isodoublet (e.g.  $u\bar{d}$ ) and subsequently decays  
 209 to  $t\bar{b}$ . This process get enhanced by many beyond the Standard Model scenarios via the addition  
 210 of new heavy particles such as  $W'$ . The  $tW$ -channel has a top quark produced in association  
 211 with a  $W$  boson produced on shell  $Q^2 = -m_W^2$ . This mode is negligible at the Tevatron, but of  
 212 relevant size at the LHC. The  $tW$ -channel is sensitive to new physics affecting the  $Wtb$  vertex.  
 213 The single top quark production cross section measurements by the CMS collaboration can be  
 214 found in Figure 1.4.

**Table 1.6:** Predictions on the single top quark production cross sections at next-to-leading order per centre-of-mass energy [6]. The uncertainties from scale dependence and from parton density functions are combined in quadrature or given separately (scale + PDF). For the  $t$ -channel the relative proportions to  $t$  and  $\bar{t}$  are 65% and 35%. For the  $s$ -channel this is respectively 69% and 31%. The  $tW$ -channel has an equal proportion of top and antitop quarks. For Tevatron, the top quark mass is assumed to be 173.3 GeV, while the LHC predictions use  $m_t = 172.5$  GeV [6, 22].

Collider	Centre-of-mass energy	Cross section $\sigma_{t+\bar{t}}$ (pb)		
		$t$ -channel	$s$ -channel	$tW$ -channel
Tevatron	$\sqrt{s} = 1.96$ TeV	$2.06^{+0.13}_{-0.13}$	$1.03^{+0.05}_{-0.05}$	-
LHC	$\sqrt{s} = 7$ TeV	$63.89^{+2.91}_{-2.52}$	$4.29^{+0.19}_{-0.17}$	$15.74^{+0.40+1.10}_{-0.40-1.14}$
LHC	$\sqrt{s} = 8$ TeV	$84.69^{+3.76}_{-3.23}$	$5.24^{+0.22}_{-0.20}$	$22.37^{+0.60+1.40}_{-0.60-1.40}$
LHC	$\sqrt{s} = 13$ TeV	$216.99^{+9.04}_{-7.71}$	$10.32^{+0.40}_{-0.36}$	$71.7^{+1.80+3.40}_{-1.80-3.40}$

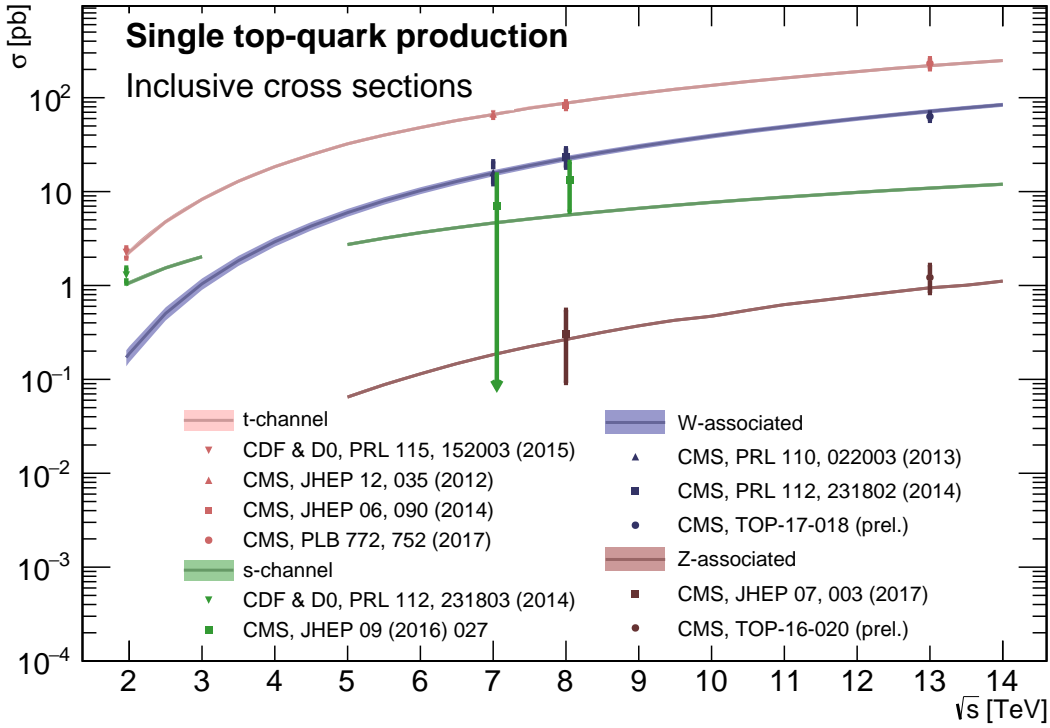


**Figure 1.4:** Summary of the measurements of the single top quark production cross section as function of the centre-of-mass energy. Figure taken from [23].

## 215 1.5 Effective field theories

216 Problems can be simplified if one looks at the relevant scale of the process that one want to  
 217 investigate, for example the chemical properties of an hydrogen atom can be described without  
 218 any knowledge of quark interactions inside the proton. In this case, the proton can be considered  
 219 the elementary object (indivisible) due to the fact that the binding energy of the constituents is  
 220 much bigger than the energy of the electron in orbit around the proton. Effective field theories  
 221 are based on this kind of separation of different energy scales in a system [24]. Effective field  
 222 theories can be used for theories where the perturbative expansion cannot be trusted, e.g. QCD  
 223 at low energy, or as bottom up approach to look for new physics in a model independent way.  
 224 The latter is the way effective field theory will be used throughout this thesis.

The main idea behind effective field theory is easily explained via the example of the Fermi theory. Fermi explained in 1933 [25] the  $\beta$ -decay as a product of currents:

$$\mathcal{L}_{\text{EFT}}^{\text{Fermi}} = -\frac{G_F}{\sqrt{2}} J^\mu J_\mu^\dagger, \quad (1.18)$$

where  $G_F$  is the Fermi coupling constant, measured to be  $G_F \approx 1.17 \times 10^{-5} \text{ GeV}^{-2}$ . The current  $J_\mu$  can written as the sum of an hadronic  $J_\mu^h$  and leptonic  $J_\mu^l$  current, where for simplicity only

the leptonic current will be used further.

$$J_\mu^l = \sum_l \bar{\nu}_l \gamma_\mu (1 - \gamma_5) l. \quad (1.19)$$

225 Historically, charged currents were flavour universal and the later discovered parity violation of  
 226 the weak interaction led to the V-A structure. After this the  $SU(2)_L$  symmetry was postulated  
 227 and the existence of neutral currents was predicted. The effective Lagrangian used then (given  
 228 in [Equation 1.18](#)), could nowadays be build starting from  $SU(2)_L$  symmetries only.

The muon decay can be computed from two different starting points. The effective Fermi Lagrangian provides the decay width of the muon into an electron and two neutrinos

$$\Gamma(\mu \rightarrow e \bar{\nu}_e \nu_\mu) \approx \frac{1}{96\pi^3} \frac{m_\mu^2}{\Lambda_F^4}, \quad (1.20)$$

where  $\Lambda_F$  is the energy scale defined as

$$\frac{G_F}{\sqrt{2}} = \frac{1}{\Lambda_F^2}. \quad (1.21)$$

From muon decay measurements, the value of  $\Lambda_F$  is determined to be  $\Lambda_F \approx 348\text{GeV}$  [[24](#)]. From the SM Lagrangian, one could also calculate the muon decay. Considering that the momenta involved are small compared to the W boson mass, the propagator's denominator can be expanded as [[1](#)]

$$\frac{1}{p^2 - m_W^2} = -\frac{1}{m_W^2} - \frac{p^2}{m_W^4} + \dots \quad (1.22)$$

Looking at the first term, and identifying

$$\frac{g^2}{8m_W} = \frac{1}{\Lambda_F^2}, \quad (1.23)$$

229 one sees that this corresponds with [Equation 1.20](#), thus the effective Lagrangian in [Equation](#)  
 230 [1.18](#) is the first term of the expansion in  $\frac{1}{m_W^2}$  applied on the full Lagrangian.

231 An effective theory is thus a Taylor expansion in the ratio of two scales and the only remnants  
 232 of the full theory at low energies are the symmetries and the values of the coupling constants.  
 233 If the expansion parameter is small, one can truncate the series leading to the Lagrangian  
 234 containing a finite number of free coefficients, making predictions possible. The error on these  
 235 predictions are then of the order as the truncated piece.

The SM can be seen as an effective theory applicable up to energies not exceeding a scale  $\Lambda$ . Therefore, remnants should still be valid and the theory above that scale should have a gauge group containing  $SU(3)_C \times SU(2)_L \times U(1)_Y$  and all the SM degrees of freedom, as well as reduce to the SM at lower energies. The general SM Lagrangian becomes then

$$\mathcal{L}_{\text{SM+EFT}} = \mathcal{L}_{\text{SM}}^{(4)} + \frac{1}{\Lambda} \sum_k C_k^{(5)} Q_k^{(5)} + \frac{1}{\Lambda^2} \sum_k C_k^{(6)} Q_k^{(6)} + \mathcal{O}\left(\frac{1}{\Lambda^3}\right), \quad (1.24)$$

236 where  $Q_k^{(n)}$  are dimension- $n$  operators (currents) and  $C_k^{(n)}$  the corresponding dimensionless  
237 coupling constants, so-called Wilson coefficients. The Wilson coefficients are determined by the  
238 underlying high energy theory.

239 In the Warsaw basis [26], a set of independent operators of dimension 5 and 6 are built out  
240 of the SM fields and are consistent with the SM gauge symmetries and is fully derived in Ref.  
241 [26]. In general the various measurements show a good agreement with the SM predictions  
242 and by lack of deviations from the SM, limits on the anomalous couplings can be derived. The  
243 estimated coupling strengths per operator contributing to single top quark production obtained  
244 from various measurements at the LHC and Tevatron are shown in Figure 1.5 for which the  
245 conventions are discussed in Ref. [27]. These results are consistent with the SM expectation for  
246 which those operators vanish.

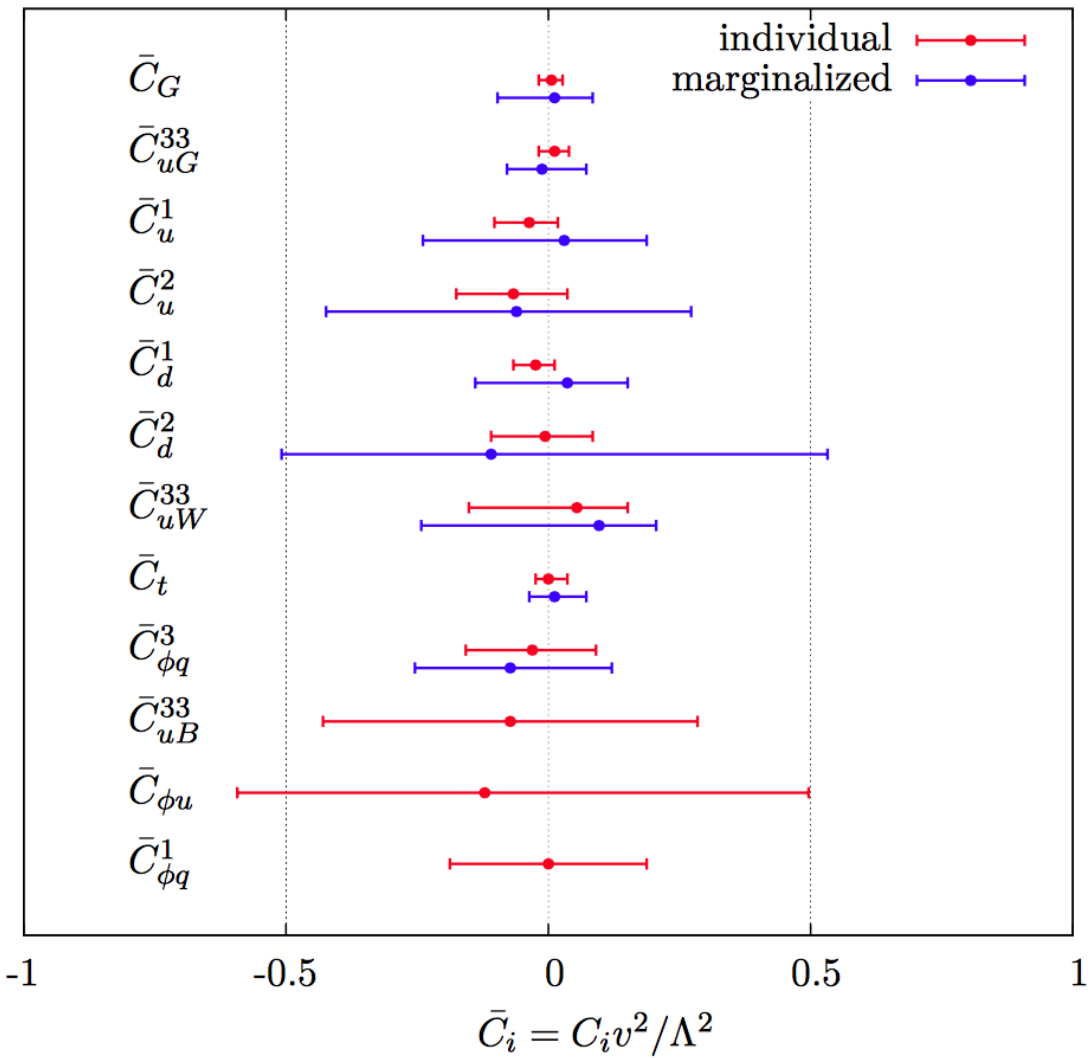


**Figure 1.5:** Global fit results of top quark effective field theory to experimental data including all constrained operators at dimension six. For the operators, the Warsaw basis of [26] is used. The bounds are set on the Wilson coefficients of various operators contributing to top quark production and decay in two cases (red) all other coefficients set to zero, or (blue) all other coefficients marginalized over. Figure taken from [28].

## <sup>247</sup> 1.6 Motivation for new physics

<sup>248</sup> Many high energy experiments confirm the success of the SM. In particular the scalar boson,  
<sup>249</sup> the cornerstone of the SM, has consecrated the theory. Unfortunately there are also strong  
<sup>250</sup> indications that the SM ought to be a lower energy expression of a more global theory. The  
<sup>251</sup> existence of physics beyond the SM (BSM) [29] is strongly motivated. These motivations are  
<sup>252</sup> based on direct evidence from observation such as the existence of neutrino masses, the existence  
<sup>253</sup> of dark matter and dark energy, or the matter-antimatter asymmetry, and also from theoretical  
<sup>254</sup> problems such as the hierarchy problem, the coupling unification or the large numbers of free  
<sup>255</sup> parameters in the SM.

<sup>256</sup> In the SM, the neutrinos are assumed to be massless, while experiments with solar, atmospheric,  
<sup>257</sup> reactor and accelerator neutrinos have established that neutrinos can oscillate and change flavour  
<sup>258</sup> during flight [4, 5]. These oscillations are only possible when neutrinos have masses. The  
<sup>259</sup> flavour neutrinos ( $\nu_e$ ,  $\nu_\mu$ ,  $\nu_\tau$ ) are then linear expressions of the fields of at least three mass  
<sup>260</sup> eigenstate neutrinos  $\nu_1$ ,  $\nu_2$ , and  $\nu_3$ .

<sup>261</sup> The ordinary or baryonic matter described by the SM describes only 5% of the mass (energy)  
<sup>262</sup> content of the universe. Astrophysical evidence indicated that dark matter is contributing  
<sup>263</sup> to approximately 27%, and dark energy to 68% of the content of the universe. From the  
<sup>264</sup> measurements of the temperature and polarizations anisotropies of the cosmic microwave  
<sup>265</sup> background by the Planck experiment [30], the density of cold non baryonic matter is determined.  
<sup>266</sup> Cold dark matter is assumed to be only sensitive to the weak and gravitational force, leading  
<sup>267</sup> to only one possible SM candidate: the neutrino. However, these are too light to account for  
<sup>268</sup> the vast amount of dark matter and other models are needed. Dark energy is assumed to be  
<sup>269</sup> responsible for the acceleration in the expansion of the universe [31].

<sup>270</sup> At the Big Bang matter and antimatter are assumed to be produced in equal quantities.  
<sup>271</sup> However, it is clear that we are surrounded by matter. So where did all the antimatter go?  
<sup>272</sup> In 1967, Sakharov identified three mechanisms that are necessary to obtain a global matter  
<sup>273</sup> antimatter asymmetry [32]. These mechanisms are those of baryon and lepton number violation,  
<sup>274</sup> that at a given moment in time there was a thermal imbalance for the interactions in the universe,  
<sup>275</sup> and there is charge C and charge parity CP violation<sup>4</sup>.

<sup>276</sup> The large number of free parameters in the SM comes from the nine fermion masses, three  
<sup>277</sup> CKM mixing angles and one CP violating phase, one EM coupling constant  $g'$ , one weak coupling  
<sup>278</sup> constant  $g$ , one strong coupling constant  $g_s$ , one QCD vacuum angle, one vacuum expectation  
<sup>279</sup> value, and one mass of the scalar boson. This large number of free parameters leads to the  
<sup>280</sup> expectation of a more elegant and profound theory beyond the SM.

<sup>281</sup> The hierarchy problem [33] is related to the huge difference in energy between the weak  
<sup>282</sup> scale and the Planck scale. The vev of the Brout-Englert-Higgs field determines the weak scale  
<sup>283</sup> that is approximately 246 GeV. The radiative corrections to the scalar boson squared mass  $m_H^2$ ,  
<sup>284</sup> coming from its self couplings and couplings to fermions and gauge bosons, are quadratically

---

<sup>4</sup>The rate of a process  $i \rightarrow f$  can be different from the CP-conjugate process:  $\tilde{i} \rightarrow \tilde{f}$ . The SM includes sources of CP-violation through the residual phase of the CKM matrix. However, these could not account for the magnitude of the asymmetry observed.

285 proportional to the ultraviolet momentum cut-off  $\Lambda_{\text{UV}}$ . This cut-off is at least equal to the energy  
 286 to which the SM is valid without the need of new physics. For the SM to be valid up to the  
 287 Planck mass, the correction to  $m_H^2$  becomes thirty orders of magnitude larger than  $m_H^2$ . This  
 288 implies that an extraordinary cancellation of terms should happen. This is also known as the  
 289 naturalness problem of the H boson mass.

The correction to the squared mass of the scalar boson coming from a fermion  $f$ , coupling to the scalar field  $\phi$  with a coupling  $\lambda_f$  is given by

$$\Delta m_H^2 = -\frac{|\lambda_f|^2}{8\pi^2} \Lambda_{\text{UV}}^2, \quad (1.25)$$

while the correction to the mass from a scalar particle  $S$  with a mass  $m_S$ , coupling to the scalar field with a Lagrangian term  $-\lambda_S |\phi|^2 |S|^2$  is

$$\Delta m_H^2 = \frac{|\lambda_S|^2}{16\pi^2} \left( \Lambda_{\text{UV}}^2 - 2m_S^2 \ln \left( \frac{\Lambda_{\text{UV}}}{m_S} \right) + \dots \right). \quad (1.26)$$

290 As one can see the correction term to  $m_H^2$  is much larger than  $m_H^2$  itself. By introducing BSM  
 291 physics models that introduce new scalar particles at the TeV scale that couple to the scalar  
 292 boson one can cancel the  $\Lambda_{\text{UV}}^2$  divergence and avoid this fine-tuning.

293 The choice of the  $SU(3)_C \times SU(2)_L \times U(1)_Y$  symmetry group itself as well as the separate  
 294 treatment of the three forces included in the SM raises concern. The intensity of the forces  
 295 show a large disparity around the electroweak scale, but have comparable strengths at higher  
 296 energies. The electromagnetic and weak forces are unified in a electroweak interaction, but the  
 297 strong coupling constant does not encounter the other coupling constants at high energies. In  
 298 order to reach a grand unification, the running of couplings can be modified by the addition of  
 299 new particles in BSM models.

## 300 1.7 An effective approach beyond the SM: FCNC involving a top 301 quark

302 The closeness of the top quark mass to the electroweak scale led physicist to believe that it  
 303 is a sensitive probe for new physics. Studying its properties is therefore an important topic  
 304 of the experimental program at the LHC. Several extensions of the SM enhance the FCNC  
 305 branching ratios and can be probed at the LHC [17], from which some of them are shown in  
 306 Table 1.7. Previous searches have been performed at the Tevatron by the CDF [34] and D0 [35]  
 307 collaborations, and at the LHC by the ATLAS [36–40] and CMS [41–45] collaborations.

308 The impact of BSM models can be written in a model independent way by means of an  
 309 effective field theory valid up to an energy scale  $\Lambda$ . The leading effects are parametrized by a  
 310 set of fully gauge symmetric operators that are added to the SM Lagrangian and can be reduced  
 311 to a minimal set of operators as seen in Equation 1.24. For simplicity, the assumption is made  
 312 that new physics effects are exclusively described by dimension-6 operators, thus neglecting

**Table 1.7:** The predicted branching ratios  $\mathcal{B}$  for FCNC interactions involving the top quark in some BSM models [17]: quark singlet (QS), generic two Higgs doublet model (2HDM) and the minimal supersymmetric extensions to the SM (MSSM);

Process	QS	2HDM	MSSM	Process	QS	2HDM	MSSM
$t \rightarrow uZ$	$\leq 1.1 \times 10^{-4}$	—	$\leq 2 \times 10^{-6}$	$t \rightarrow cZ$	$\leq 1.1 \times 10^{-4}$	$\leq 10^{-7}$	$\leq 2 \times 10^{-6}$
$t \rightarrow u\gamma$	$\leq 7.5 \times 10^{-9}$	—	$\leq 2 \times 10^{-6}$	$t \rightarrow c\gamma$	$\leq 7.5 \times 10^{-9}$	$\leq 10^{-6}$	$\leq 2 \times 10^{-6}$
$t \rightarrow ug$	$\leq 1.5 \times 10^{-7}$	—	$\leq 8 \times 10^{-5}$	$t \rightarrow cg$	$\leq 1.5 \times 10^{-7}$	$\leq 10^{-4}$	$\leq 8 \times 10^{-5}$
$t \rightarrow uH$	$\leq 4.1 \times 10^{-5}$	$\leq 5.5 \times 10^{-6}$	$\leq 10^{-5}$	$t \rightarrow cH$	$\leq 4.1 \times 10^{-5}$	$\leq 10^{-3}$	$\leq 10^{-5}$

313 neutrino physics. In the fully gauge symmetric case, the EFT Lagrangian is then given by

$$\mathcal{L}_{\text{SM+EFT}} = \mathcal{L}_{\text{SM}} + \sum_i \frac{\bar{c}_i}{\Lambda^2} O_i + \mathcal{O}\left(\frac{1}{\Lambda^3}\right), \quad (1.27)$$

where the Wilson coefficients  $\bar{c}_i$  depend on the considered theory and on the way that new physics couples to the SM particles. Considering that  $\Lambda$  is large, contributions suppressed by powers of  $\Lambda$  greater than two are neglected. Moreover, all four fermion operators are omitted for the rest of this thesis. The Warsaw basis is adopted for the independent effective operators [26], parametrising the new physics effects relevant for the flavour changing neutral current interactions of the top quark as, all flavour indices understood,

$$\begin{aligned} \mathcal{L}_{\text{EFT}}^t = & \frac{\bar{c}_{uG}}{\Lambda^2} \Phi^\dagger \cdot [\bar{Q}_L \sigma^{\mu\nu} \mathcal{T}_a u_R] G_{\mu\nu}^a + \frac{\bar{c}_{uB}}{\Lambda^2} \Phi^\dagger \cdot [\bar{Q}_L \sigma^{\mu\nu} u_R] B_{\mu\nu} + \frac{2\bar{c}_{uW}}{\Lambda^2} \Phi^\dagger T_i \cdot [\bar{Q}_L \sigma^{\mu\nu} u_R] W_{\mu\nu}^i \\ & + i \frac{\bar{c}_{hu}}{\Lambda^2} \left[ \Phi^\dagger \overleftrightarrow{D}_\mu \Phi \right] [\bar{u}_R \gamma^\mu u_R] + i \frac{\bar{c}_{hq}^{(1)}}{\Lambda^2} \left[ \Phi^\dagger \overleftrightarrow{D}_\mu \Phi \right] [\bar{Q}_L \gamma^\mu Q_L] \\ & + i \frac{4\bar{c}_{HQ}^{(3)}}{\Lambda^2} \left[ \Phi^\dagger T_i \overleftrightarrow{D}_\mu \Phi \right] [\bar{Q}_L \gamma^\mu T^i Q_L] + \frac{\bar{c}_{uh}}{\Lambda^2} \Phi^\dagger \Phi \Phi^\dagger \cdot [\bar{Q}_L u_R] + \text{h.c.}, \end{aligned} \quad (1.28)$$

where the left handed  $SU(2)_L$  doublet of the quark fields is denoted by  $Q_L$ , the up-type right handed fields by  $u_R$ , the down-type right handed fields by  $d_R$ , the  $SU(2)_L$  doublet of the Higgs field by  $\Phi$ , the field strength tensors as

$$\begin{aligned} B_{\mu\nu} &= \partial_\mu B_\nu - \partial_\nu B_\mu, \\ W_{\mu\nu}^k &= \partial_\mu W_\nu^k - \partial_\nu W_\mu^k - g \epsilon_{ij}^k W_\mu^i W_\nu^j, \\ G_{\mu\nu} &= \partial_\mu G_\nu^a - \partial_\nu G_\mu^a + g_s f_{bc}^a G_\mu^b G_\nu^c, \end{aligned} \quad (1.29)$$

denoting the structure constant of the  $SU(3)_C$  group as  $f_{bc}^a$  and the structure constant of the  $SU(2)_L$  group as  $\epsilon_{ij}^k$ . The gauge covariant derivatives are also standard defined as

$$D_\mu \Phi = \partial_\mu \Phi - \frac{1}{2} i g' B_\mu \Phi - i g T_k W_\mu^k \Phi \quad (1.30)$$

with the conventions of Section 1.2. The representation matrices  $T$  of  $SU(2)_L$  are defined in Equation 1.1, while the representation matrices  $\mathcal{T}$  of  $SU(3)_C$  are the Gell-Mann matrices [1].

The hermitian derivative operator is defined as

$$\Phi^\dagger \overleftrightarrow{D} \Phi = \Phi^\dagger D^\mu \Phi - D_\mu \Phi^\dagger \Phi. \quad (1.31)$$

After electroweak symmetry breaking the operators induce [17, 46] both corrections to the SM couplings and new interactions at tree level such as FCNC interactions. The FCNC interactions of the top quark that are not present in the SM are given by

$$\mathcal{L}_{\text{EFT}}^t = \frac{\sqrt{2}}{2} \sum_{q=u,c} \left[ g' \frac{\kappa_{t\gamma q}}{\Lambda} A_{\mu\nu} \bar{t} \sigma^{\mu\nu} (f_{\gamma q}^L P_L + f_{\gamma q}^R P_R) q \right. \quad (1.32)$$

$$+ \frac{g}{2\cos\theta_W} \frac{\kappa_{tZq}}{\Lambda} Z_{\mu\nu} \bar{t} \sigma^{\mu\nu} (f_{Zq}^L P_L + f_{Zq}^R P_R) q \quad (1.33)$$

$$+ \frac{\sqrt{2}g}{4\cos\theta_W} \zeta_{tZq} \bar{t} \gamma^\mu (\tilde{f}_q^L P_L + \tilde{f}_q^R P_R) q Z_\mu \quad (1.34)$$

$$+ g_s \frac{\kappa_{tgq}}{\Lambda} Z_{\mu\nu} \bar{t} \sigma^{\mu\nu} (f_{gq}^L P_L + f_{gq}^R P_R) q G_\mu^a \quad (1.35)$$

$$+ \eta_{Hqt} \bar{t} (\hat{f}_q^L P_L + \hat{f}_q^R P_R) q H + \text{h.c.} \Big], \quad (1.36)$$

where the value of the FCNC couplings at scale  $\Lambda$  are represented by  $\kappa_{tZq}, \kappa_{tgq}, \kappa_{t\gamma q}, \zeta_{tZq}$ , and  $\eta_{Hqt}$ . These are assumed to be real and positive, with the unit of  $\text{GeV}^{-1}$  for  $\kappa_{txq}/\Lambda$  and no unit for  $\zeta_{xqt}$  and  $\eta_{xqt}$ . In the equation  $\sigma^{\mu\nu}$  equals to  $\frac{i}{2} [\gamma^\mu, \gamma^\nu]$ , and the left- and right-handed chirality projector operators are denoted by  $P_L$  and  $P_R$ . The electromagnetic coupling constant is denoted by  $g'$ , the strong interaction coupling is denoted as  $g_s$ , while the electroweak interaction is parametrised by the coupling constant  $g$  and the electroweak mixing angle  $\theta_W$ . The complex chiral parameters are normalized according to  $|f_{xq}^L|^2 + |f_{xq}^R|^2 = 1$ ,  $|\tilde{f}_q^L|^2 + |\tilde{f}_q^R|^2 = 1$ , and  $|\hat{f}_q^L|^2 + |\hat{f}_q^R|^2 = 1$ . In the expression for  $\mathcal{L}_{\text{EFT}}^t$ , the unitary gauge is adopted and the scalar field is expanded around its vacuum expectation value  $v$  with  $H$  being the SM scalar boson, and the field strength tensors of the photon  $A_\mu$ , the gluon field  $G_\mu^{1\dots 8}$ , and the Z boson  $Z_\mu^0$  are defined as

$$\begin{aligned} A_{\mu\nu} &= \partial_\mu A_\nu - \partial_\nu A_\mu, \\ Z_{\mu\nu} &= \partial_\mu Z_\nu - \partial_\nu Z_\mu, \text{ and} \\ G_{\mu\nu} &= \partial_\mu G_\nu^a - \partial_\nu G_\mu^a + g_s f_{bc}^a G_\mu^b G_\nu^c. \end{aligned} \quad (1.37)$$

<sup>314</sup> Note that there are two coupling constants arising in  $\mathcal{L}_{\text{EFT}}^t$ , which is a residue of electroweak  
<sup>315</sup> symmetry breaking. The massive Z boson will appear in both the  $Z_\mu^0$  field as well as the covariant  
<sup>316</sup> derivative, leading to an extra Z-vertex.

317 The relations between the Wilson coefficients in (1.28) and the coupling strengths of the  
 318 interactions in Equation 1.36 can be derived. The 14 effective operators are mapped onto 10  
 319 free parameters providing a more minimal parametrisation of the anomalous interactions of the  
 320 top quark.

$$\begin{aligned}
 \kappa_{tqg} f_{gq}^L &= \frac{\nu}{g_s \Lambda} [\bar{c}_{uG}]_{i3}^*, & \kappa_{tqg} f_{gq}^R &= \frac{\nu}{g_s \Lambda} [\bar{c}_{uG}]_{3i}, \\
 \kappa_{t\gamma q} f_{\gamma q}^L &= \frac{\nu}{g' \Lambda} [\cos\theta_W \bar{c}_{uB} - \sin\theta_W \bar{c}_{uW}]_{i3}^*, & \kappa_{t\gamma q} f_{\gamma q}^R &= \frac{\nu}{g' \Lambda} [\sin\theta_W \bar{c}_{uB} - \cos\theta_W \bar{c}_{uW}]_{3i}, \\
 \kappa_{tZq} f_{Zq}^L &= -\frac{2\cos\theta_W \nu}{g \Lambda} [\sin\theta_W \bar{c}_{uB} + \cos\theta_W \bar{c}_{uW}]_{i3}^*, & \kappa_{tZq} f_{Zq}^R &= -\frac{2\cos\theta_W \nu}{g \Lambda} [\cos\theta_W \bar{c}_{uB} + \sin\theta_W \bar{c}_{uW}]_{3i}, \\
 \zeta_{tZq} \tilde{f}_{Zq}^L &= -\frac{2\nu^2}{\Lambda^2} [(\bar{c}_{hq}^{(1)} - \bar{c}_{hq}^{(3)})_{i3} + (\bar{c}_{hq}^{(1)} - \bar{c}_{hq}^{(3)})_{3i}^*], & \zeta_{tZq} \tilde{f}_{Zq}^R &= -\frac{2\nu^2}{\Lambda^2} [(\bar{c}_{hu})_{i3} + (\bar{c}_{hu})_{3i}^*], \\
 \eta_{tHq} \hat{f}_{Hq}^L &= \frac{3\nu^2}{2\Lambda^2} [\bar{c}_{uh}]_{3i}^*, & \eta_{tHq} \hat{f}_{Hq}^R &= \frac{3\nu^2}{2\Lambda^2} [\bar{c}_{uh}]_{i3}.
 \end{aligned} \tag{1.38}$$

## 321 1.8 Experimental constraints on top-FCNC

Experiments commonly put limits on the branching ratios which allow an easier interpretation across different EFT models by use of the branching ratio

$$\mathcal{B}(t \rightarrow qX) = \frac{\delta_{txq}^2 \Gamma_{t \rightarrow qX}}{\Gamma_t}, \tag{1.39}$$

322 where  $\Gamma_{t \rightarrow qX}$  represents the FCNC decay width<sup>5</sup> for a coupling strength  $\delta_{txq}^2 = 1$ , and  $\Gamma_t$  the full  
 323 decay width of the top quark. In the SM, supposing a top quark mass of 172.5 GeV, the full  
 324 width becomes  $\Gamma_t^{\text{SM}} = 1.32$  GeV [47].

325 Searches for top-FCNC usually adopt a search strategy depending on the experimental set-up  
 326 and the FCNC interaction of interest, looking either for FCNC interactions in the production of a  
 327 single top quark or in its decay for top quark pair interactions. In Figure 1.6, these two cases  
 328 are shown for the tZq vertex.

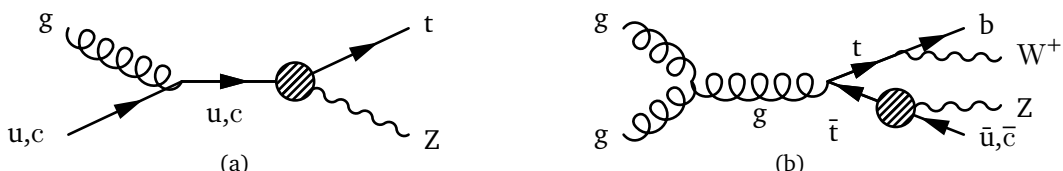


**Figure 1.6:** Feynman diagrams for the processes with a tZq FCNC interaction, where the FCNC interaction is indicated with the shaded dot. (a) Single top quark production through an FCNC interaction. (b) Top quark pair production with an FCNC induced decay.

<sup>5</sup>The decay width of a certain process represents the probability per unit time that a particle will decay. The total decay width, defined as the sum of all possible decay widths of a particle, is inversely proportional to its lifetime.

330 The observation of top-FCNC interactions has yet to come and experiments have so far only  
 331 been able to put upper bounds on the branching ratios. An overview of the best current limits is  
 332 given in [Table 1.8](#). In [Figure 1.7](#) a comparison is shown between the current best limits set by  
 333 ATLAS and CMS with respect to several BSM model benchmark predictions. From there one can  
 334 see that FCNC searches involving a Z or H boson are close to excluding or confirming several  
 335 BSM theories. In [Figure 1.9](#), the searches performed by CMS are summarised. For the tZq  
 336 vertex, the best limit from CMS comes from Ref. [41] where both single top quark and top quark  
 337 pair is studied. The observed (expected) limits 95% CL at 8 TeV for the FCNC tZq interaction  
 338 by CMS are  $\mathcal{B}(t \rightarrow uZ) < 2.2 \times 10^{-4}$ ( $2.7 \times 10^{-4}$ ) and  $\mathcal{B}(t \rightarrow cZ) < 4.9 \times 10^{-4}$ ( $12 \times 10^{-4}$ ). In  
 339 [Figure 1.8](#), the summary of the 95% confidence level observed limits on the branching ratios  
 340 of the top quark decays to a charm or up quark and a neutral boson is given, considering the results from the HERA, the LEP, the Tevatron, and the the LHC.

**Table 1.8:** Overview of the most stringent observed and expected experimental limits on top-FCNC branching ratios  $\mathcal{B}$  at 95% confidence level.

Process	Search mode	Observed $\mathcal{B}$	Expected $\mathcal{B}$	Experiment	
$t \rightarrow uZ$	top quark pair decay	$1.7 \times 10^{-4}$	$2.4 \times 10^{-4}$	ATLAS	[40]
$t \rightarrow u\gamma$	single top quark production	$1.3 \times 10^{-4}$	$1.9 \times 10^{-4}$	CMS	[43]
$t \rightarrow ug$	single top quark production	$4.0 \times 10^{-5}$	$3.5 \times 10^{-5}$	ATLAS	[37]
$t \rightarrow uH$	top quark pair decay	$2.4 \times 10^{-3}$	$1.7 \times 10^{-3}$	ATLAS	[39]
$t \rightarrow cZ$	top quark pair decay	$2.3 \times 10^{-4}$	$3.2 \times 10^{-4}$	ATLAS	[40]
$t \rightarrow c\gamma$	single top quark production	$2.0 \times 10^{-3}$	$1.7 \times 10^{-3}$	CMS	[43]
$t \rightarrow cg$	single top quark production	$2.0 \times 10^{-4}$	$1.8 \times 10^{-4}$	ATLAS	[37]
$t \rightarrow cH$	top quark pair decay	$2.2 \times 10^{-3}$	$1.6 \times 10^{-3}$	CMS	[39]

341

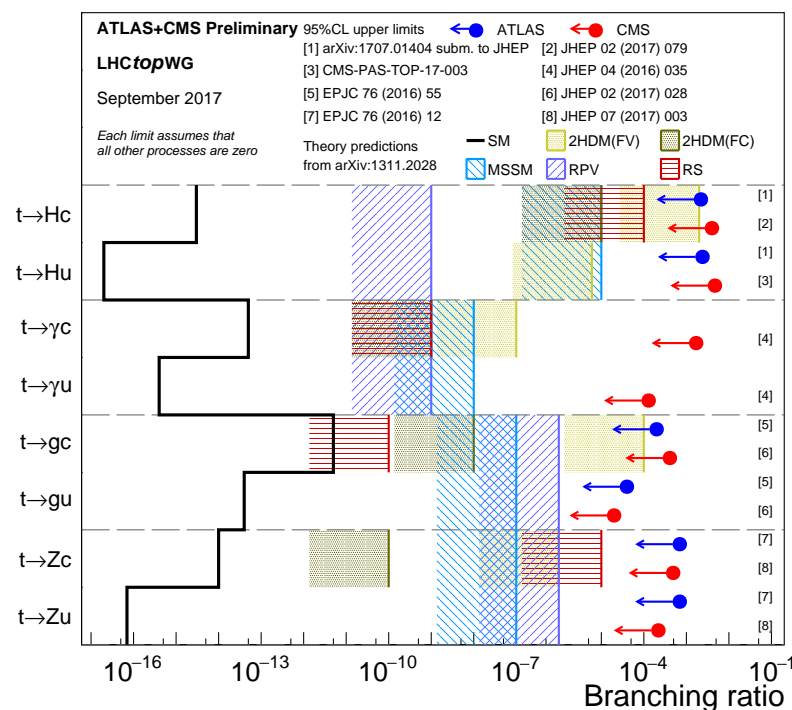


**Figure 1.7:** Current best limits set by CMS and ATLAS for top-FCNC interactions. Figure taken from [23]. (TO DO Remake with new atlas results)

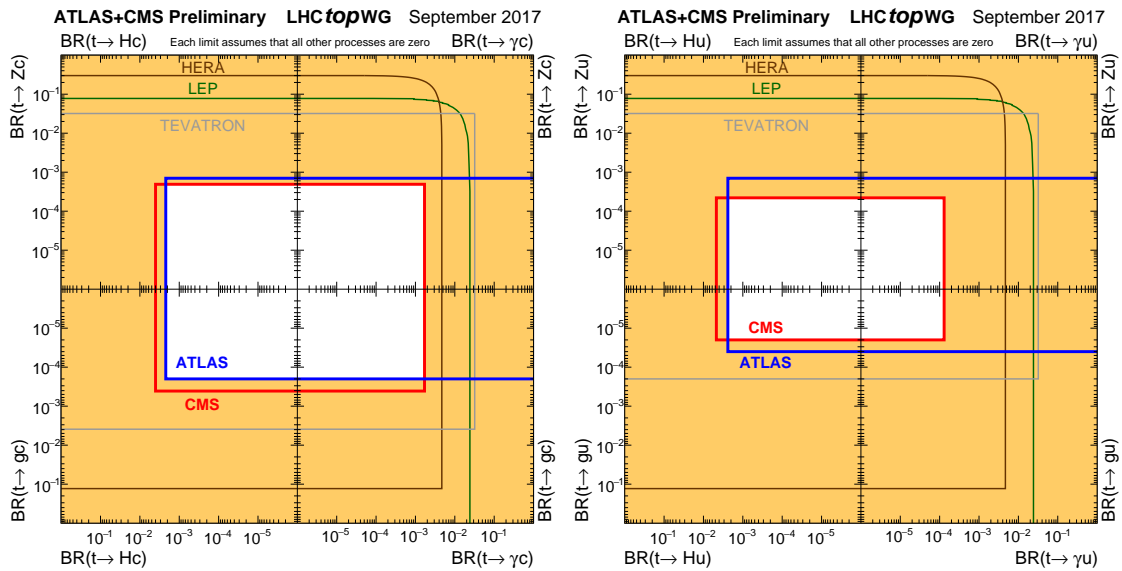


**Figure 1.8:** Summary of the current 95% confidence level observed limits on the branching ratios of the top quark decays via flavour changing neutral currents to a charm (left) or up (right) quark and a neutral boson. The coloured lines represent the results from HERA (the most stringent limits between the ones obtained by the H1 and ZEUS collaborations, in brown), LEP (combined ALEPH, DELPHI, L3 and OPAL collaborations result, in green), TEVATRON (the most stringent limits between the ones obtained by the CDF and D0 collaborations, in grey). The yellow area represents the region excluded by the ATLAS and the CMS Collaborations. Figure taken from [20].

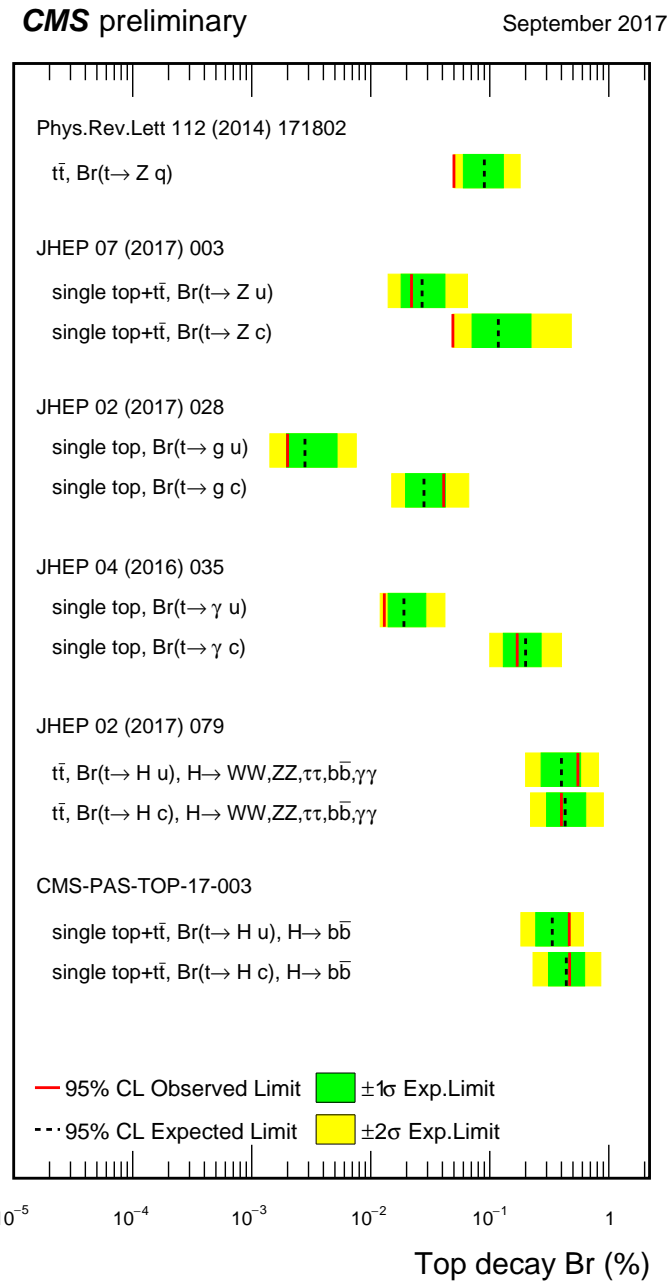


**Figure 1.9:** Summary of the FCNC branching ratios from CMS searches at 8 TeV. Figure taken from [23].

# Experimental set-up

# 2

---

343 A key objective of the Large Hadron Collider (LHC) was the search for the Brout-Englert-Higgs  
 344 boson. The Large Electron Positron (LEP) [48] and Tevatron [49] experiments established  
 345 that the mass of the scalar boson has to be larger than 114 GeV [50, 51], and smaller than  
 346 approximate 1 TeV due to unitarity and perturbativity constraints [52]. On top of this, the  
 347 search for new physics such as supersymmetry or the understanding of dark matter were part  
 348 of the motivation for building the LHC. Since the start of its operation, the LHC is pushing the  
 349 boundaries of the Standard Model, putting the most stringent limits on physics beyond the  
 350 Standard Model as well as precision measurements of the parameters of the Standard Model. A  
 351 milestone of the LHC is the discovery the scalar boson in 2012 by the two largest experiments  
 352 at the LHC [10, 11].

353 This chapter is dedicated to the experimental set up of the LHC and the Compact Muon  
 354 Solenoid (CMS) experiment. Section 2.1 describes the LHC and its acceleration process for  
 355 protons to reach their design energies. The CMS experiment and its components are presented  
 356 in Section 2.2. The upgrades performed during the long shutdown in 2013 are discussed  
 357 in Section 2.2.4. The data acquisition of CMS is presented in Section 2.2.3, while the CMS  
 358 computing model is shown in Section 2.2.5.

## 359 2.1 The Large Hadron Collider

360 The LHC has started its era of cutting edge science on 10 September 2008 [53] after approval by  
 361 the European Organisation of Nuclear Research (CERN) in 1995 [54]. Installed in the previous  
 362 LEP tunnel, the LHC consists of a 26.7 km quasi ring, that is installed between 45 and 170 m  
 363 under the French-Swiss border amidst Cessy (France) and Meyrin (Switzerland). Built to study  
 364 rare physics phenomena at high energies, the LHC can accelerate mainly two types of particles,  
 365 protons and lead ions  $Pb^{45+}$ , and provides collisions at four interaction points, where the particle  
 366 bunches are crossing. Experiments for studying the collisions are installed at each interaction  
 367 point.

368 As can be seen in Figure 2.1, the LHC is the last element in a chain that creates, injects and  
 369 accelerates protons. The starting point is the ionisation of hydrogen, creating protons that are  
 370 injected in a linear accelerator (LINAC 2). Here, the protons obtain an energy of 50 MeV. They

371 continue to the Proton Synchrotron Booster (PSB or Booster), where the packs of protons are  
 372 accelerated to 1.4 GeV and each pack is split up in twelve bunches with 25 or 50 ns spacing.  
 373 The Proton Synchrotron (PS) then increases their energy to 25 GeV before the Super Proton  
 374 Synchrotron (SPS) increases the proton energy up to 450 GeV. Each accelerator ring expands in  
 375 radius in order to reduce the energy loss of the protons by synchrotron radiation<sup>1</sup>. Furthermore,  
 376 the magnets responsible for the bending of the proton trajectories have to be strong enough  
 377 to sustain the higher proton energy. Ultimately, the proton bunches are injected into opposite  
 378 directions into the LHC, where they are accelerated to 3.5 TeV (in 2010 and 2011), 4 TeV (in  
 2012 and 2013) or 6.5 TeV (in 2015 and 2016) [55].

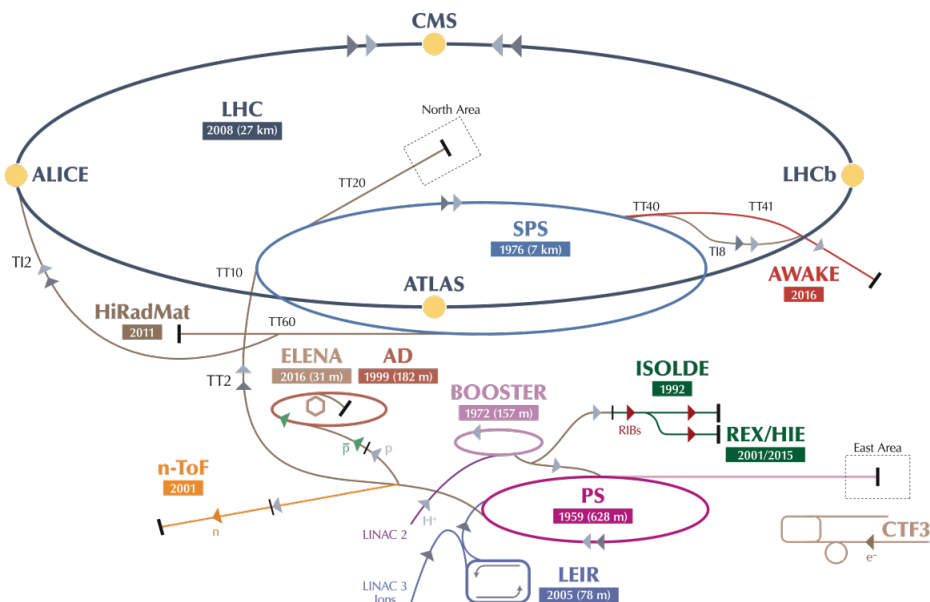


**Figure 2.1:** Schematic representation of the accelerator complex at CERN [56]. The LHC (dark blue) is the last element in chain of accelerators. Protons are successively accelerated by LINAC 2, the Booster, the Proton Synchrotron (PS) and the Super Proton Synchrotron (SPS) before entering the LHC.

379

380 In Figure 2.2 the LHC programme is shown. the first data collisions, so-called Run 1 period,  
 381 lasted from 2008 until 16 February 2013 after which the CERN accelerator complex shut down  
 382 for two years of planned maintenance and consolidation during so-called long shutdown 1  
 383 (LS1). On 23 March 2015, the new data taking period known as Run 2 started. With a brief  
 384 end of the year extended technical stop (EYETS). The main activities carried out during the  
 385 EYETS were the maintenance of many system such as the cryogenics, the cooling, electrical  
 386 systems, etc.; the replacement of magnet, as well as a de-cabling and cabling campaign on  
 387 the SPS. Run 2 will last until July 2018 when the long shut down 2 (LS2) will begin for 2  
 388 years. The main goal of this shutdown is the LHC injectors upgrade (LUI), but also maintenance  
 389 and consolidation will be performed. Furthermore, preparations for the High Luminosity LHC,

<sup>1</sup>This energy loss is proportional to the fourth power of the proton energy and inversely proportional to the bending radius.

390 which will start in 2024, will be done. More information about phase 1 upgrades during LS1  
 391 and EYETS is given in [Section 2.2.4](#).

392 Before the start of the LHC in 2010, the previous energy record was held by the Tevatron collider  
 393 at Fermilab, colliding proton with antiprotons at  $\sqrt{s} = 1.96$  TeV. When completely filled, the  
 LHC nominally contains 2220 bunches in Run 2, compared to 1380 in Run 1 (design: 2200).

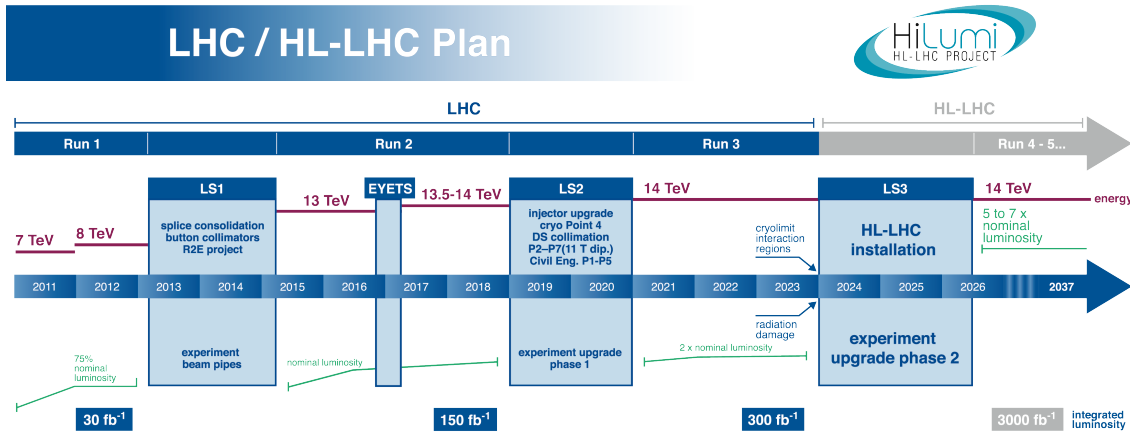


**Figure 2.2:** The HL-LHC timeline. Figure taken from [57].

394

395 Inside the LHC ring [58], the protons are accelerated by the means of radio frequency cavities,  
 396 while 1232 dipole magnets of approximately 15 m long, each weighing 35 t ensure the deflection  
 397 of the beams. The two proton beams circulate in opposite direction in separate pipes inside of  
 398 the magnet. Through the use of a strong electric current in the coils of the magnet, magnetic  
 399 fields are generated and cause the protons to bend in the required orbits. In order for the coil  
 400 to become superconducting and able to produce a strong magnetic field of 8.3 T, the magnet  
 401 structure is surrounded by a vessel. This vessel is filled with liquid Helium making it possible  
 402 to cool down the magnet to 1.9 K. In order to get more focussed and stabilised proton beams,  
 403 additional higher-order multipole and corrector magnets are placed along the LHC beam line.

404 The LHC is home to seven experiments, each located at an interaction point:

- 405 • A Toroidal LHC ApparatuS (ATLAS) [59] and the Compact Muon Solenoid (CMS) [60]  
 406 experiments are the two general purpose detectors at the LHC. They both have a hermetic,  
 407 cylindrical structure and were designed to search for new physics phenomena along with  
 408 precision measurements of the Standard Model. The existence of two distinct experiments  
 409 allows cross-confirmation of any discovery.
- 410 • A Large Ion Collider Experiment (ALICE) [61] and the LHC Beauty (LHCb) [62] experi-  
 411 ments are focusing on specific phenomena. ALICE studies strongly interacting matter  
 412 at extreme energy densities where a quark-gluon plasma forms in heavy ion collisions  
 (Pb-Pb or p-Pb). LHCb searches for differences between matter and antimatter with the  
 413 focus on b physics..

- 415     • The forward LHC (LHCf) [63] and the TOTal cross section, Elastic scattering and diffraction  
 416       dissociation Measurement (TOTEM) [64] experiments are two smaller experiments that  
 417       focus on head on collisions. LHCf consists of two parts placed before and after ATLAS  
 418       and studies particles created at very small angles. TOTEM is placed in the same cavern as  
 419       CMS and measures the total proton-proton cross section and studies elastic and diffractive  
 420       scattering.
- 421     • The Monopoles and Exotics Detector At the LHC (MoEDAL) [65] experiment is situated  
 422       near LHCb and tries to find magnetic monopoles.

For the enhancement of the exploration of rare events and thus enhancing the number of collisions, high beam energies as well as high beam intensities are required. The luminosity [66] is a measurement of the number of collisions that can be produced in a detector per square meter and per second and is the key role player in this enhancement. The LHC collisions create a number of events per second given by

$$N_{\text{event}} = L \sigma_{\text{event}}, \quad (2.1)$$

where  $\sigma_{\text{event}}$  is the cross section of the process of interest and  $L$  the machine instantaneous luminosity. This luminosity depends only on the beam parameters and is for a Gaussian beam expressed as

$$L = \frac{1}{4\pi} N_b n_b f_{\text{rev}} \frac{N_b}{\epsilon_n} \left( 1 + \left( \frac{\theta_c \sigma_z}{2\sigma^*} \right)^2 \right)^{-\frac{1}{2}} \frac{\gamma_r}{\beta^*}. \quad (2.2)$$

423 The number of particles per bunch is expressed by  $N_b$ , while  $n_b$  is the number of bunches  
 424 per beam,  $f_{\text{rev}}$  the revolution frequency,  $\gamma_r$  the relativistic gamma factor,  $\epsilon_n$  the normalized  
 425 transverse beam emittance - a quality for the confinement of the beam,  $\beta^*$  the beta function at  
 426 the collision point - a measurement for the width of the beam,  $\theta_c$  the angle between two beams  
 427 at the interaction point,  $\sigma_z$  the mean length of one bunch, and  $\sigma^*$  the mean height of one bunch.  
 428 In Equation 2.2, the blue part represents the stream of particles, the red part the brilliance, and  
 429 the green part the geometric reduction factor due to the crossing angle at the interaction point.

430 The peak design luminosity for the LHC is  $10^{34} \text{ cm}^{-2}\text{s}^{-1}$ , which leads to about 1 billion proton  
 431 interactions per second. In 2016, the LHC was around 10% above this design luminosity [67].  
 432 The luminosity is not a constant in time since it diminishes due to collisions between the beams,  
 433 and the interaction of the protons and the particle gas that is trapped in the centre of the vacuum  
 434 tubes due to the magnetic field. The diffusion of the beam degrades the emittance and therefore  
 435 also the luminosity. For this reason, the mean lifetime of a beam inside the LHC is around 15  
 436 h. The integrated luminosity - the luminosity provided in a certain time range - recorded by  
 437 CMS and ATLAS over the year 2016 is given in Figure 2.3. In Run 2, the peak luminosity is  
 438  $13\text{-}17 \times 10^{33} \text{ cm}^{-2}\text{s}^{-1}$  compared to  $7.7 \times 10^{33} \text{ cm}^{-2}\text{s}^{-1}$  in Run 1. The recorded luminosity is  
 439 validated for physics analysis keeping  $35.9 \text{ fb}^{-1}$  during 2016 data taking.

440 Multiple proton-proton interactions can occur during one bunch crossing, referred to as  
 441 pileup. On average, the number of pileup events is proportional to the luminosity times the total  
 442 inelastic proton-proton cross section. In 2016, an average of about 27 of pileup interactions  
 443 has been observed in 13 TeV proton collisions at the interaction point of CMS. For 2012, this  
 444 number was about 21 pileup interactions for 8 TeV collisions.

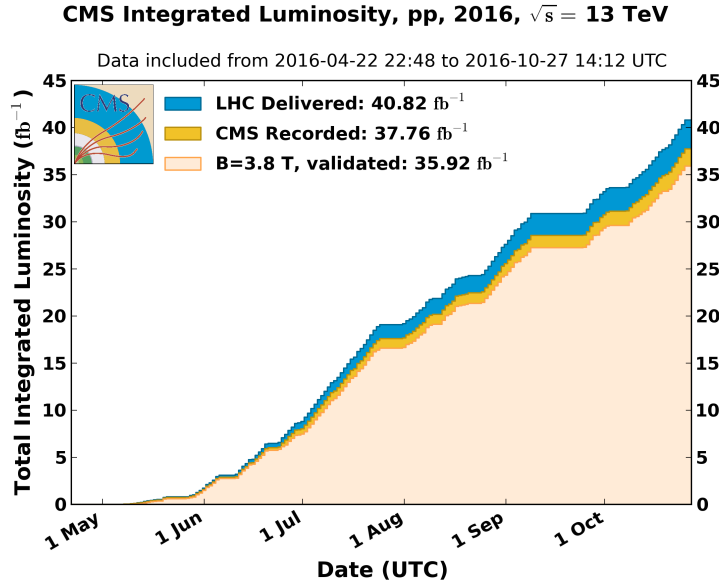


**Figure 2.3:** Cumulative off-line luminosity measured versus day delivered by the LHC (blue), and recorded by CMS (orange), and certified as good physics analysis during stable beams (light orange) during stable beams and for proton collisions at 13 TeV centre-of-mass energy in 2016. [68].

## 445 2.2 The Compact Muon Solenoid

446 At one of the collision points of the LHC, the CMS detector [69–71] is placed. Weighing 14 000 t,  
447 this cylindrical detector is about 28.7 m long and 15 m in diameter. It has an onion like structure  
448 of several specialised detectors and contains a superconducting solenoid with a magnetic field of  
449 3.8 T. Living in a hadronic environment, multi-jet processes produced by the strong interaction  
450 are the main source of background for rare physics processes. Therefore, good identification,  
451 momentum resolution, and charge determination of muons, electrons and photons are one of  
452 the main goals of the CMS detector. Additionally, a good charged particle momentum resolution  
453 and reconstruction efficiency in the inner tracker provides identification for jets coming from b  
454 quarks or tau particles. Also the electromagnetic resolution for an efficient photon and lepton  
455 isolation as well as a good hadronic calorimeter for the missing transverse energy<sup>2</sup> were kept  
456 into account while designing CMS. In Figure 2.4, an overview of the CMS detector is shown.

### 457 2.2.1 CMS coordinate system

The coordinate system used by CMS can be found in Figure 2.5. The origin of the right handed orthogonal coordinate system is chosen to be the point of collisions. The x-axis points towards the centre of the LHC ring such that the y-axis points towards the sky, and the z-axis lies tangent to the beam axis. Since the experiment has a cylindrical shape, customary coordinates are used to describe the momentum  $\vec{p}$  : the distance  $p = |\vec{p}|$ , the azimuthal angle<sup>3</sup>  $\phi \in [-\pi, \pi]$ , the

<sup>2</sup>The missing transverse energy comes from an imbalance in the transverse plane. This will be discussed in Chapter 4.

<sup>3</sup>The azimuthal angle is the angle between the x-axis and the projection in the transverse plane of the momentum  $\vec{p}$ , denoted as  $\vec{p}_T$ .

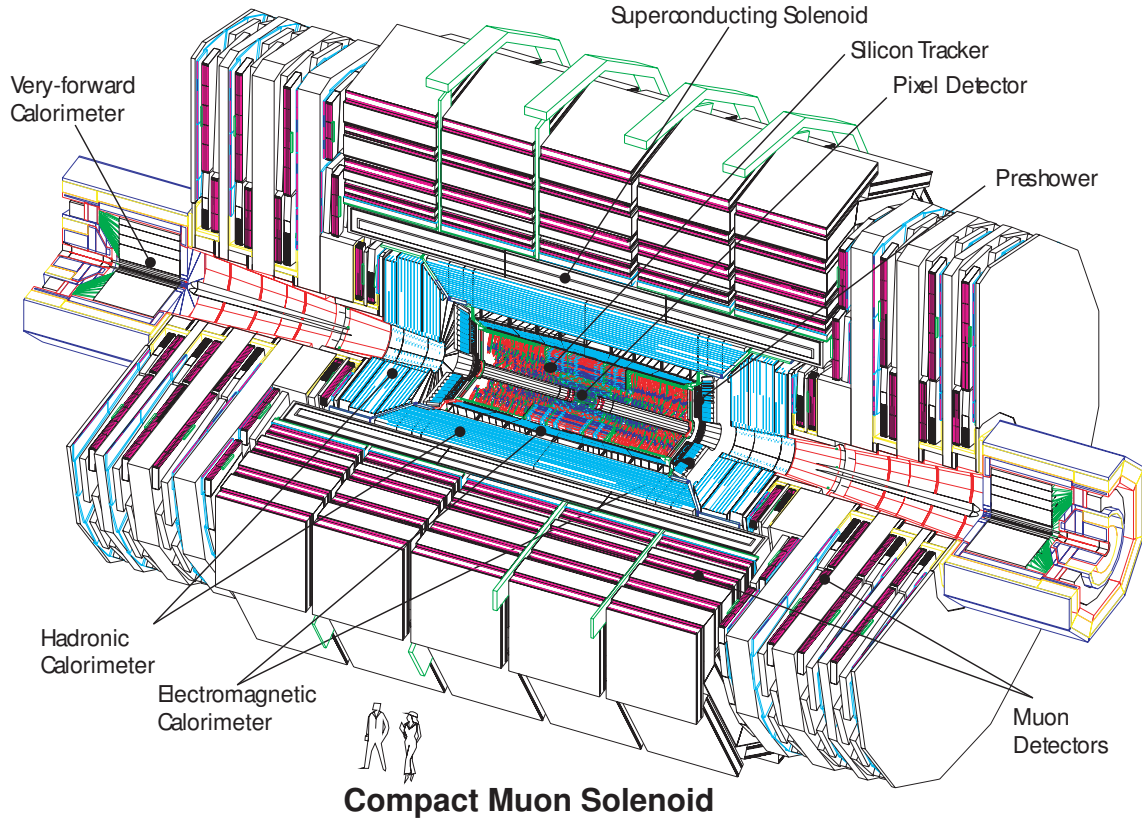


**Figure 2.4:** Mechanical layout of the CMS detector. Figure taken from [72].

pseudo-rapidity<sup>4</sup>  $\eta$  :

$$\eta = -\ln \left( \tan \left( \frac{\theta}{2} \right) \right). \quad (2.3)$$

For the energies considered at the LHC, where  $E \gg m$ , the pseudo-rapidity is a good approximation of the rapidity  $y$

$$y = \frac{1}{2} \ln \left( \frac{E + p_z}{E - p_z} \right), \quad (2.4)$$

458 where the difference of rapidities of two particles is invariant under a Lorentz boost in the  
459 z-direction.

### 460 2.2.2 Towards the heart of CMS

461 The CMS detector can be divided into two parts. A central barrel is placed around the beam  
462 pipe ( $|\eta| < 1.4$ ), and two plugs (endcaps) ensure the hermeticity of the detector. In [Figure 2.4](#)  
463 and [Figure 2.6](#) the onion like structure of the CMS detector is visible. The choice of a solenoid of  
464 12.9 m long and 5.9 m diameter gives the advantage of bending the particle trajectories in the

---

<sup>4</sup>The pseudo rapidity is expressed by the polar angle  $\theta$  between the direction of  $\vec{p}$  and the beam.

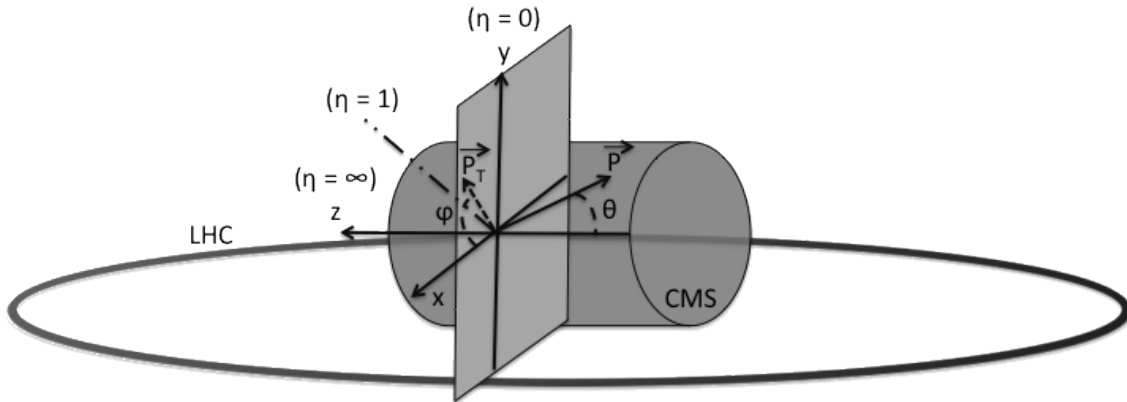


**Figure 2.5:** Representation of the coordinate system used by CMS. The point of origin is put at the collision point. The x-axis points towards the centre of the LHC ring such that the z-axis lies tangent to the beam axis.

465 transverse plane. The hadronic calorimeter (Section 2.2.2.3), the electromagnetic calorimeter  
 466 (Section 2.2.2.4) and the tracker (Section 2.2.2.5) are within the solenoid (Section 2.2.2),  
 467 while the muon chambers (Section 2.2.2.1) are placed outside the solenoid. The data used for  
 468 the search presented in this thesis is collected after the long shutdown 1. After discussing each  
 469 part of CMS in their Run 1 configuration, Section 2.2.4 elaborates on their different upgrades  
 470 for the data collected in Run 2.

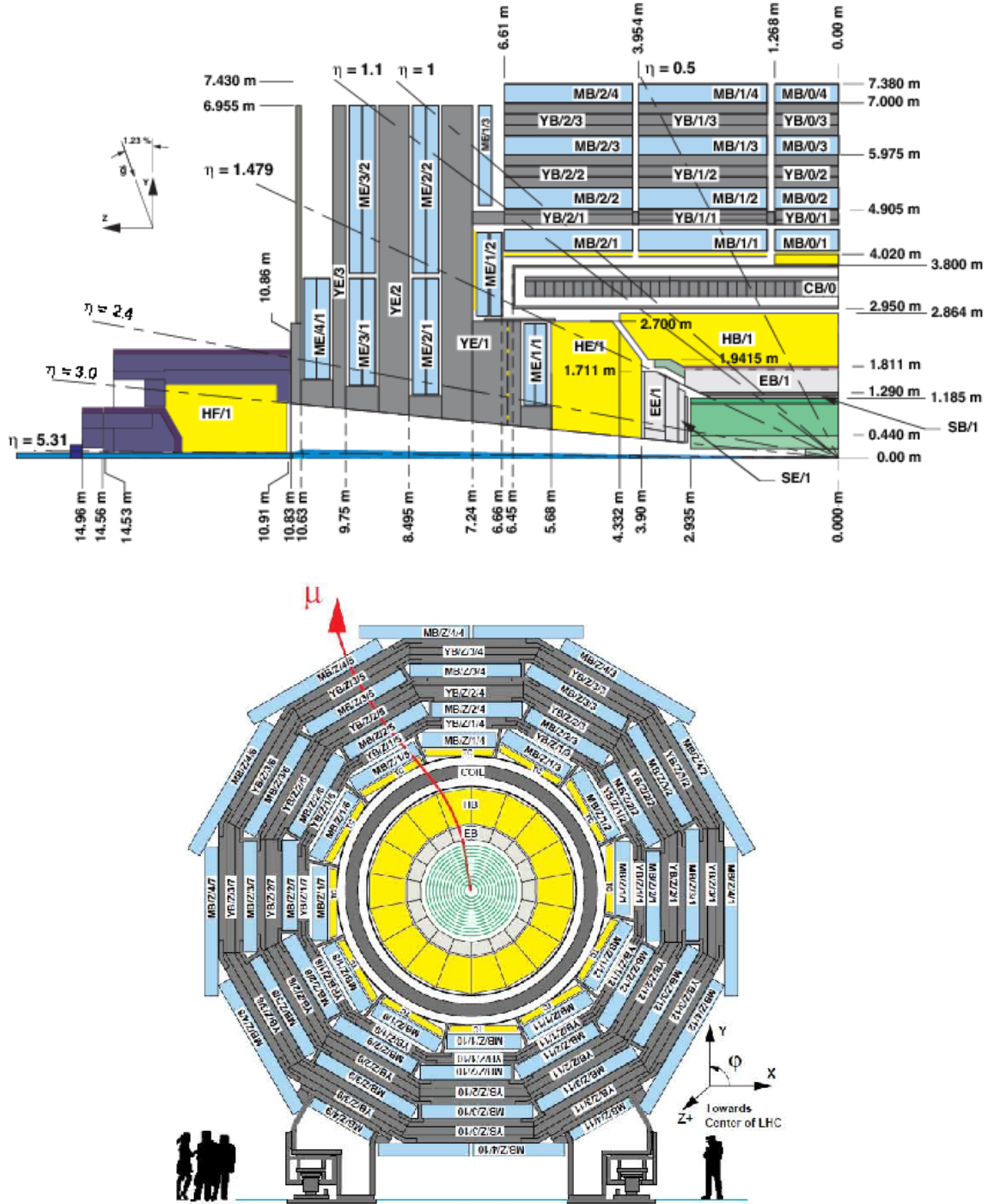


**Figure 2.6:** Schematic view of the CMS detector in the Run 1 configuration. The longitudinal view of one quarter of the detector is given at the top, while the transversal view is shown at the bottom. The muon system barrel elements are denoted as MBZ/N/S, where Z=−2...+2 is the barrel wheel number, N=1...4 the station number and S=1...12 the sector number. Similarly, the steel return yokes are denoted as YBZ/N/S. The solenoid is denoted as CB0, while the hadronic calorimeter is denoted as HE (endcap)/ HB (barrel)/HF (forward) and the electromagnetic calorimeter as EE (endcap)/EB (barrel). The green part represents the tracking system (tracker + pixel). Figure taken from [73].

471 **2.2.2.1 Muon system**

472 The outermost part of CMS consists of the muon system. The magnet return yoke is interleaved  
 473 with gaseous detector chambers for muon identification and momentum measurement. The  
 474 barrel contains muon stations arranged in five separate iron wheels, while in the endcap four  
 475 muon stations are mounted onto three independent iron discs on each side. Each barrel wheel  
 476 has 12 sectors in the azimuthal angle.

477 The muon system is divided into three parts, shown in [Figure 2.7](#). The muon rate and neutron  
 478 induced backgrounds are small and the magnetic field is very low for the barrel, thus CMS can  
 479 use drift tube (DT) chambers. For the endcaps however, the muon and background flux is much  
 480 higher and there is a need to use cathode strip chambers (CSC) which are able to provide a  
 481 faster response, higher granularity and have a better resistance against radiation. In order to  
 482 form a redundant trigger system, resistive plate chambers (RPC) are added. This makes a total  
 483 of 250 DT, 540 CSC and 610 RPC chambers. In [Figure 2.6](#) the arrangement is shown.

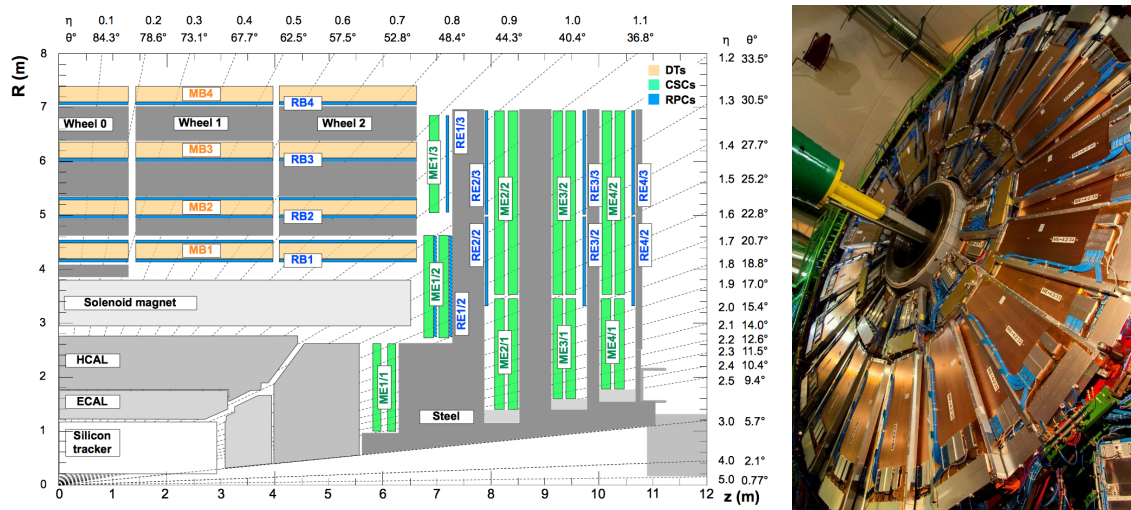


**Figure 2.7:** (Left) Schematic view of one quarter of the CMS muon system in the Run 1 configuration. The cathode strip chambers (CSC) are shown in green, the drift tubes (DT) are shown in yellow, while the resistive plate chambers (RPC) are shown in blue. Figure taken from [73]. (Right) Cathode strip chambers (ME+4/2 chambers on YE+3). Photo taken from [74].

483

484 Providing a measurement for  $|\eta| < 1.2$ , the DT chambers in the barrel are on average  
 485  $2 \times 2.5 \text{ m}^2$  in size and consist of 12 layers of DT cells<sup>5</sup> arranged in three groups of four. The  
 486  $r\phi$  coordinate is provided by the two outside groups, while the middle group measures the  
 487  $z$  coordinate. For the outer muon station, the DT chambers contain only 8 layers of DT cells,  
 488 providing a muon position in the  $r\phi$  plane. There are four CSC stations in each endcap, providing  
 489 muon measurements for  $0.9 < |\eta| < 2.4$  (Run 1 configuration). These CSCs are multi-wired  
 490 proportional chambers that consist of 6 anode wire planes crossed by 7 copper strips cathode  
 491 panels in a gas volume. The  $r$  coordinate is provided by the copper strips, while the  $\phi$  coordinate  
 492 comes from the anode wires, giving a two dimensional position measurement. There are six

<sup>5</sup>The DT cells are 4 cm wide gas tubes with positively charged stretched wires inside.

493 layers of RPCs in the barrel muon system and one layer into each of the first three stations  
 494 of the endcap. They are made from two high resistive plastic plates with an applied voltage  
 495 and separated by a gas volume. Read out strips mounted on top of the plastic plates detect the  
 496 signal generated by a muon passing through the gas volume. The RPCs provide a fast response  
 497 with a time resolution of 1 ns and cover a range of  $|\eta| < 1.8$  for the Run 1 configuration.

498 The muon system provides triggering on muons, identifying muons and improves the momen-  
 499 tum measurement and charge determination of high  $p_T$  muons. On top of the muon system,  
 500 a fraction of the muon energy is deposited in the electromagnetic calorimeter, the hadronic  
 501 calorimeter, and outer calorimeter. The high magnetic field enables an efficient first level trigger  
 502 and allows a good momentum resolution of  $\Delta p/p \approx 1\%$  for a  $p_T$  of 100 GeV and  $\approx 10\%$  for a  
 $p_T$  of 1 TeV. There is an efficient muon measurement up to  $|\eta| < 2.4$ .

**NOTE:** 503  
check num-  
bers for Run  
2 504

### 2.2.2.2 Solenoid

505 Making use of the knowledge of previous experiments like ALEPH and DELPHI at LEP and H1  
 506 at HERA, CMS choose for a large super conducting solenoid with a length of 12.9 m and a  
 507 inner bore of 5.9 m [71]. With 2 168 turns, a current of 18.5 kA resulting in a magnetic field of  
 508 3.8 T, and a total energy of 2.7 GJ, a large bending power can be obtained for a modestly-sized  
 509 solenoid. In order to ensure a good momentum resolution in the forward regions, a favourable  
 510 length/radius was necessary. In [Figure 2.8](#), a photo of the CMS solenoid is shown.

511 The solenoid uses a high-purity aluminium stabilised conductor with indirect cooling from  
 512 liquid helium, together with fully epoxy impregnation. A four-layer winding is implemented that  
 513 can withstand an outward pressure of 64 atm. The NbTi cable is co-extruded by pure aluminium  
 514 that acts as a thermal stabilizer and has an aluminium alloy for mechanical reinforcement. The  
 515 return of the magnetic field is done by five wheels, noted by YB in [Figure 2.6](#).

### 516 2.2.2.3 Hadronic calorimeter

517 The hadronic calorimeter (HCAL) is dedicated to precisely measure the energy of charged and  
 518 neutral hadrons via a succession of absorbers and scintillators. This makes it crucial for physics  
 519 analyses with hadronic jets or missing transverse energy. The HCAL barrel extends between  
 520  $1.77 < r < 2.95$  m, where  $r$  is the radius in the transverse plane with respect to the beam. Due  
 521 to space limitations, the HCAL needs to be as small as possible and is made from materials  
 522 with short interaction lengths<sup>6</sup>. On top of this, the HCAL should be as hermetic as possible and  
 523 extend to large absolute pseudo rapidities such that it can prove a good measurement of the  
 524 missing transverse energy.

525 The quality of the energy measurements is dependent on the fraction of the hadronic shower  
 526 that can be detected. Therefore, the HCAL barrel (HB) inside the solenoid is reinforced by an  
 527 outer hadronic calorimeter between the solenoid and muon detectors (HO, see [Figure 2.9](#)), using  
 528 the solenoid as extra absorber. This increases the thickness to 12 interaction lengths. The HB

<sup>6</sup>Here the interaction length is the nuclear interaction length and this is the length needed for absorbing 36.7% of the relativistic charged particles. For the electromagnetic calorimeter this is defined in radiation length  $X_0$ . The radiation length is the mean distance over which a high energy electron loses all but  $1/e$  of its energy by bremsstrahlung.

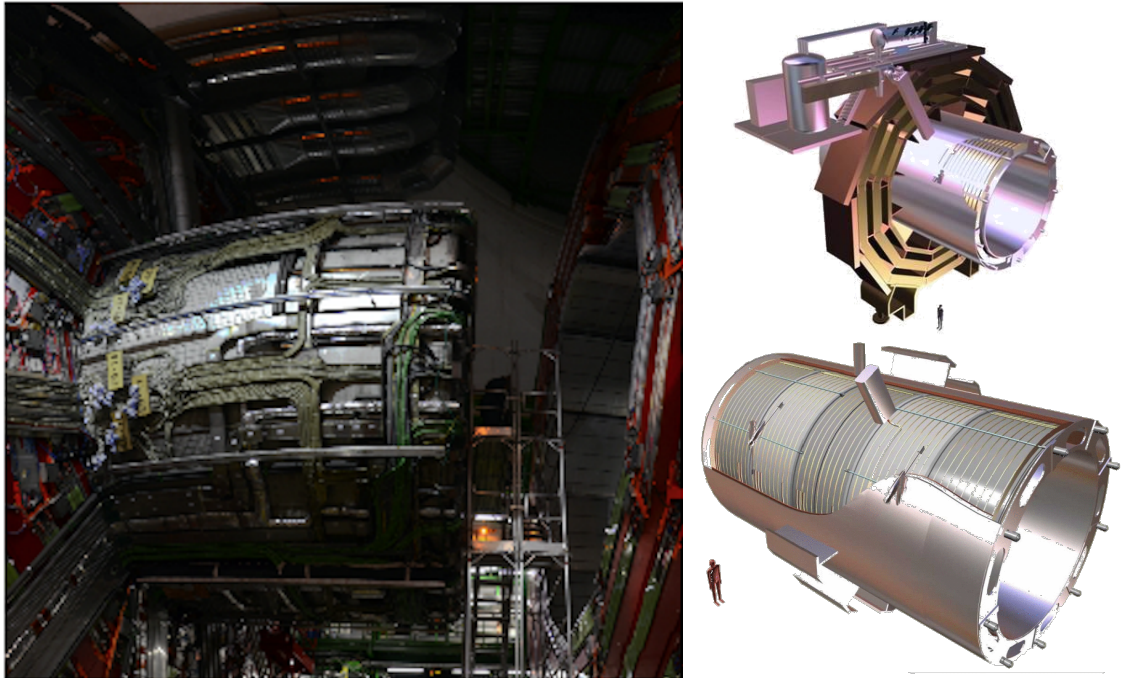


**Figure 2.8:** (Left) CMS solenoid during the long shutdown in 2013. (Right) An impression of the solenoid magnet taken from [75].

529 and HO provide measurements for  $|\eta| < 1.3$ , while an endcap on each side (HE,  $1.3 < |\eta| < 3$ )  
 530 and a forward calorimeter (HF,  $3.0 < |\eta| < 5.2$ ) extend the pseudo rapidity range.

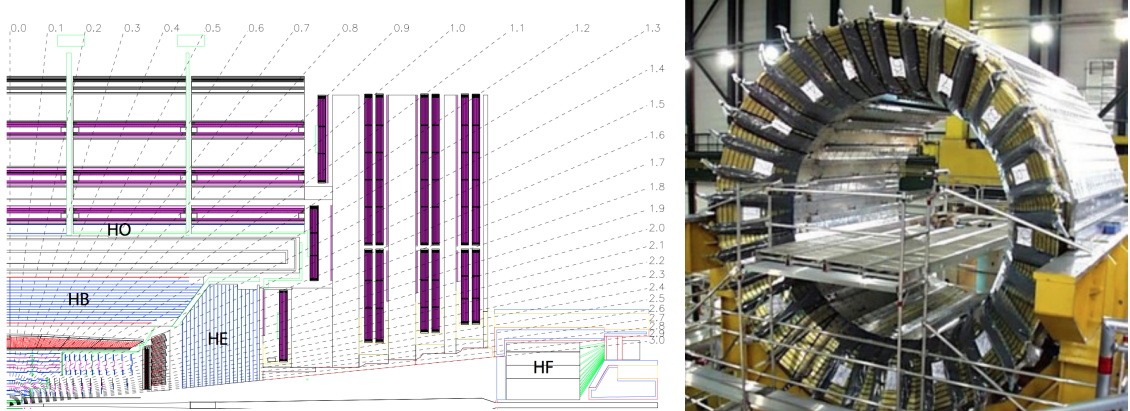


**Figure 2.9:** (Left) Longitudinal view of the CMS detector showing the locations of the HB, HE, HO, and HF calorimeters. Figure taken from [60]. (Right) CMS barrel calorimeter. Photo taken from [76].

531 The HB is made of 16 absorber plates where most of them are built from brass and others are  
 532 made from stainless steel and is about five to ten interaction lengths thick. It is divided in  $\eta \times \phi$   
 533 towers and contains 2592 read out channels. The HO complements the HB and extends the  
 534 reach up to twelve interaction lengths. This subsystem contains 2160 read out channels. The HE  
 535 is also composed of brass absorber plates and has a thickness corresponding to approximately

ten interaction lengths, with 2592 read out channels.. The HF experiences intense particle fluxes with an expected energy of 760 GeV deposited on average in a proton interaction at a centre-of-mass of 14 TeV, compared to 100 GeV in the rest of the detector. Therefore, these are Cherenkov light detectors made of radiation hard quartz fibres. The main causes of such large energy events are high energy muons and charged particles from late showering hadrons. During Run 1, it became clear that the glass windows of the photon multiplier tubes (PMTs) had to be replaced which was done during LS1 [77]. The HF represents 1728 read out channels.

The HCAL and electromagnetic calorimeter combined can measure the hadron energy with a resolution  $\Delta E/E \approx 100\% \sqrt{E[\text{GeV}]} + 5\%$ .

#### 2.2.2.4 Electromagnetic calorimeter

The electromagnetic calorimeter (ECAL) is designed to measure the energy of photons and electrons and covers  $|\eta| < 3$ . It is an hermetic, homogeneous detector and consists of 75 848 lead tungstate ( $\text{PbWO}_4$ ) crystals. These crystals have a fast response time - 80% of the light is emitted within 25 ns - and are radiation hard. The electromagnetic showers produced by passing electrons or photons ionize the crystal atoms which emit a blue-green scintillation light, that is collected by silicon avalanche photodiodes (APDs) in the barrel and vacuum phototriodes (VPTs) in the endcaps. The crystals and the APD response is sensitive to temperature changes and require a stable temperature.

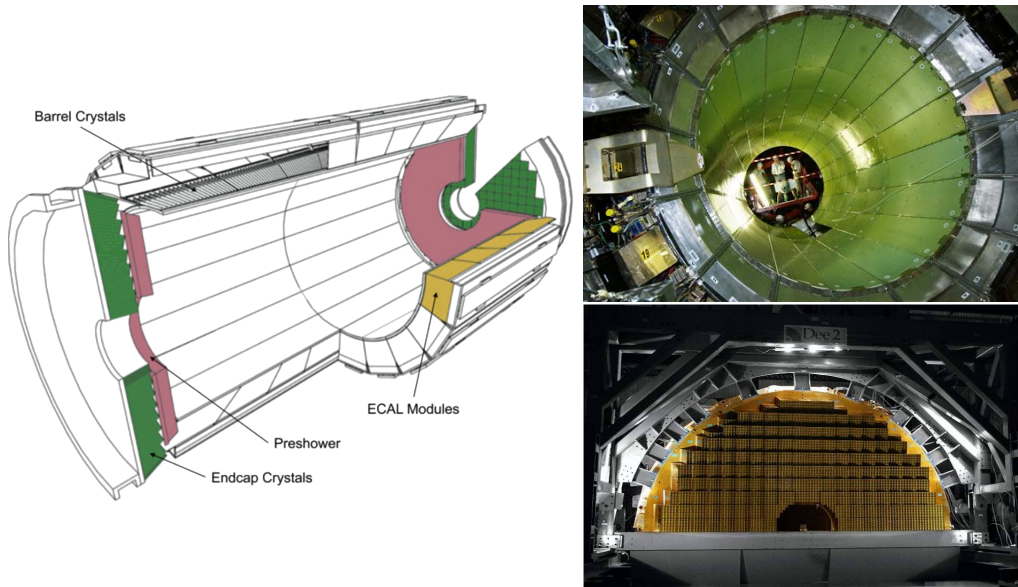


**Figure 2.10:** (Left) Schematic cross section of the electromagnetic calorimeter taken from [60]. (Right top) The ECAL barrel during construction [78]. (Right bottom) One half of an EE [79].

There are three parts: a central barrel (EB), an endcap region (EE) and a preshower (ES) (Figure 2.10). The EB has an inner radius of 129 cm and corresponds to a pseudo rapidity of  $0 < |\eta| < 1.479$ . At a distance of 314 cm from the vertex and covering a pseudo rapidity of  $1.479 < |\eta| < 3.0$ , are the EE. They consist of semi-circular aluminium plates from which structural units of  $5 \times 5$  crystals (super crystals) are supported. The ES is placed in front of

559 the crystal calorimeter over the endcap pseudo rapidity range with two planes of silicon strip  
 560 detectors as active elements.

The electromagnetic shower will typically involve more than one channel. More than 90% of the energy of a 35 GeV electron or photon is contained in a  $5 \times 5$  matrix of crystals. Therefore, a clustering algorithm is performed in order to associate the energy deposits to the particles impinging the calorimeter. The achieved precision [80] for the barrel is  $2 \times 10^{-3}$  rad in  $\phi$  and  $10^{-3}$  in  $\eta$ . For the endcaps this is  $5 \times 10^{-3}$  rad in  $\phi$  and  $2 \times 10^{-3}$  in  $\eta$ . The energy is reconstructed by a supercluster algorithm, taking into account energy radiated via bremsstrahlung or conversion [60]. The energy resolution is given by

$$\frac{\sigma(E)}{E} = \frac{2.8\%}{\sqrt{E}} \oplus \frac{0.128}{E(\text{GeV})} \oplus 0.3\%, \quad (2.5)$$

561 in the absence of a magnetic field, where the contributions come from the stochastic, noise and  
 562 constant terms respectively. The dominating term is the constant term ( $E_{\text{shower}} \approx 100$  GeV)  
 563 and thus the performance is highly dependent on the quality of calibration and monitoring .

#### 564 2.2.2.5 Inner tracking system and operations

565 The tracking system (tracker) [81] is the detecting unit closest to the point of interaction.  
 566 Responsible for the reconstruction of trajectories from charged particles with  $|\eta| < 2.5$  that  
 567 are bent by the magnetic field, it provides a measurement of the momentum. The tracker is  
 568 also responsible for the determination of the interaction point or vertex. It should be able to  
 569 provide high granularity as well as fast read out, and be able to endure high radiation. For these  
 570 reasons, the CMS collaboration choose silicon detector technology.

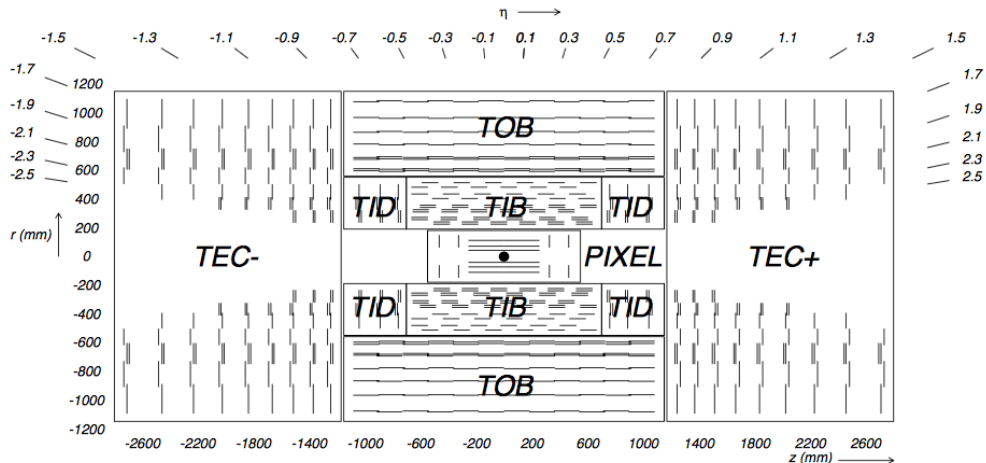


**Figure 2.11:** Schematic cross section through the CMS tracker. Each line represents a detector module. Double lines indicate back-to-back modules that deliver stereo hits. Figure taken from [60].

571 The tracking system consists of a cylinder of 5.8 m long and 2.5 m in diameter. It is immersed  
 572 in a co-axial magnetic field of 3.8 T provided by the solenoid. As shown in Figure 2.11, the  
 573 tracker is built up from a large silicon strip tracker with a small silicon pixel tracker inside. The

574 inner pixel region ( $4.4 < r < 10.2$  cm), gets the highest flux of particles. Therefore, pixel silicon  
 575 sensors of  $100 \times 150 \mu\text{m}^2$  are used. It consists of three cylindrical barrels that are complemented  
 576 by two discs of pixel modules at each side. The silicon strip tracker ( $20 < r < 116$  cm) has three  
 577 subdivisions. The Tracker Inner Barrel and Discs (TIB, TID, see [Figure 2.13](#)) are composed  
 578 of four barrel layers accompanied by three discs at each end. The outer part of the tracker -  
 579 Tracker Outer Barrel (TOB) - consists of 6 barrel layers. In the outer discs, there are nine discs  
 580 of silicon sensors, referred to as Tracker End Caps (TEC).



**Figure 2.12:** The pixel barrel being re-installed after the Long Shutdown in 2015, around the beam pipe at CMS [82].



**Figure 2.13:** First half of the inner tracker barrel, consisting of three layers of silicon modules [83].

581 The pixel detector, shown in [Figure 2.12](#), has 1440 modules that cover an area of about  $1 \text{ m}^2$   
 582 and have 66 million pixels. It provides a three-dimensional position measurement of the hits  
 583 arising from the interaction from charged particles with the sensors. In transverse coordinate  
 584 ( $r\phi$ ), the hit position resolution is about  $10 \mu\text{m}$ , while  $20\text{-}40 \mu\text{m}$  is obtained in the longitudinal  
 585 coordinate ( $z$ ). The sensor plane position provides the third coordinate. The TIB/TID, shown in  
 586 [Figure 2.13](#), delivers up to four  $r\phi$ -measurements using  $320 \mu\text{m}$  thick silicon micro-strip sensors.  
 587 These sensors are placed with their strips parallel to the beam axis in the barrel and radial  
 588 in the discs. In the TIB, the first two layers have a strip pitch of  $80 \mu\text{m}$ , while the remaining  
 589 two have a strip pitch of  $120 \mu\text{m}$ . This leads to a respective single point resolution of  $23 \mu\text{m}$   
 590 and  $35 \mu\text{m}$ . For the TID, the pitch varies between  $100 \mu\text{m}$  and  $141 \mu\text{m}$ . The TOB provides six  
 591  $r\phi$ -measurements with a single point resolutions of  $53 \mu\text{m}$  in the first four layers, and  $35 \mu\text{m}$  in  
 592 the last two layers. It consists of  $500 \mu\text{m}$  thick microstrip sensors with strip pitches of  $183 \mu\text{m}$   
 593 (first 4 layers) or  $122 \mu\text{m}$  (last two layers). The TEC provides up to 9  $\phi$ -measurements via 9  
 594 discs consisting of up to 7 rings of silicon microstrip sensors of  $97 \mu\text{m}$  to  $184 \mu\text{m}$  average pitch.

595 A second co-ordinate measurement ( $z$  in the barrel,  $r$  on the discs) is provided through the  
 596 use of a second micro strip detector module mounted back-to-back with a stereo angle of  $100$   
 597 mrad. This is done on the modules in the first two layers and rings of the TIB, TID, and TOB, as  
 598 well as rings 1,2, and 5 of the TECs (blue line in [Figure 2.11](#)). The resolution in the  $z$  direction is  
 599 approximately  $230 \mu\text{m}$  in the TIB and  $530 \mu\text{m}$  in the TOB, and is varying with pitch in the TID  
 600 and TEC. To allow overlay and avoid gaps in acceptance, each module is shifted slightly in  $r$  or  
 601  $z$  with respect to its neighbouring modules within a layer. With this detector layout, at least  
 602 nine points per charged particle trajectory can be measured in an  $|\eta|$  range up to 2.4, where at  
 603 least four of them being two dimensional. The CMS silicon tracker provides 9.3 million readout  
 604 channels and covers an active area of about  $198 \text{ m}^2$ .

605 **2.2.3 Data acquisition**

606 At a design luminosity of  $10^{34} \text{ cm}^{-2}\text{s}^{-1}$ , the proton interaction rate exceeds 1 GHz. Given the  
 607 large size of an event (about 1 MB), the high crossing rate, and that typically tens of collisions  
 608 happen at the same time, it is impossible for the CMS experiment to store all the data generated.  
 609 In order to deal with the large amount of data, a two level trigger system has been put in place.  
 610 The first level (Level-1) is a custom hardware system, while a second high level trigger (HLT) is  
 611 software based running on a large farm of computers.

612 **CMS Level-1 Trigger**

613 The Level-1 Trigger has to be a flexible, maintainable system, capable of adapting to the  
 614 evolving physics programme of CMS [84]. Its output rate is restricted to 100 kHz imposed  
 615 by the CMS readout electronics. It is implemented by custom hardware and selects events  
 616 containing candidate objects - e.g. ionization deposits consistent with a muon, or energy clusters  
 617 corresponding to an electron / photon / tau lepton / missing transverse energy / jet. Collisions  
 618 with large momenta can be selected by using scalar sum of the transverse momenta of the jets.

619 By buffering the raw data from the CMS subdetectors in front-end drivers, the Level-1 Trigger  
 620 has a pipeline memory of 3.2  $\mu\text{s}$  to decide whether to keep an event or reject it. The trigger  
 621 primitives (TP) from the calorimeters and muon detectors are processed in several steps and  
 622 combined into a global trigger. This information is then combined with the input from the other  
 623 subsystems for the HLT. The separate inputs are synchronized to each other and the LHC orbit  
 624 clock and sent to the global trigger module. Here, Level-1 Trigger algorithms are performed  
 625 within 1  $\mu\text{s}$  to decide whether to keep the event.

626 **CMS HLT Trigger**

627 The HLT is an array of commercially available computers with a programmable menu that has  
 628 an output rate of on average 400 Hz for off-line event storage. The data processing is based on  
 629 an HLT path. This is a set of algorithmic steps to reconstruct objects to define selection criteria.  
 630 Here, the information of all subdetectors can be used to perform algorithms on higher level  
 631 reconstructed objects.

632 **2.2.4 Phase 1 upgrades**

633 Before the start of taking collision data for 13 TeV operations on 3 June 2015, CMS had a  
 634 long shutdown (LS1) [85]. During this shutdown, the section of the beryllium beam pipe  
 635 within CMS was replaced by a narrower one. This operation required the pixel detector to be  
 636 removed and reinserted into CMS. During Run 2, higher particle fluxes with respect to Run  
 637 1 are expected. To avoid longterm damage caused by the intense particle flux at the heart of  
 638 CMS, the tracker is been made ready to operate at much lower temperature than during Run 1.  
 639 The electromagnetic calorimeter preshower system was damaged during Run 1, therefore the  
 640 preshower discs were removed, repaired and reinstalled successfully inside CMS in 2014. To  
 641 help the discrimination between interesting low momentum muons coming from collisions and  
 642 muons caused by backgrounds, a fourth triggering and measurement station for muons was  
 643 added in each of the endcaps. Several new detectors were installed into CMS for measuring the  
 644 collision rate within the detector and to monitor beam related backgrounds.

645 During the LS1, the muon system underwent major upgrades [86, 87]. In the fourth station  
 646 of each endcap, the outermost rings of CSC and RPC chambers were completed, providing an  
 647 angular coverage of  $1.2 < |\eta| < 1.8$  for Run 2, increasing the system redundancy, and allowing  
 648 tighter cuts on the trigger quality. In order to reduce the environmental noise, outer yoke discs  
 649 have been placed on both sides for the endcaps. At the innermost rings of the first station,  
 650 the CSCs have been upgraded by refurbishing the readout electronics to make use of the full  
 651 detector granularity instead of groups of three as was the case for Run 1. In Figure 2.7 (right),  
 652 the refurbishing of the CSCs is shown.

653 Since the HF experiences intense particle fluxes, it became clear during Run 1 that the glass  
 654 windows of the PMTs need replacing. For the ECAL in Run 1, the energy reconstruction happened  
 655 via a weighted sum of the digitized samples [88]. For Run 2 however, the reconstruction had  
 656 to be made more resistant for out of time pile up and a multi-fit approach has been set into  
 657 place. In this approach, the pulse shape is modelled as a sum of one in-time pulse plus the out  
 658 of time pulses [80]. The energy resolution is better than 2% in the central barrel region and  
 659 2-5 % elsewhere.

During the first data taking period of the LHC (2010 to 2013), the tracker operated at +4°C. With the higher LHC beam intensities from 2015 onwards, the tracker needs to be operated at much lower temperatures. The reason for this is that with intense irradiation, the doping concentration changes, the leakage current increases proportional to the fluence and the charge collection efficiency decreases due to charge trapping. Mostly the leakage current ( $I$ ) is affected by the temperature change:

$$I \propto T^2 e^{-\frac{E_g}{2kT}}, \quad (2.6)$$

660 where  $T$  is the operating temperature,  $E_g$  the band gap and  $k$  the Boltzmann constant. There is  
 661 approximately a factor 15 between the leakage currents at room temperatures and at -10 °C.

662 During the LS1, the CMS cooling plant was refurbished [89] and the fluorocarbon cooling  
 663 system overhauled. To help to suppress the humidity inside the tracker, new methods for vapour  
 664 sealing and insulation were applied. Furthermore, several hundred high-precision sensors are  
 665 used to monitor the humidity and temperature. In order to get as dry air as possible, a new  
 666 dry-gas plant provides eight times more dry gas (air or nitrogen) than during the first run, and  
 667 allows regulation of the flow. As a final addition, the cooling bundles outside the tracker are  
 668 equipped with heater wires and temperature sensors in order to maintain safe operations above  
 669 the cavern dew point. For the data taking in 2015-2016, the tracker operated at -15°C.

670 In Run 2, with the increase in centre of mass energy and a higher luminosity, a larger number  
 671 of simultaneous inelastic collisions per crossing is expected with respect to Run 1. For this, the  
 672 CMS Level-1 has been upgraded [90]. All hardware, software, databases and the timing control  
 673 system have been replaced for Run 2, where the main changes are that the muon system now  
 674 uses the redundancy of the muon detector system earlier to make a high resolution muon trigger.  
 675 Other upgrades are that the calorimeter system isn't bound any more for streaming data and  
 676 the global trigger has more Level-1 Trigger algorithms.

677 After the first half of Run 2, the innermost part of detection in CMS (pixel detector) was  
 678 replaced, enhancing the particle tracking capabilities of CMS. The data used in the framework

of this thesis however is from before this upgrade. More information on the Pixel upgrade can be found in Refs. [91, 92].

### 2.2.5 CMS computing model

The selected data is stored, processed and dispersed via the Worldwide Large Hadron Collider Computing Grid (WLCG) [93, 94]. This has a tiered structure that functions as a single, coherent system.

At CERN and the Wigner Research Center for physics, a single Tier-0 is located. The raw data collected by the experiments is archived here, and a first reconstruction of the data is done. This data is then already in a file format usable for physics analysis. Furthermore, it is able to reprocess data when new calibrations become available. The Tier-0 site distributes this data to a total of 14 Tier-1 centres. They carry out data reprocessing and store real data as well as simulated data. The Tier-1 further distributes the data to over 150 Tier-2 centres. These make the data accessible for physics analysis and are also being used for the production of simulated data. The data is made accessible for physicists around the world. For CMS, the Tier-0 site at CERN reconstructs the full collision events and the backup of the data is send to seven Tier-1 computer centres: France, Germany, Italy, Spain, Taiwan, UK, and the US. At the Tier-1 sites the events are again reconstructed using refined calibration constants. The patterns are created and the more complex events are sent to forty Tier-2 centres for specific analysis task.

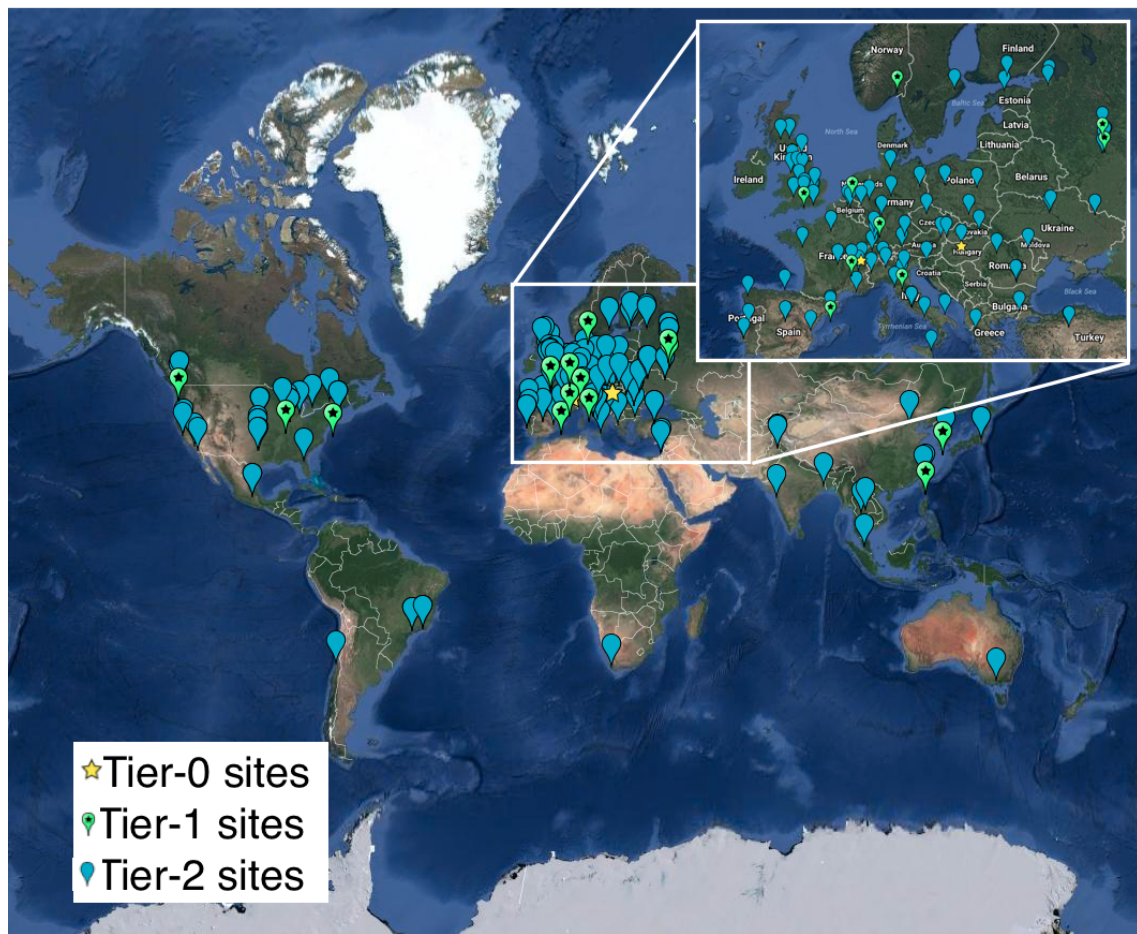


Figure 2.14: Worldwide LHC Computing Grid in 2017 [95].

# Analysis techniques

# 3

698 In order to study the collisions coming from high energy experiments, many tools have been  
 699 developed. In [Section 3.1](#), the physics of hadron collision at high energies are presented. These  
 700 insights are used to generate events via Monte Carlo event generators, explained in [Section](#)  
 701 [3.2](#). Machine learning helps to differentiate between signal- and background like events. In  
 702 [Section 3.3](#), the multivariate technique of boosted decision trees is explained. This yields  
 703 powerful discriminants for separating signal and background events and provides distributions  
 704 for template-based maximum likelihood fits. The fitting method used in the search presented  
 705 in this thesis is discussed in [Section 3.4](#).

## 706 3.1 Hadron collisions at high energies

All partons can be approximated as free when there is sufficiently high momentum transfer in hadron collisions. This makes it possible to treat a hadron-hadron scattering as a single parton-parton interaction. The momentum of the parton can then be expressed as a fraction of the hadron momentum

$$\vec{p}_{\text{parton}} = x \vec{p}_{\text{hadron}}, \quad (3.1)$$

where  $x$  is referred to as the Björken scaling variable. The interaction  $p_A p_B \rightarrow X$  can then be factorised in terms of partonic cross sections  $\hat{\sigma}_{ij \rightarrow X}$  [96]

$$\sigma_{p_A p_B \rightarrow X} = \sum_{ij} \iint dx_1 dx_2 f_i^A(x_1, Q^2) f_j^B(x_2, Q^2) d\hat{\sigma}_{ij \rightarrow X}, \quad (3.2)$$

707 where  $i$  and  $j$  are the partons resolved from protons A and B. The parton density functions  
 708 (PDF) are denoted as  $f_i(x_j, Q^2)$ , and  $Q^2$  is the factorisation scale more commonly denoted as  
 709  $\mu_F$ . This factorisation scale represents the energy at which the hadronic interaction can be  
 710 expressed as a product of the partonic cross section and the process independent PDF. In [Figure](#)  
 711 [3.1](#), the kinematic regions in  $x$  and  $\mu_F$  are shown for fixed target and collider experiments.

712 The parton density functions (PDF) [97–99] represent the momentum distribution of the  
 713 proton amongst its partons at an energy scale  $\mu_F$ . These functions are obtained from global  
 714 fits to data since they can not be determined from first principles. From measurements on deep

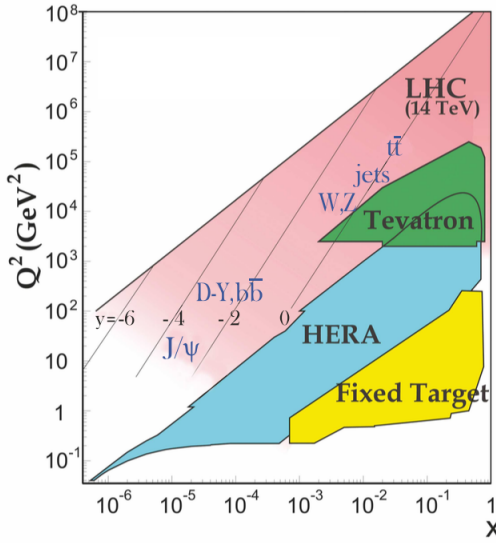


**Figure 3.1:** Kinematic regions in momentum fraction  $x$  and factorisation scale  $Q^2$  probed by fixed-target and collider experiments. Some of the final states accessible at the LHC are indicated in the appropriate regions, where  $y$  is the rapidity. In this figure, the incoming partons have  $x_{1,2} = (M/14\text{TeV})e^{\pm y}$  with  $Q = M$  where  $M$  is the mass of the state shown in blue in the figure. For example, exclusive  $J/\psi$  and  $\Upsilon$  production at high  $|y|$  at the LHC may probe the gluon PDF down to  $x \sim 10^{-5}$ . Figure taken from [6].

715 inelastic scattering using lepton-proton collision by the HERA collider [100], supplemented  
 716 with proton-antiproton collisions from the Tevatron [101], and proton collision data from the  
 717 ATLAS, CMS and LHCb collaborations at the LHC (Run 1) [102] the PDFs are determined and  
 718 included in global PDF sets known as the PDF4LHC recommendation [99]. Their measurement  
 719 at scale  $\mu_F$  is extrapolated to higher energies by use of the DGLAP equations [103]. Once  
 720 these PDFs are known, the cross section of a certain process can be calculated and used as  
 721 input for the Monte Carlo generators used to make the simulated data samples at the LHC. In  
 722 the framework of this thesis, the NLO PDF4LHC15\_100 set is used. This set is an envelope of  
 723 three sets: CT14, MMHT2014 and NNPDF3.0 [99]. As illustration, the dependency of the PDFs  
 724 on the momentum fraction  $x$  is shown for the NNPDF3.0 set on hadronic scale  $\mu_F^2 = 10\text{GeV}^2$   
 725 and LHC scale  $\mu_F^2 = 10^4\text{GeV}^2$  in Figure 3.2. The gluon density dominated for most values of  
 726 the momentum fraction, implying that it is easier to probe gluons than the quarks. When the  
 727 Björken scale is to one, the parton densities of the valence quarks of the proton, up and down  
 728 quarks, dominate over the gluon density. The sea quarks originating from gluon splitting, the  
 729 charm, anti-up, and anti-down quarks, have lower densities in general for the proton. The  
 730 resolution scale  $Q^2$  is typically taken to be the energy scale of the collision. For the top quark pair  
 731 production a scale of  $Q^2 = (350\text{ GeV})^2$  is chosen, meaning that the centre-of-mass energy of the  
 732 hard interaction is about twice the top quark mass. The uncertainty on the parton distributions  
 733 is evaluated using the Hessian technique [104], where a matrix with a dimension identical to  
 734 the number of free parameters needs to be diagonalised. In the case of PDF4LHC15\_100 set, this  
 735 translates into 100 orthonormal eigenvectors and 200 variations of the PDF parameters in the  
 736 plus and minus direction.

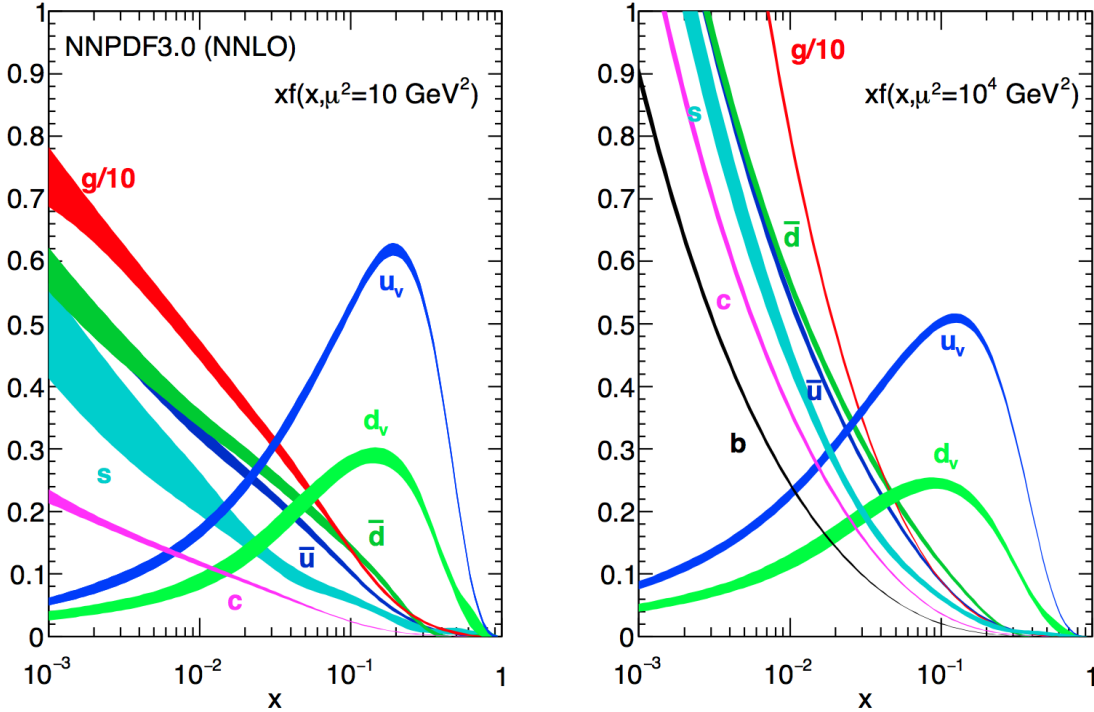


**Figure 3.2:** The momentum fraction  $x$  times the parton distribution functions  $f(x)$ , where  $f = u_v, d_v, \bar{u}, \bar{d}, s, c$ , or  $g$  as a function of the momentum fraction obtained in the NNLO NNPDF3.0 global analysis at factorisation scales  $\mu^2 = 10 \text{ GeV}^2$  (left) and  $\mu^2 = 10^4 \text{ GeV}^2$  (right), with  $\alpha_s(M_Z^2) = 0.118$ . The gluon PDF has been scaled down by a factor of 0.1. Figure taken from [6].

Quantum fluctuations can cause divergences at high energies. This is solved by introducing a renormalization scale  $\mu_R$  to redefine physical quantities, making the theory still able to describe the experimental regime. A consequence of this method is that the coupling constants will run as a function of  $\mu_R$ . Beyond the renormalization scale, the high energy effects such as the loop corrections to propagators (self energy) are absorbed in the physical quantities through a renormalization of the fields. In particular the running behaviour of the strong coupling constant<sup>1</sup>  $\alpha_S$  is found to be

$$\alpha_S = \frac{\alpha_S(\mu_0^2)}{1 + \alpha_S(\mu_0^2) \frac{33-2n_f}{12\pi} \ln\left(\frac{|\mu_R^2|}{\mu_0^2}\right)}, \quad (3.3)$$

with  $n_f$  the number of quarks and  $\mu_0$  the reference scale at which the coupling is known. The current world average of the strong coupling constant at the Z boson mass is  $\alpha_S(\mu_R = m_Z) = 0.1181 \pm 0.0011$  [6]. From Equation 3.3 one can see easily that the coupling strength decreases with increasing renormalization scale, this is known as asymptotic freedom. Additionally, following the behaviour of  $\alpha_S(\mu_R^2)$ , a limit  $\Lambda_{\text{QCD}} \approx 200 \text{ MeV}$  is found for which  $\alpha_S$  becomes larger than one. Under this limit, the perturbative calculations of observables can no longer be done.

<sup>1</sup>The strong coupling constant is defined as  $\alpha_S = \frac{g_S^2}{4\pi}$ .

Cross sections can be written in terms of interacting vertices contributing to the matrix element (ME) originating from elements of a perturbative series [105], allowing them to be expanded as a power series of the coupling constant  $\alpha$

$$\sigma = \sigma_{\text{LO}} \left( 1 + \left( \frac{\alpha}{2\pi} \right) \sigma_1 + \left( \frac{\alpha}{2\pi} \right)^2 \sigma_2 + \dots \right). \quad (3.4)$$

744 Leading order (LO) accuracy contains the minimal amount of vertices in the process, then  
 745 depending on where the series is cut off one speaks of next-to-leading order (NLO), or next-to-  
 746 next-to-leading order (NNLO) accuracy in  $\alpha$ . Predictions including higher order corrections  
 747 tend to be less affected by theoretical uncertainties originating from a variation of the chosen  
 748 renormalization and factorisation scales.

## 749 3.2 Event generation

750 In order to compare reconstructed data with theoretical predictions, collision events are gener-  
 751 ated and passed through a simulation of the CMS detector and an emulation of its readout. For  
 752 the detector simulation, a so-called Full Simulation package [106, 107] based on the Geant4  
 753 toolkit [108] is employed. This allows detailed simulations of the interactions of the particles  
 754 with the detector material.

### 755 3.2.1 Fundamentals of simulating a proton collision

756 The generation of  $\text{pp} \rightarrow \text{X}$  events is subdivided into sequential steps [109–111], as shown in  
 757 [Figure 3.3](#).

758 The interaction of two incoming protons is often soft and elastic leading to events that are not  
 759 interesting in the framework of this thesis. More intriguing are the hard interactions between  
 760 two partons from the incoming protons. The event generation starts from the matrix elements of  
 761 a hard scattering process of interest. The corresponding cross section integral is sampled using  
 762 Monte Carlo techniques and the resulting sample of events reflect the probability distribution  
 763 of a process over its final state phase space. A parton shower (PS) program is then used to  
 764 simulate the hadronisation of final state partons, coming from the sample of events of the hard  
 765 interaction, into hadrons which then decay further. On top of this, radiation of soft gluons or  
 766 quarks from initial or final state partons is simulated. These are respectively referred to as  
 767 initial state radiation (ISR) or final state radiation (FSR). The contributions from soft secondary  
 768 interactions, the so-called underlying event (UE), and colour reconnection effects are also taken  
 769 into account. A brief overview of the employed programs used for the event generation of the  
 770 signal and main background processes used in the search presented in the thesis is given in  
 771 [Section 3.2.2](#).

### 772 3.2.2 Programs for event generation

773 The FEYNRULES package [112] allows for the calculation of the Feynman rules in momentum  
 774 space for any quantum field theory model. By use of a Lagrangian, the set of Feynman rules asso-  
 775 ciated with this Lagrangian is calculated. Via the Universal FeynRules Output (UFO) [113]  
 776 the results are then passed to matrix element generators.

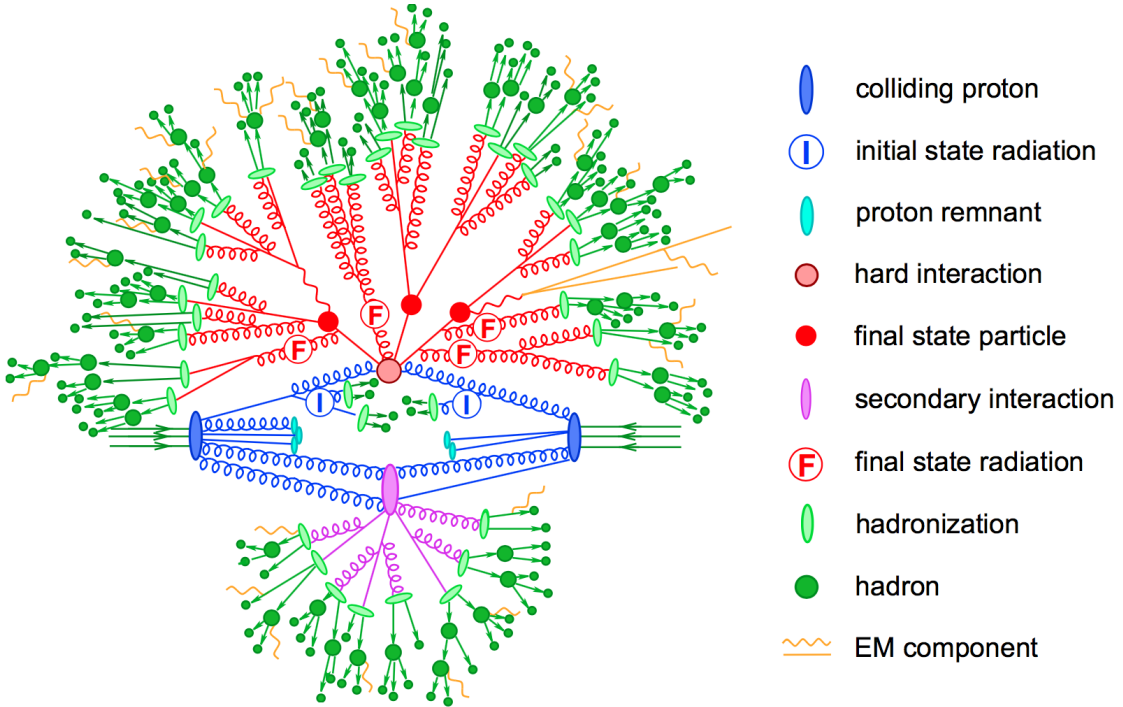


**Figure 3.3:** Sketch of a hadron collision as simulated by a Monte-Carlo event generator. The red blob in the centre represents the hard collision, surrounded by a tree-like structure representing Bremsstrahlung as simulated by parton showers. The purple blob indicates a secondary hard scattering event. Parton-to-hadron transitions are represented by light green blobs, dark green blobs indicate hadron decays, while yellow lines signal soft photon radiation. Figure taken from [111].

777     The MadGraph program [114] is used to interpret the physics model and calculate the cor-  
 778     responding Feynman diagrams and matrix elements. After this, MadEvent [115] is used to  
 779     calculate the corresponding partons. These generated parton configurations are then merged  
 780     with Pythia [116–118] parton showers using the MLM merging scheme [119].

781     The MadGraph5\_aMC@NLO program [120] combines the LO MadGraph [114] and the aMC@NLO  
 782     program into a common framework. This combination supports the generation of samples at  
 783     LO or NLO together with a dedicated matching to parton showers using the MC@NLO [121]  
 784     or FxFx [122] schemes respectively. The FxFx scheme produces a certain fraction of events  
 785     with negative weights originating from the subtraction of amplitudes that contain additional  
 786     emissions from the NLO matrix element to prevent double-counting.

787     The POWHEG box (versions 1 and 2) [123–128] contains predefined implementations of various  
 788     processes at NLO. It applies the POWHEG method for ME- to PS- matching, where the hardest  
 789     radiation generated from the ME has priority over subsequent PS emission to remove the overlap  
 790     with the PS simulation.

791     The JHU generator (version 7.02) [129–132] is used to generate the parton level information  
 792     including full spin and polarization correlations. It is commonly used for studying the spin and  
 793     parity properties of new resonances such as  $ab \rightarrow X \rightarrow VV$ , where  $V = Z, W, \gamma$ .

The generation of events from processes involving the production and decay of resonances creates a computational heavy load, especially at NLO. The narrow width approximation assumes that the resonant particle is on-shell. This factorizes the production and decay amplitude, allowing to perform the simulation of the production and decay of heavy resonances like top quarks or Higgs bosons to be performed in separate steps. The MadSpin program [133] extends this approach and accounts for off-shell effects through a partial reweighting of the events. Additionally, spin correlation effects between production and decay products are taken into account.

802 The Pythia program (versions 6 and 8) [116–118] generates events of various processes at  
 803 LO. However more commonly it is only used for its PS simulation and is then used after other  
 804 LO and NLO event generators to perform subsequent parton showering, hadronisation, and  
 805 simulation of the underlying event. In this thesis the underlying event tunes [134] are the  
 806 CUETP8M2T4, CUETP8M1 and CUETP8M2.

807 The detector response is simulated via the Geant4 [108] program. This program tracks the  
 808 particles through the detector material via a detailed description of the detector and generates  
 809 several hits throughout several sensitive layers. In addition, the response of the detector  
 810 electronics to these hits are simulated.

### 3.2.3 Generating FCNC top-Z interactions

The FCNC processes are generated by interfacing the Lagrangian in Equation 1.36 with MadGraph5\_AMC@NLO by means of the FeynRules package and its Universal FeynRules Output format. The complex chiral parameters are arbitrary chosen to be  $f_{xq}^L = 0$  and  $f_{xq}^R = 1$ . The processes are generated with the MadGraph5\_aMC@NLO (version 2.2.2) and showered with Pythia (version 8.22). The signal consists of two components: events describing the top quark pair production followed by an FCNC decay of one top quark ( $t \rightarrow Zq$ ), and events with the FCNC single top quark production ( $Zq \rightarrow t$ ) for which the top quark decays according the to SM. The leading order generation of the single top quark FCNC process  $tZ+0,1$  jet including a merging technique can not be done since  $tZ+1$  jet also contains contributions from top quark pair FCNC where one quark is decaying in  $tZ$ . Therefore, single top quark and top quark pair processes are generated independently, where the single top quark process is generated without the extra hard jet, and the top quark pair FCNC process is generated with up to two extra jets.

824 The signal rates are estimated by use of the MadGraph5\_aMC@NLO program for estimating the  
 825 partial widths. The anomalous couplings are left free to float for this estimation, and only one  
 826 coupling is allowed to be non-vanishing at a time. The results are presented in [Table 3.1](#).

The anomalous single top quark cross sections are calculated by convolution of the hard scattering matrix elements with the LO order set of NN23L01 [135] partons densities. The NLO effects are modelled by multiplying each LO cross section by a global  $k$ -factor. The LO single top quark production cross section and the global  $k$ -factors for the top-Z production are shown in [Table 3.2](#). The hard scattering events are then matched to parton showers to Pythia to account for the simulation of the QCD environment relevant for hadronic collisions.

**Table 3.1:** Leading order partial widths related to the anomalous decay modes of the top quark, where the new physics scale  $\Lambda$  is given in GeV.

Anomalous coupling	vertex	Partial decay width (GeV)
$\kappa_{tZq}/\Lambda$	tZu	$1.64 \times 10^4 \times (\kappa_{tZu}/\Lambda)^2$
	tZc	$1.64 \times 10^4 \times (\kappa_{tZc}/\Lambda)^2$
	tZu	$1.69 \times 10^{-1} \times (\zeta_{tZu})^2$
	tZc	$1.68 \times 10^{-1} \times (\zeta_{tZc})^2$

**Table 3.2:** Leading order single top quark production cross section at a centre-of-mass of 13 TeV for  $pp \rightarrow tZ$  or  $t\bar{Z}$ , where the new physics scale is given in GeV. The NLO  $k$ -factors [136] are given in the last column.

Anomalous coupling	vertex	Cross section (pb) $pp \rightarrow t + pp \rightarrow \bar{t}$	$\sigma_{pp \rightarrow \bar{t}}/\sigma_{pp \rightarrow t}$	NLO $k$ -factor
$\kappa_{tZq}/\Lambda$	tZu	$1.92 \times 10^7 \times (\kappa_{tZu}/\Lambda)^2$	0.12	1.40
	tZc	$2.65 \times 10^6 \times (\kappa_{tZc}/\Lambda)^2$	0.50	1.40
$\zeta_{tZq}$	tZu	$8.24 \times 10 \times (\zeta_{tZu})^2$	0.14	1.40
	tZc	$1.29 \times 10 \times (\zeta_{tZc})^2$	0.50	1.40

The top quark pair cross sections are derived from the SM  $t\bar{t}$  cross section, calculated with MadGraph5\_aMC@NLO at NLO at a centre-of-mass of 13 TeV ( $\sigma_{t\bar{t}}^{\text{SM,NLO}} = 6.741 \times 10^2 \text{ pb}$ ), and considering the decay  $t\bar{t} \rightarrow (bW^\pm)(Xqt)$ . The branching ratio  $\mathcal{B}(t \rightarrow bW^\pm)$  is assumed to be equal to one and the FCNC branching ratio is calculated as

$$\mathcal{B}(t \rightarrow qX) = \frac{\Gamma_{t \rightarrow qX}}{\Gamma_t^{\text{SM}} + \Gamma_t^{\text{FCNC}}} \approx \frac{\Gamma_{t \rightarrow qX}}{\Gamma_t^{\text{SM}}}, \quad (3.5)$$

833 where  $\Gamma_{t \rightarrow qX}$  is given in Table 3.1,  $\Gamma_t^{\text{SM}} = 1.32 \text{ GeV}$  [47], and the assumption  $\Gamma_t^{\text{FCNC}} \ll \Gamma_t^{\text{SM}}$  is  
834 made. In Table 3.3 the resulting NLO cross sections for the top-Z FCNC interactions are given.

**Table 3.3:** Next to leading order top quark pair cross section for the top-Z FCNC interactions  $t\bar{t} \rightarrow (bW^\pm)(X_{qt})$  with a full leptonic decay at a centre-of-mass of 13 TeV, where  $\sigma_{pp \rightarrow t\bar{t}}^{\text{SM,NLO}} = 6.741 \times 10^2 \text{ pb}$ ,  $\mathcal{B}(Z \rightarrow \ell\bar{\ell}) = 3.36 \times 3 \times 10^{-2}$ , and  $\mathcal{B}(W \rightarrow \ell\nu) = 10.80 \times 3 \times 10^{-2}$ .

Anomalous coupling	vertex	Process	Cross section (pb)
$\kappa_{tZq}/\Lambda$	$tZ_u$	$t\bar{t} \rightarrow (b\ell^+\nu)(\bar{u}\ell^+\ell^-)$	$2.727 \times 10^5 \times (\kappa_{tZu}/\Lambda)^2$
		$t\bar{t} \rightarrow (\bar{b}\ell^-\bar{\nu})(u\ell^+\ell^-)$	$2.727 \times 10^5 \times (\kappa_{tZu}/\Lambda)^2$
	$tZ_c$	$t\bar{t} \rightarrow (b\ell^+\nu)(\bar{c}\ell^+\ell^-)$	$2.726 \times 10^5 \times (\kappa_{tZc}/\Lambda)^2$
		$t\bar{t} \rightarrow (\bar{b}\ell^-\bar{\nu})(c\ell^+\ell^-)$	$2.726 \times 10^5 \times (\kappa_{tZc}/\Lambda)^2$
$\zeta_{tZq}$	$tZ_u$	$t\bar{t} \rightarrow (b\ell^+\nu)(\bar{u}\ell^+\ell^-)$	$2.807 \times (\zeta_{tZu})^2$
		$t\bar{t} \rightarrow (\bar{b}\ell^-\bar{\nu})(u\ell^+\ell^-)$	$2.807 \times (\zeta_{tZu})^2$
	$tZ_c$	$t\bar{t} \rightarrow (b\ell^+\nu)(\bar{c}\ell^+\ell^-)$	$2.807 \times (\zeta_{tZc})^2$
		$t\bar{t} \rightarrow (\bar{b}\ell^-\bar{\nu})(c\ell^+\ell^-)$	$2.807 \times (\zeta_{tZc})^2$

### 3.2.4 Generating SM background events

The SM  $tZq$  sample is generated using the MadGraph5\_aMC@NLO generator (version 2.2.2) [137] at leading order accuracy. The  $t\bar{t}Z$  and triboson samples were generated using the MadGraph5\_aMC@NLO generator (version 2.2.2), interfaced through the dedicated MC@NLO matching scheme [121]. The  $WZ + \text{jets}$  and  $t\bar{t}W$  samples are produced with up to one additional parton at next-to-leading order accuracy using MadGraph5\_aMC@NLO (version 2.2.2) and using FxFx approach [138] for matching and merging. Other minor background are simulated using different generators. The samples of  $t\bar{t}H$ ,  $WW$ ,  $ZZ$ , and single top quark production channels are generated with the POWHEG box (versions 1 and 2) [123–128]. The JHU generator [129–132] is used for the  $tqH$  sample, while the  $tWZ$  sample is generated using MadGraph [114] interfaced with the MLM matching scheme [119]. All events are interfaced to Pythia version 8.22 [118] to simulate parton shower, hadronisation, and underlying event. Additionally, MadSpin is used for the  $tZq$ ,  $WZ + \text{jets}$ ,  $t\bar{t}Z$ ,  $t\bar{t}W$ ,  $tWZ$ , and triboson samples.

The complete list of SM samples is given in Table 3.4, along with their cross sections at a centre-of-mass of 13 TeV. The cross sections without a reference are coming from the generator with which the sample has been made, for some of them the uncertainties are provided by the Generator Group [139]. For each MC sample, the integrated luminosity that the sample represents is estimated as the number of simulated events divided by the cross section of the generated process. This luminosity is then matched to integrated luminosity of  $35.9 \text{ fb}^{-1}$  represented by the data used for analysis. For processes generated with MadGraph5\_aMC@NLO, the effective number of simulated events is used, taking into account positive and negative event weights. In Figure 3.4, a summary is given of the SM cross section measurements performed by the CMS collaboration. These cross sections are all in agreement with their SM predictions.

**Table 3.4:** SM MC samples used in this analysis with their corresponding cross section at a centre-of-mass of 13 TeV and MadGraph5\_aMC@NLO correction C when applicable. The generators used for each sample are indicated and the simulation of the parton shower, hadronisation, and underlying event is done by Pythia version 8.22 [118] for all samples.

Process	Generator	Cross section (pb)	C	Ref.
$WZ \rightarrow 3\ell\nu$	MadGraph5_aMC@NLO+MadSpin	5.26	1.61	[139]
$tZq$ with $Z \rightarrow \ell^+\ell^-$	MadGraph5_aMC@NLO+MadSpin	0.0758	3.77	[139]
$tqH$ with $H \rightarrow ZZ \rightarrow \ell^+\ell^-\ell^+\ell^-$	JHU	$8.80 \cdot 10^{-6}$	-	[139]
$t\bar{t}W + \text{jets}$ with $W \rightarrow \ell\nu$	MadGraph5_aMC@NLO+MadSpin	$0.2043 \pm 0.0020$	1.94	[139]
$t\bar{t}Z \rightarrow 2\ell + 2\nu + \text{other}$ , with $m_{\ell\ell} > 10$ GeV	MadGraph5_aMC@NLO+MadSpin	$0.2529 \pm 0.0004$	2.15	[139]
$t\bar{t}H, \text{no } b\bar{b} \text{ decays}$	POWHEG	0.2151	-	[139]
$t\bar{t}H, b\bar{b} \text{ decays}$	POWHEG	0.2934	-	[139]
$WW \rightarrow 2\ell 2\nu$	POWHEG	12.178	-	[140]
$ZZ \rightarrow 4\ell$	POWHEG	0.3366	-	[139]
$WZZ$	MadGraph5_aMC@NLO+ MadSpin	0.05565	1.14	[139]
$ZZZ$	MadGraph5_aMC@NLO	0.01398	1.17	[139]
single top quark $tWZ$ , with $Z_\mu \rightarrow \ell^+\ell^-$	MadGraph5_aMC@NLO(LO)+MadSpin	0.001123	-	[139]
single top quark t-channel $\bar{t}$	POWHEG+MadSpin	$44.33^{+1.76}_{-1.49}$	-	[139]
single top quark t-channel $t$	POWHEG+MadSpin	$26.38^{+1.32}_{-1.18}$	-	[139]
single top quark $t\bar{W}$	POWHEG	$35.85 \pm 0.90 \text{ (scale)} \pm 1.70 \text{ (PDF)}$	-	[139]
single top quark $tW$	POWHEG	$35.85 \pm 0.90 \text{ (scale)} \pm 1.70 \text{ (PDF)}$	-	[139]
$t\bar{t}$	POWHEG	$831.76^{+19.77+35.06}_{-29.20-35.06}$	-	[139]
$Z/\gamma^* + \text{jets}$ , with $m_{\ell\ell} > 50$ GeV	MadGraph5_aMC@NLO	$3 \times (1921.8 \pm 0.6 \pm 33.2)$	1.49	[139]
$Z/\gamma^* + \text{jets}$ , with $10 \text{ GeV} < m_{\ell\ell} < 50 \text{ GeV}$	MadGraph	18610	-	[139]

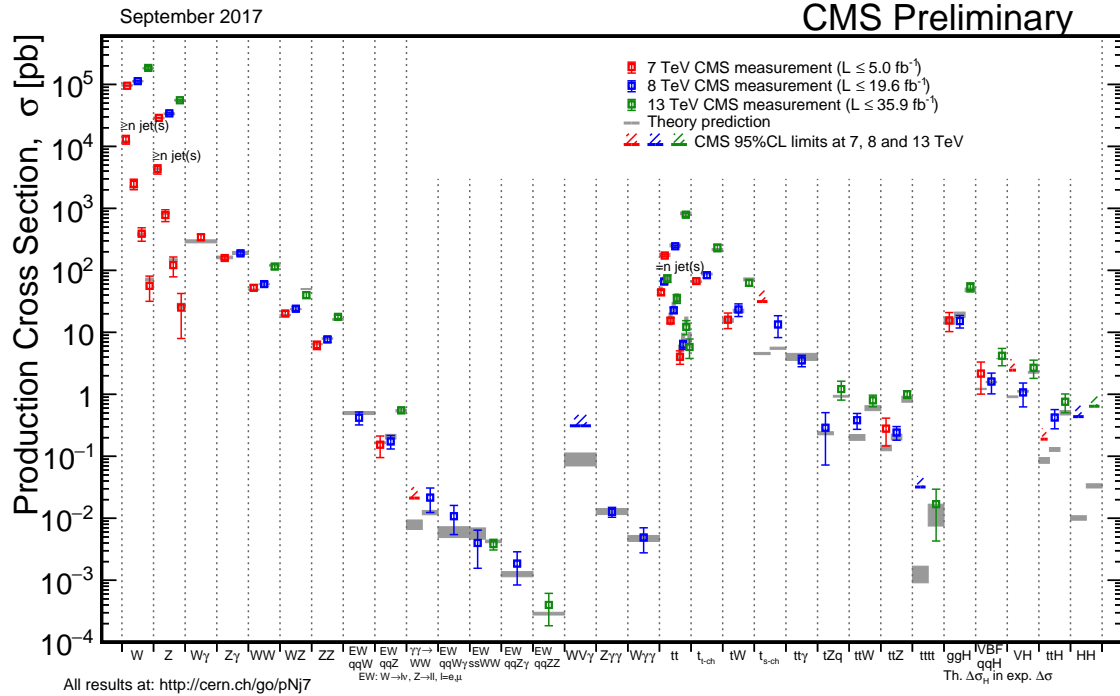


**Figure 3.4:** Summary of the SM cross section measurements performed by the CMS collaboration. Figure taken from [23]

### 3.3 Multivariate analysis techniques: Boosted Decision Trees

The need of processing large quantities of data and discriminating between events with largely similar experimental signatures makes multivariate analysis (MVA) a largely used method in the physics community. Multivariate classification methods based on machine learning techniques are a fundamental ingredient to most analyses. The advantage of using a MVA classifier is that it can achieve a better discrimination power with respect to a simpler analysis based on individual selection criteria or poorly discriminating variables. A risk of using MVA classifiers is overtraining. This happens when there are too many model parameters of an algorithm adjusted to too few data points. This leads to an increase in the classification performance over the objectively achievable one.

There are many software tools that exist for MVA. In this thesis the Tool for Multivariate Analysis (TMVA) [141] is used. This software is an open source project included into ROOT [142]. By training on events for which the classification is known, a mapping function is determined that describes a classification or an approximation of the underlying behaviour defining the target value (regression). In this thesis boosted decision trees (BDT) are employed for the classification of events as implemented in the TMVA framework [141]. This multivariate technique is based on a set of decision trees where each tree yields a binary output depending on the fact that an event is signal- or background-like. This has as advantage that several discriminating variables can be combined into a powerful one-dimensional discriminant D.

877 The decision tree is constructed by training on a dataset for which the outcome is already  
 878 provided, such as simulation datasets with signal and background processes (supervised learn-  
 879 ing). Different trees can be combined into a forest where the final output is determined by the  
 880 majority vote of all trees, so-called boosting. This stabilises the decision trees against statistical  
 881 fluctuations and makes it possible to keep the decision trees very shallow, making the method  
 882 more robust against overtraining. Examples of such boosting algorithms are Adaptive Boosting  
 883 (AdaBoost) and Gradient Boosting [143]. In this thesis Gradient boost is used with a learning  
 884 rate of 0.2-0.3 and the depth of the tree is set to three. Additionally, the Gradient boost is  
 885 used in combination with bagging, so-called stochastic gradient boosting. Bagging smears the  
 886 statistical fluctuations in the training data and therefore stabilises the response of the classifier  
 887 and increases the performance by eliminating overtraining. More information about stochastic  
 888 gradient boosting can be found in Ref. [144].

889 The discriminating power of a BDT is assessed by analysing the receiver operating characteristic  
 890 (ROC) curve. This curve represents the background rejection over the signal efficiency of the  
 891 remaining sample. The area under the curve (AUC) is compared to random guessing in order  
 892 to identify the best classifier can be identified. When the multivariate discriminator has no  
 893 discriminating power, the resulting AUC will be 0%, while 50% means fully separated event  
 classes. In Figure 3.5 examples of ROC curves are shown.

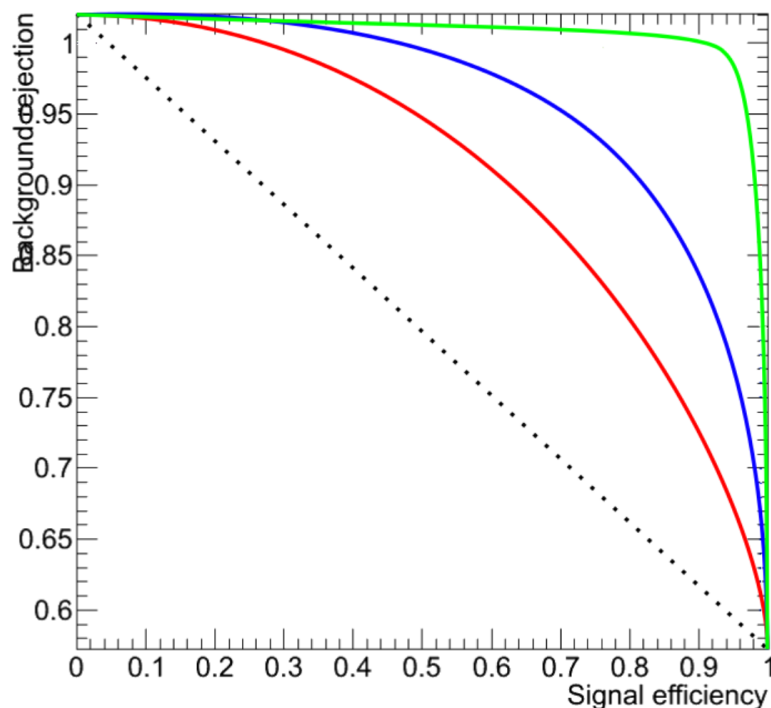


**Figure 3.5:** Example of ROC curves. In this example, the green method is better than the blue one, which is better than the red one. The dashed line represents a case where there is no separation. Figure taken from [145].

### 895 3.4 Statistical methodology

896 The search performed in the framework of this thesis requires the simultaneous analysis of data  
 897 from different decay channels. The statistical methodology used for this search is developed by  
 898 the ATLAS and CMS collaborations in the context of the LHC Higgs Combination group [146–  
 899 149]. The Higgs Combined Tool [150] is a RooStats [151] framework which runs different  
 900 statistical methods. In this section, only the statistical tools necessary for the performed search  
 901 are described [152].

902 The event yields of signal and background processes are denoted as  $s$  and  $b$  respectively.  
 903 These represent event counts in multiple bins or unbinned probability density functions. By  
 904 use of simulation, predictions on both signal and background yields are made the multiple  
 905 uncertainties on these predictions are accounted for by introducing nuisance parameters  $\theta$  such  
 906 that  $s = s(\theta)$  and  $b = b(\theta)$ .

907 The Bayesian and modified classical frequentist statistical approaches are used in high energy  
 908 physics to characterise the absence of a signal. The level of incompatibility of data with a signal  
 909 hypothesis is quantified in terms of confidence levels (CL). The convention is to require a 95%  
 910 CL for excluding a signal. In general limits are not set on the signal cross section directly, but  
 911 are set on the signal strength modifier  $\mu$ . The signal strength modifier is defined such that it  
 912 equally changes all the cross sections of all production mechanisms of the signal by the same  
 913 scale.

In this thesis, the modified frequentist approach [153, 154] for confidence levels that adopts the classical frequentist method to allow nuisance parameters, is used. It constructs a likelihood  $\mathcal{L}(\text{data}|\mu, \theta)$  is as

$$\mathcal{L}(\text{data}|\mu, \theta) = \text{Poisson}(\text{data}|\mu s(\theta) + b(\theta)) \text{pdf}(\tilde{\theta}|\theta). \quad (3.6)$$

914 The probability density function  $\text{pdf}(\tilde{\theta}|\theta)$  describes all sources of uncertainty. In this thesis, all  
 915 sources of uncertainties are assumed to be either 100% correlated or uncorrelated. Partially  
 916 correlated uncertainties are broken down to subcomponents that fit those requirements, allowing  
 917 to include all constraints in the likelihoods in a clean factorised form.

A systematic uncertainty pdf  $\rho(\theta|\tilde{\theta})$  for the nuisance  $\theta$  with nominal value  $\tilde{\theta}$  is used. It reflects the degree of belief of what the true value of the  $\theta$  is. In this thesis, the approach from the Higgs Combined Tool is used where the pdfs  $\rho(\theta|\tilde{\theta})$  are re-interpret as posteriors of real or imaginary measurements  $\tilde{\theta}$

$$\rho(\theta|\tilde{\theta}) \sim \text{pdf}(\tilde{\theta}|\theta) \pi_\theta(\theta), \quad (3.7)$$

918 where  $\pi_\theta(\theta)$  is the hyper prior for the (imaginary) measurements. The the pdfs used by the  
 919 Higgs Combine Tool are described in Ref. [149].

The data in Equation 3.6 represents either the actual observation or pseudo-data to construct sampling distributions. For a binned likelihood, the Poisson probabilities to observe  $n_i$  events in bin  $i$  is given as

$$\text{Poisson}(\text{data}|\mu s(\theta) + b(\theta)) = \prod_i \frac{(\mu s_i(\theta) + b_i(\theta))^{n_i}}{n_i!} e^{-\mu s_i(\theta) - b_i(\theta)}. \quad (3.8)$$

At the LHC, the test statistic is defined as

$$q_\mu = -2 \ln \frac{\mathcal{L}(\text{data} | \mu, \hat{\theta}_\mu)}{\mathcal{L}(\text{data} | \hat{\mu}, \hat{\theta}_\mu)}, \quad (3.9)$$

where the likelihood is maximised in the numerator (maximum likelihood estimator, MLE) for a given  $\mu$  and (pseudo) data at  $\hat{\theta}_\mu$ , while  $\hat{\mu}$  combined with  $\hat{\theta}$  defines the point for which the likelihood reaches its global maximum. The estimated signal strength modifier  $\hat{\mu}$  can not become negative since a signal rate is positive defined by physics. Furthermore, an upper constraint on the MLE  $\hat{\mu} \leq \mu$  is imposed.

The signal is excluded at  $1 - \alpha$  confidence level when

$$\text{CLs} = \frac{P(q_\mu \geq q_\mu^{\text{obs}} | \mu s + b)}{P(q_\mu \geq q_\mu^{\text{obs}} | b)} \leq \alpha, \quad (3.10)$$

with  $P(q_\mu \geq q_\mu^{\text{obs}} | \mu s + b)$  the probability to observe a value of the test statistic at least as large as the one observed in data  $q_\mu^{\text{obs}}$ , under the signal plus background ( $s + b$ ) hypothesis, and  $P(q_\mu \geq q_\mu^{\text{obs}} | b)$  for the background only ( $b$ ) hypothesis. These probabilities are defined as

$$p_\mu = P(q_\mu \geq q_\mu^{\text{obs}} | \mu s + b) = \int_{q_\mu^{\text{obs}}}^{\infty} f(q_\mu | \mu, \hat{\theta}_\mu^{\text{obs}}) dq_\mu, \\ 1 - p_b = P(q_\mu \geq q_\mu^{\text{obs}} | b) = \int_{q_{\mu=0}^{\text{obs}}}^{\infty} f(q_\mu | \mu = 0, \hat{\theta}_{\mu=0}^{\text{obs}}) dq_\mu, \quad (3.11)$$

where  $p_\mu$  and  $p_b$  are the p-values associated to the two hypothesis, and  $f(q_\mu | \mu, \hat{\theta}_\mu^{\text{obs}})$  and  $f(q_\mu | \mu = 0, \hat{\theta}_{\mu=0}^{\text{obs}})$  are the probability density functions of the signal plus background and background only hypothesis constructed from toy Monte Carlo pseudo data. These are generated with nuisance parameters fixed to  $\hat{\theta}_{\mu=0}^{\text{obs}}$  (background only) and  $\hat{\theta}_\mu^{\text{obs}}$  (signal plus background). The 95% CL level upper limit on  $\mu$  is achieved by adjusting  $\mu$  until  $\text{CL} = 0.05$ , this is the so-called observe limit. The expected median upper limit and the  $\pm 1\sigma$  and  $\pm 2\sigma$  bands for a hypothesis is generated by a large set of pseudo data and calculate the CLs and the value of  $\mu$  at 95% CL for each of them. A cumulative probability distribution can be build by starting the integration from the side corresponding to low event yields. The median expected value, so-called expected limit at 95% CL, is where the cumulative distribution function crosses the 50% quantile. The  $\pm 1\sigma$  (68%) and  $\pm 2\sigma$  (95%) bands on the expected limit are defined by the crossings of the 16% and 84%, and 2.5% and 97.5% quantiles.

In order to significantly reduce computing time, the Asymptotic CL method is used. This method avoids an ensemble of toy Monte Carlo samples and instead replaces it by one representative dataset, called Asimov dataset. This dataset is constructed such that all observed quantities are set equal to their MLE values ( $\hat{\theta}_{\text{Asimov}} = \theta_0$ ). More information about this procedure can be found in Refs. [147].



# Event reconstruction and identification

4

---

943 The simulated data after the detector simulation described in [Section 3.2](#), has the exact same  
944 format as the real collision data recorded at the CMS experiment. Therefore the same software  
945 can be used for the reconstruction of both simulation and real data. In [Section 4.1](#), the object  
946 reconstruction is explained. After reconstructing the objects, they are connected to physics  
947 objects need to be identified ([Section 4.2](#)) and corrected for pileup ([Section 4.3](#)). The objects  
948 used for physics analysis have extra requirements as shown in [Section 4.4](#). A summary of all  
949 the corrections applied to data and simulation is given in [Section 4.5](#).

## 950 4.1 Object Reconstruction

951 In [Figure 4.1](#), the particle interaction in a transverse slice of the CMS detector is shown. When  
952 a particle enters the detector, it first enters the tracker where charged particle trajectories,  
953 so-called tracks, and origins, so-called vertices, are reconstructed from signals or hits in the  
954 sensitive layers. The magnetic field bends the charged particles making it able to measure the  
955 electric charges and momenta of charged particles. The electron and photons are absorbed in  
956 the ECAL and the corresponding electromagnetic showers are detected as clusters of energy  
957 in adjacent cells. From this, the energy and the direction of the particles can be determined.  
958 The charged and neutral hadrons can also initiate a hadronic shower in the ECAL that is fully  
959 absorbed in the HCAL. The clusters from these showers are also used to estimate the energy  
960 and direction. Muons and neutrino's pass through the calorimeters without little to no energy  
961 loss and the neutrinos even escape the CMS detector undetected while muons produce hits in  
962 the muon detectors.

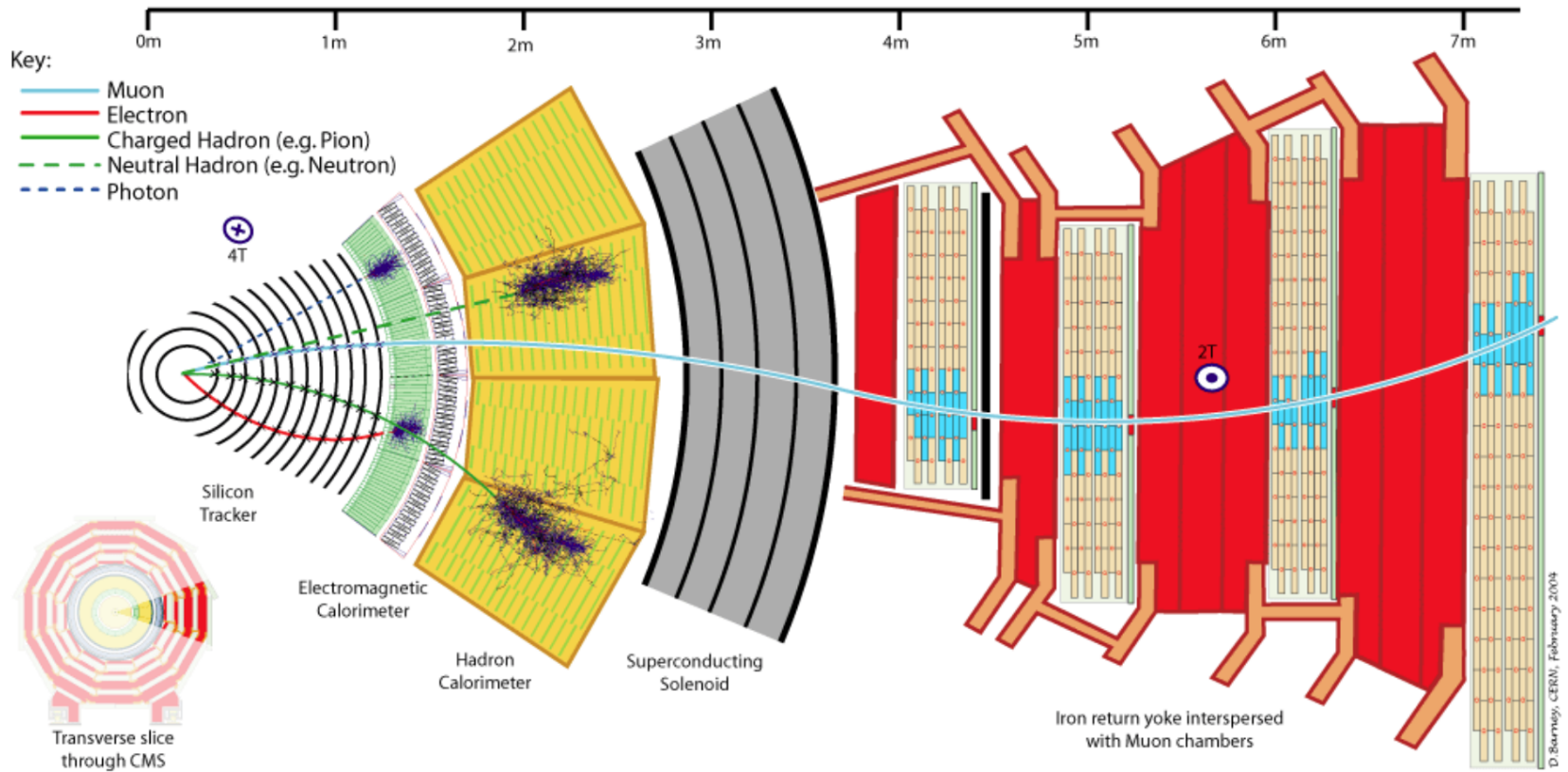


**Figure 4.1:** Cross-section of the CMS detector with all parts of the detector labelled. This sketch shows the specific particle interactions from a beam interaction point to the muon detector. The muon and charged pion are positively charged, the electron is negatively charged. Figure taken from [155].

963 The particle flow (PF) [155] reconstruction algorithm correlates the tracks and clusters  
 964 from all detector layers with the identification of each final state particle, and combines the  
 965 corresponding measurements to reconstruct the properties. The muon is identified by a track  
 966 in the inner tracker connected to a track in the muon detector as described in Section 4.1.2.  
 967 The electrons are identified by a track and an ECAL cluster, not connected to an HCAL cluster  
 968 as described in Section 4.1.3. The ECAL and HCAL clusters without a track link identify the  
 969 photons and neutral hadrons, while the addition of the tracker determines the energy and  
 970 direction of a charged hadron.

### 971 4.1.1 Charged particle tracks

972 An iterative tracking algorithm is responsible for the reconstruction of the tracks made by  
 973 charged particles in the inner tracking system. Each iteration consists of four steps [71]: the  
 974 track-seed generation, the pattern recognition algorithm, removal of track-hit ambiguities and  
 975 a final track fit. The pattern recognitions done by use a Kalman filter method [156, 157] which  
 976 into account the magnetic field and multiple scattering effects. All hits that are unambiguously  
 977 associated to the final track are removed from the list of available hits. In order to associate the  
 978 remaining hits, the procedure is repeated with looser track reconstruction criteria. The use of  
 979 the iterative track reconstruction procedure has a high track finding efficiency, where the fake  
 980 track reconstruction rate is negligible.

**NOTE:** Ik kan hier stoppen en 4.1.1, 4.1.2, 4.1.3.4.1.4 volledig schrappen (dus enkel primary vertex houden)

### 981 4.1.2 Following the Muon's Footsteps

982 The muon reconstruction [158] has three subdivisions: local reconstruction, regional reconstruction  
 983 and global reconstruction. The local reconstruction is performed on individual detector  
 984 elements such as strip and pixel hits in the inner tracking system, and muon hits and/or segments  
 985 in the muon chambers. Independent tracks are reconstructed in the inner tracker - called tracker  
 986 tracks - and in the muon system, called standalone muon tracks. Based on these tracks, two  
 987 reconstructions are considered: Global Muon reconstruction and Tracker Muon reconstruction.  
 988 The first is an outside in approach starting from a standalone muon track while the second uses  
 989 an inside-out approach starting from tracker tracks. For low transverse momenta ( $p_T \lesssim 5$  GeV),  
 990 the tracker muon reconstruction is more efficient than the global muon approach. This is due  
 991 to the fact that tracker muons only require a single muon segment in muon system, while the  
 992 global muon approach requires typically segments in at least two muon stations. These tracker  
 993 muons are used for identifying muons from the hadronisation of b or c quarks. The global muon  
 994 approach typically improves the tracker reconstruction for  $p_T \gtrsim 200$  GeV.

### 995 4.1.3 The path of the Electron

996 Standard tracking algorithms are based on Kalman filtering which assume that the energy loss  
 997 is Gaussian distributed. Since the electron tracks are increasingly curved in the magnetic field  
 998 as a function of its flight distance, these standard tracking algorithms are not suitable to fit the  
 999 electron tracks and different filtering algorithm, the Gaussian sum filter (GSF) [159] is used  
 1000 instead.

1001 In CMS, the electrons are reconstructed in two ways. The older ECAL based tracking is  
 1002 developed to identify high energetic isolated electrons. This tracking algorithm starts from

1003 ECAL clusters with a transverse energy above 4 GeV and extrapolates from these cluster the  
 1004 position of the hits in the tracker. Another, tracker based algorithm uses all the tracks with  
 1005 a  $p_T$  higher than 2 GeV found with iterative tracking as seeds. The electron seeds from the  
 1006 ECAL- and tracker-based procedures are merged into a unique collection and are then refitted  
 1007 by using the summed Gaussian distributions as uncertainty per hit in the track fit. The electron  
 1008 efficiency is measured in 8 TeV proton collision data to be better than 93% for electrons with an  
 1009 ECAL supercluster energy of  $E_T > 20$  GeV [160]. For electrons with an  $E_T > 25$  GeV in 13 TeV  
 1010 proton collision data, the efficiency is about 96%[161].

#### 1011 4.1.4 Primary Vertex Reconstruction

1012 The primary vertex (PV) reconstruction is able to measure the location of all proton interaction  
 1013 vertices in each event consisting of the signal vertex and all vertices from pileup events. First  
 1014 tracks are selected to be consistent with being produced promptly in the primary interaction [81].  
 1015 Then the tracks are grouped according to the  $z$  coordinate of their closest approach to the beam  
 1016 line [162] and a vertex fitting algorithm [163] is performed. The primary vertex is found as the  
 1017 vertex corresponding to the highest sum of squared track transverse momenta and is taken to  
 1018 be the main interaction point. The resolution on the primary vertex is about 14  $\mu\text{m}$  in  $r\phi$  and  
 1019 about 19  $\mu\text{m}$  in the  $z$  direction for primary vertices with the sum of the track  $p_T > 100$  GeV  
 1020 for 2016 data taking.

#### 1021 4.1.5 Calorimeter clusters

1022 The energy and direction of stable neutral particles such as photons and neutral hadron are recon-  
 1023 structed using a cluster algorithm. This algorithm also separates neutral particles from charged  
 1024 hadron energy deposits, and reconstructs and identifies electrons and their bremsstrahlung  
 1025 photons. Furthermore, the cluster algorithm is contributing to the energy measurements of  
 1026 charged hadrons that don't have accurate tracks parameters, e.g. for low quality and high  
 1027 transverse momentum tracks. The clustering is performed separately in each subdetector:  
 1028 ECAL barrel and endcaps, HCAL barrel and endcaps, and the two preshower layers. The HF has  
 1029 no clustering algorithm since the electromagnetic or hadronic components give rise to an HF  
 1030 EM or HF HAD cluster.

1031 The clustering algorithm consist of different steps. First seeds are identified when cells have  
 1032 an energy larger than the seeding threshold and larger than their neighbouring cells. Then  
 1033 topological clusters are made by accumulating cells that share at least a corner with a cell  
 1034 already in the cluster and an energy above a cell threshold set to twice the noise level. The  
 1035 third step is an expectation maximization algorithm that reconstructs the cluster [155] and  
 1036 assumes that the energy deposits are Gaussian distributed. The calorimeter clusters are used  
 1037 for reconstructing photons and neutral hadrons. The clusters that are not in the vicinity of the  
 1038 extrapolated charged tracks identified as neutral hadrons or photons. If the energy deposits are  
 1039 in vicinity of charged tracks, such is the case for charged hadrons, the neutral particle energy  
 1040 deposit is measured as an excess over the charged particle deposit.

## 1041 4.2 Particle flow identification

1042 The several PF elements from the various CMS subdetectors are connected through a link  
 1043 algorithm. This algorithm tests any pair of elements in an event, only considering nearest  
 1044 neighbours in the  $\eta\phi$ -plane. The quality of the link is determined via the distance between the  
 1045 two elements and PF blocks of elements are formed from elements with a direct link or indirect  
 1046 link through common elements. The identification and reconstruction follows a particular order  
 1047 in each PF block. After each identification and reconstruction the corresponding PF elements  
 1048 (tracks and clusters) are removed from the PF block.

1049 The muons are the first to be identified and reconstructed. These are reconstructed if their  
 1050 momenta are compatible with corresponding track only momenta. Then the electron and its  
 1051 corresponding brehmstrahung photons, are identified and reconstructed by using of the GSF  
 1052 tracking. At the same time, the energetic and isolated photons are identified as well. The  
 1053 remaining elements in the PF block are subjected to a cross identification of charged hadrons,  
 1054 neutral hadrons, and photons that arise from parton fragmentation, hadronisation, and decays  
 1055 in jets. The charged hadron candidate is made from the remaining candidates that have a  
 1056 charged particle track associated with them. Then the charged particle energy fraction is  
 1057 subtracted from the calibrated energy of the linked calorimeter clusters and the remaining  
 1058 energy is assigned to the neutral energy. Depending on the excess of neutral energy in the ECAL  
 1059 and HCAL clusters, a photon or a neutral hadron is assigned respectively. The pseudorapidity  
 1060 range of the inner tracker limits the information on the particles charge to  $|\eta| < 2.4$ . Outside  
 1061 this range a simplified identification is done for hadronic and electromagnetic candidates only.

## 1062 4.3 Pileup mitigation and luminosity measurement

For the 8 TeV dataset, an average of about 21 pileup interactions happen per bunch cross section. For the dataset taken at 13 TeV, the number of pileup interactions increases to about 27 interactions per bunch crossing. These interactions are spread around the beam axis around the centre of the CMS coordinate system and follow a normal distribution with a standard deviation of about 5 cm [155]. The number of pileup interactions is estimated from the number of interaction vertices reconstructed from charged particle tracks, or from the instantaneous luminosity of the given bunch crossing with dedicated detectors and the inelastic proton-proton crossing. The luminosity of the CMS interaction point is estimated from measuring certain process rates with luminometers such as the pixel detector, HF calorimeter, and the pixel luminosity telescope [164]. The instantaneous luminosity from recorded process rate  $R$  is then determined as

$$Ldt = \frac{Rdt}{\sigma_{fid}}, \quad (4.1)$$

1063 where  $\sigma_{fid} = \sigma \times A$  corresponds to the fiducial cross section recorded in the luminometer  
 1064 acceptance  $A$  which is determined using van der Meer scans [165]. The overall uncertainty on  
 1065 the luminosity measurement is estimated to be 2.5%.

1066 The luminosity is used to infer to number of pileup interactions in data, which can be used  
 1067 to corrected the predefined pileup interactions in simulation. Then an event weight can be

1068 derived from the ratio of the distributions of pileup interactions in data and simulation. For 13  
 1069 TeV collisions, the inelastic cross section is measured to be  $71.3 \pm 3.5$  mb [166]. However a  
 1070 better agreement in data and simulation for the pileup sensitive variables, such as the number  
 1071 of primary vertices, is found with a lower cross section of 69.2 mb with an uncertainty of 4.6%.

## 1072 4.4 Physics object reconstruction and identification

1073 The particle flow objects are used for building physics objects that are used for analysis. Analyses  
 1074 use jets, muons, electrons, photons, taus and missing transverse momentum  $\vec{p}_T$  with extra,  
 1075 analysis dependent requirements. In the following section, only the physics objects used  
 1076 throughout this thesis are discussed.

### 1077 4.4.1 Muons

1078 The muon candidates used for analysis in this thesis correspond to the tight and loose working  
 1079 point. Detailed reports on the performance can be found in [167].

1080 The tight working point rejects objects wrongly reconstructed as muons from hadron showers  
 1081 that reach the muon system (punch-throughs), by requiring that the global muon fit includes  
 1082 at least one valid hit in the muon chambers for which at least two muon segments in two  
 1083 muon stations are present. Furthermore, the muon tracks should have a global fit yielding a  
 1084 goodness-of-fit of  $\chi^2/\text{ndof} < 10$ . Requiring at least one pixel hit in the muon track suppresses  
 1085 the decay of muons in flight. Also a minimum of five hits in the tracker is required. Cosmic  
 1086 muons and muons originating from pileup interactions are rejected by constricting the distance  
 1087 of the muon with respect to the primary vertex by putting limits on  $d_{x,y} < 2$  mm and  $d_z < 5$   
 1088 mm. Also muons according to the loose muon working point will be used in the thesis. These  
 1089 are either global muons or tracker muons reconstructed from the particle flow muon object. In  
 1090 Table 4.1, the muon requirements for the muons used throughout this thesis are summarised.  
 1091 In Figure 4.2, the muon efficiencies for data and simulation is presented. These efficiencies are  
 1092 estimated from tag-and-probe methods [167]. Overall, the efficiency is about 95-100%, with  
 1093 two drops due to the crack between the wheels of the DT system. The differences between  
 1094 data and simulation are corrected by applying  $p_T$ - and  $\eta$ -dependent scale factors ( $\epsilon_{\text{data}}/\epsilon_{\text{MC}}$ )  
 1095 to simulated events.

In addition to the identification criteria, the muons are required to be spatially isolated from electromagnetic and hadronic activity. The relative lepton isolation is defined as estimating the total transverse energy of the particles emitted around the direction of the lepton by defining a cone of radius  $\Delta R$  in  $\eta\phi$  plane around the lepton direction. Then a summed energy is calculated from the charged hadrons (CH), neutral hadrons (NH), photons ( $\gamma$ ), excluding the lepton itself. This sum is then corrected to remove the energy coming from pileup interactions. The relative isolation for muons  $\mathcal{I}_\mu$  is defined as [155]:

$$\mathcal{I}_\mu = \frac{\sum p_T(\text{CH}) + \max(0., \sum E_T(\text{NH}), \sum E_T(\gamma) - 0.5 \times \sum E_T(\text{CH}))}{p_T(\mu)}, \quad (4.2)$$

1096 where a cone of  $\Delta R = 0.4$  is adopted and the pileup mitigation is based on the  $\Delta\beta$  correction.  
 1097 The  $\Delta\beta$  correction estimates the pileup energy as half of the contribution coming from charged

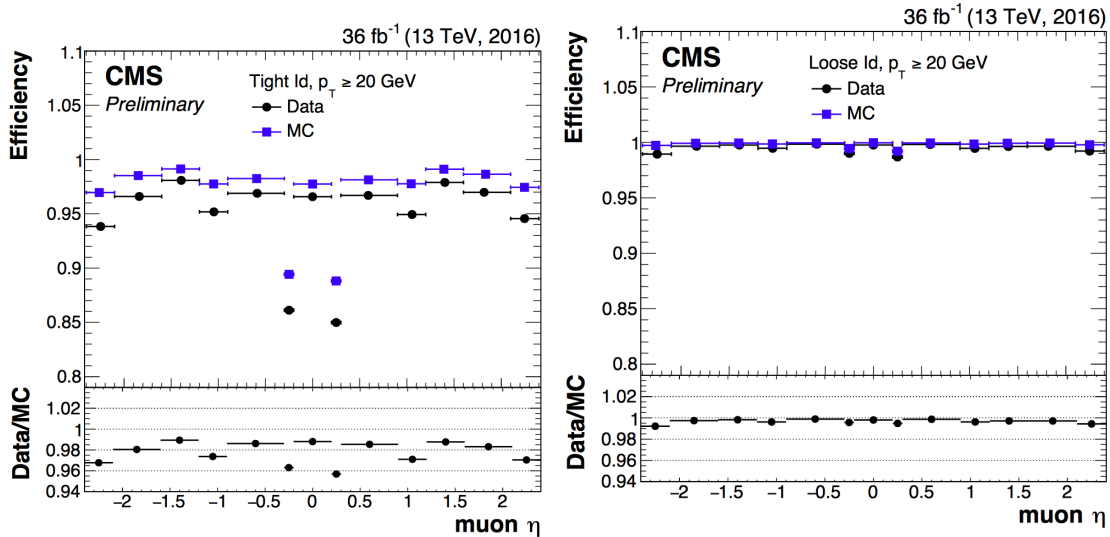


**Figure 4.2:** Comparison of the muon tight ID (left) and loose ID (right) efficiencies in data and simulation as a function of the pseudorapidity of the muon using the full 2016 dataset. Figure taken from [167].

hadrons. For tight ID muons, this relative isolation should  $\mathcal{I}_\mu < 0.15$ , while for loose muons this should be  $\mathcal{I}_\mu < 0.25$ . In Figure 4.3, the isolation efficiencies as a function of the pseudo rapidities using the tag and probe method are shown for the tight muon working point. The efficiencies are 85-100% and have a decline for low- $p_T$  muons. The differences between data and simulation are accounted for by applying  $\eta$ - and  $p_T$ -dependent scale factors on the simulation.

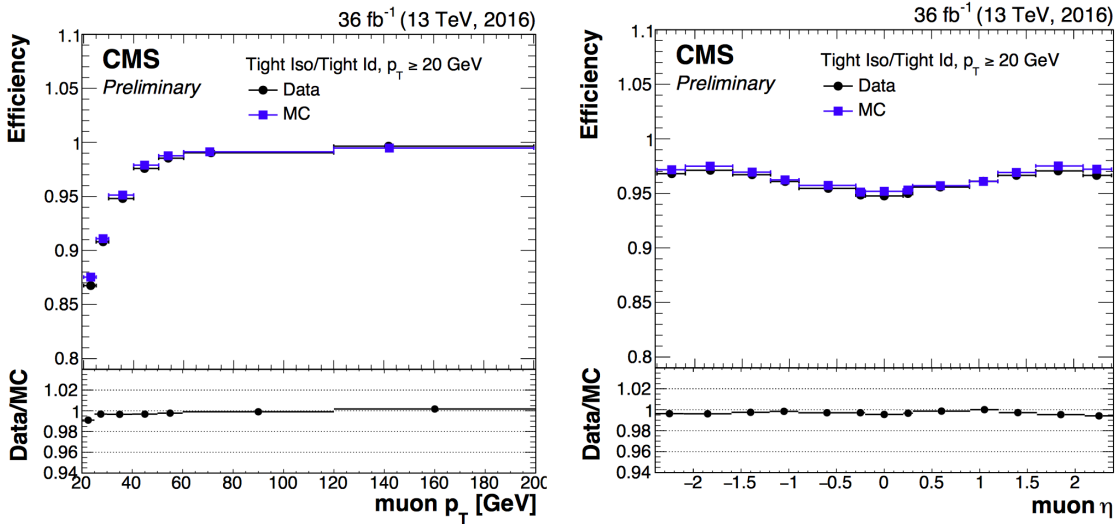


**Figure 4.3:** Comparison of the muon tight isolation requirement with the muon tight ID efficiencies in data and simulation as a function of the transverse momentum (left) or pseudorapidity (right) of the muon using the full 2016 dataset. Figure taken from [167].

**Table 4.1:** Muon requirements for the tight and loose working points, used throughout this thesis.

Property	Loose Muons	Tight Muons
Global muon or Tracker Muon	One or the other	Both
Particle Flow muon	Y	Y
$\chi^2/ndof$ of global muon track fit	N/A	< 10
Nb. of hit muon chambers	N/A	> 0
Nb. of muon stations contained in the segment	N/A	> 1
Size of the transverse impact parameter of the track wrt. to the PV	N/A	$d_{xy} < 2 \text{ mm}$
Longitudinal distance wrt. the PV	N/A	$d_z < 5 \text{ mm}$
Nb. of pixel hits	N/A	> 0
Nb. of tracker layers with hits	N/A	> 5
Relative Isolation	<0.25	<0.15

#### 1103 4.4.2 Electrons

1104 The electrons candidates used correspond to the tight and veto working points. The study of  
 1105 the electron reconstruction and identification performance can be found in [161].

1106 Starting from an electron PF candidate with a GSF track that is outside the barrel-endcap  
 1107 transition region ( $1.4443 < |\eta| < 1.5660$ ), several requirements are set. The electron track  
 1108 should not have more than one (two or three) missing hit in the innermost layer for the tight (veto)  
 1109 working point. This dismisses electrons from photon conversions are dismissed. Additionally, a  
 1110 photon conversion veto is applied by testing if a pair of electron tracks is originating from a  
 1111 common displaced vertex. Furthermore, refined cuts are applied on the shower shape variables  
 1112 such as the difference in  $\eta$  or  $\phi$  between the energy weighted supercluster position in the  
 1113 ECAL and the track direction in at the innermost tracker position ( $\Delta\eta_{\text{in}}$ ,  $\Delta\phi_{\text{in}}$ ), and the ECAL  
 1114 crystal based shower covariance in the  $\eta$  direction ( $\sigma_{\eta\eta}$ ). These cuts also include energy related  
 1115 variables such as the absolute difference between the inverse electron energy measured in the  
 1116 ECAL and the inverse momentum measured in the tracker ( $|1/E - 1/p|$ ), and the ratio of the  
 1117 energy measured in the HCAL and ECAL (H/E). Unlike the muon case, the identification criteria  
 1118 also contain requirements on the isolation of the electrons.

Similar to the muons, the electron relative isolation is determined from the sum of the particles in a cone around the electron itself. The cone radius used for electrons is  $\Delta R = 0.3$  and a  $\rho$  correction for pileup mitigation is applied. For this correction, the expected pileup energy inside the isolation cone is estimated from the median density energy per area of pileup contamination ( $\rho$ ), computed event by event, and the effective area ( $A_{\text{eff.}}$ ) [155]. This effective area is estimated from simulation and denotes the expected amount of neutral energy from

pileup interactions per  $\rho$  within the isolation cone as a function of the pseudo rapidity of the associated ECAL superclusters. Table 4.2 shows the values used for 13 TeV data. The relative electron isolation  $\mathcal{I}_e$  is calculated as

$$\mathcal{I}_e = \frac{\sum p_T(\text{CH}) + \max(0., \sum E_T(\text{NH}), \sum E_T(\gamma) - \rho \times A_{\text{eff}})}{p_T(e)}. \quad (4.3)$$

**Table 4.2:** The effective areas  $A_{\text{eff}}$  used for the electron relative isolation [168].

$\eta$ region	$A_{\text{eff}}$
$0 <  \eta  < 0.1752$	0.1703
$1.0 <  \eta  < 0.1479$	0.1715
$1.479 <  \eta  < 2.0$	0.1213
$2.0 <  \eta  < 2.2$	0.1230
$2.2 <  \eta  < 2.3$	0.1635
$2.3 <  \eta  < 2.4$	0.1937
$2.4 <  \eta  < 2.5$	0.2393

1119

1120 The efficiency of electron identification is estimated from  $Z \rightarrow e^- e^+$  events via the tag-and-  
 1121 probe method and is shown in Figure 4.4 for the tight working point. The efficiencies reach  
 1122 95 – 100%. The difference between data and simulation are corrected by dedicated  $p_T$ - and  $\eta$   
 1123 dependent scale factors as well.

#### 1124 4.4.3 Jets

1125 Jets are reconstructed from all reconstructed particles without the charged hadrons associated to  
 1126 pileup vertices. The clustering is done via the anti –  $k_T$  algorithm [169] with a radius parameter  
 1127 for the cone size of the resulting jet of  $R = 0.4$ . More information about the jet algorithm  
 1128 performance can be found in Ref. [170].

1129 The jets used for the analysis discussed in this thesis uses the loose identification working  
 1130 point summarised in Table 4.4. The requirements on the jet constituents are based on the  
 1131 assumption that a proper jet originating from the hadronisation of a quark or gluon consists of  
 1132 multiple PF particles and types. Therefore, the jet should consist of more than one constituent  
 1133 and the neutral hadron fraction and neutral EM energy fractions should be less than 99%. For  
 1134 the jets within the tracker acceptance ( $|\eta| < 2.4$ ), at least one constituent has to be a charged  
 1135 hadron resulting in a charged hadron energy fraction above 0%. Additionally the charged  
 1136 EM energy fraction should be less than 99%. On top of these requirements, objects that are  
 1137 labelled as jets and found in vicinity of any isolated lepton,  $\Delta R < 0.3$ , are removed from the jet  
 1138 collection in that event to avoid duplications of objects.

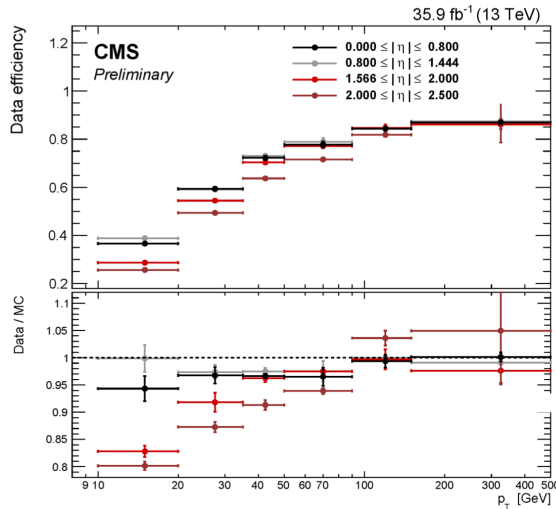


**Figure 4.4:** Electron identification efficiency as function of the electron transverse momentum from the full 2016 dataset. Figure taken from [161].

**Table 4.3:** Electron requirements used in this analysis. The requirements are set in the barrel ( $|\eta_{supercluster}| \leq 1.479$ ) and the endcaps ( $|\eta_{supercluster}| > 1.479$ ).

Properties	$ \eta_{supercluster}  \leq 1.479$		$ \eta_{supercluster}  > 1.479$	
	Veto electron	Tight electron	Veto electron	Tight electron
$\sigma_{\eta\eta}$	< 0.0115	< 0.00998	< 0.037	< 0.0292
$ \Delta\eta_{in} $	< 0.00749	< 0.00308	< 0.00895	< 0.00605
$ \Delta\phi_{in} $	< 0.228	< 0.0816	< 0.213	< 0.0394
H/E	< 0.356	< 0.0414	< 0.211	< 0.0641
relative isolation	< 0.175	< 0.0588	< 0.159	< 0.0571
$ 1/E - 1/p $	$< 0.299 \text{ GeV}^{-1}$	$< 0.0129 \text{ GeV}^{-1}$	$< 0.15 \text{ GeV}^{-1}$	$< 0.0129 \text{ GeV}^{-1}$
expected missing inner hits	$\leq 2$	$\leq 1$	$\leq 3$	$\leq 1$
pass conversion veto	Y	Y	Y	Y

**Table 4.4:** Jet criteria used throughout the thesis. The last three requirements are only for jets within the tracker acceptance.

Properties	Loose Jet ID
Neutral hadron fraction	< 0.99
Neutral EM fraction	< 0.99
Number of constituents	> 1
Charged hadron fraction	> 0
Charged multiplicity	> 0
Charged EM fraction	< 0.99

1139 The energy of the reconstructed jets deviates from the energies of the corresponding jets  
 1140 clustered from the hadronisation products of true partons from simulations due to non linear  
 1141 subdetector response and efficiencies. The jet energy corrections (JEC) calibrate the jets  
 1142 in order to have the correct energy scale and resolution. Jet energy scale corrections (JES)  
 1143 are determined as a function of pseudorapidity and the transverse momentum from data and  
 1144 simulated events by combining several channels and methods. This is extensively described  
 1145 in [171]. These corrections account for the effects of pileup, the uniformity of the detector  
 1146 response, and residual data-simulation jet energy scale differences. Furthermore, the jet energy  
 1147 resolution (JER) is measured in data and simulation as function of pileup, jet size and jet flavour.  
 1148 The performance of the jet energy corrections for the 13 TeV dataset can be found in [172].

1149 The JEC are factorised and subsequently correct for the offset energy due to pileup, the detector  
 1150 response to hadrons, and residual differences between data and simulation as a function of the  
 1151 jet pseudorapidity and transverse momentum. The consecutive steps of JEC are shown in Figure  
 4.5. The off set corrections remove the dependence of the jet energy response of additional pileup

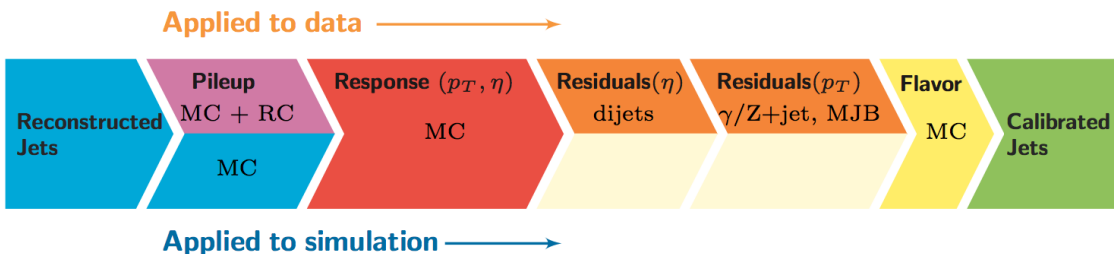


**Figure 4.5:** The sequence of the JEC for data and simulations. The corrections marked with MC are derived from simulation studies, while RC stands for random cone, and MJB for the analysis of multi-jet events. Figure taken from [171].

1152 activity. It is based on the jet area method, which uses the effective area of the jets multiplied  
 1153 by the average density in the event to calculate the offset energy to be subtracted of the  
 1154 jets. The correction factors are derived by comparing the jet response with and without pileup

1156 events overlaid. The residual differences between data and detector simulation are determined  
 1157 using the random cone method (RC). For this method, many jets are reconstructed in each  
 1158 event by clustering particles through placing random cones. This provides a mapping of the  
 1159  $\eta\phi$ -space and the average  $p_T$  of those jets gives the average energy offset due to pileup [171].  
 1160 The next level of corrections have as goal to have an uniform energy response independent  
 1161 of the transverse momentum or pseudorapidity of the jet. These corrections are determined  
 1162 from simulated events by matching the reconstructed to true particle jets and comparing there  
 1163 momenta. The residual corrections between data and simulation are determined by comparing  
 1164 the transverse momentum balance in various types of events (multi-jet, Z + jets, and  $\gamma$  + jets),  
 1165 using a reference jet in the barrel region. The jet flavour corrections are optional and not used  
 1166 for this thesis. More information on the jet flavour corrections can be found in [171]. For jets  
 1167 with a transverse momentum above 30 GeV, the uncertainties from the various corrections are  
 1168 3-5% for the 13 TeV dataset [172].

After applying JEC, the transverse momentum resolution of the jet is extracted from data and simulated events. There are two methods used to rescale the reconstructed four momentum chosen based on whether or not the simulated jet can be matched to a true jet in simulation. The factors are defined as

$$c_{\text{matched}} = 1 + \frac{p_T^{\text{reco.}} - p_T^{\text{true}}}{p_T^{\text{reco.}}} (s_{\text{JER}} - 1), \\ c_{\text{unmatched}} = 1 + N(0, \sigma_{\text{JER}}) \sqrt{\max(s_{\text{JER}}^2 - 1, 0)}, \quad (4.4)$$

1169 where  $N(0, \sigma_{\text{JER}})$  denotes a sample value from a normal distribution centred at zero with  
 1170 as standard deviation the relative resolution in simulation  $\sigma_{\text{JER}}$ , and  $s_{\text{JER}}$  the  $\eta$ -dependent  
 1171 resolution scale factors. These scale factors are derived from data from di-jet or  $\gamma$  + jets events  
 1172 and analysing the  $p_T$  balance. The resolution scale factors (data/simulation) are found to be  
 1173 1.1-1.2 except for the transition regions around  $|\eta| = 3$  and  $|\eta| = 1.4$  [172] and given in Table  
 1174 4.5.

#### 1175 4.4.4 Jets from b fragmentation

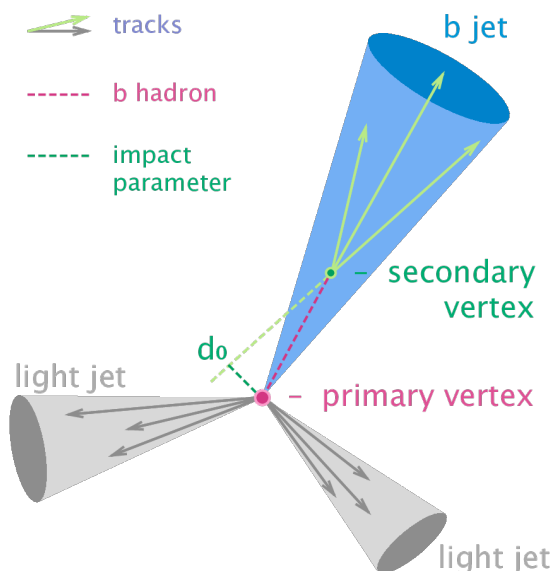
1176 Jets originating from the hadronisation of bottom quarks can be discriminated from jets from  
 1177 gluons and light-flavour quarks as well as charm quark fragmentation through the use of b-  
 1178 tagging. There are several algorithms developed within CMS to perform b-tagging [173, 174]  
 1179 on jets that fall within the pseudorapidity acceptance of the trackers. These algorithms exploit  
 1180 the properties of the b quark to identify the jets formed by its fragmentation. These hadrons  
 1181 have relative large masses, long lifetimes and daughter particles with hard momentum spectra.  
 1182 Additionally, their semi-leptonic decays can be exploited as well. To use b-jet identification  
 1183 in an analysis, one needs to know its efficiency and misidentification probability. In general  
 1184 these are function of the pseudorapidity and transverse momentum of the considered jet. Their  
 1185 performances are directly measured from data by use of b-jet enriched jet samples (multi-jet or  
 1186 top-quark decays).

1187 This thesis uses b-jets identified by the Combined Secondary Vertex version 2 (CSVv2)  
 1188 algorithm [173]. This algorithm combines secondary vertices together with track based lifetime

**Table 4.5:** Jet energy scale factors in bins of  $\eta$  with uncertainty

$ \eta $	SF	Uncertainty ( $\pm$ )
0-0.5	1.109	0.008
0.5-0.8	1.138	0.013
0.8-1.1	1.114	0.013
1.1-1.3	1.123	0.024
1.3-1.7	1.084	0.011
1.7-1.9	1.082	0.035
1.9-2.1	1.140	0.047
2.1-2.3	1.067	0.053
2.3-2.5	1.177	0.041

information by use of a multivariate technique. The secondary vertex is reconstructed from displaced tracks within a jet, as illustrated in [Figure 4.6](#). The final state b quark is encapsulated in a B meson (e.g.  $B^\pm$ ,  $B_0$ ,  $B_S$ ) after the hadronisation. This B meson has relatively long lifetime and can travel a measurable distance from the primary vertex before decaying. After reconstruction, the secondary vertices are required to be in accordance with the B meson hypothesis bases on the amount of shared tracks with the primary vertex, the invariant vertex mass to reject kaon decays, and the direction of the tracks compared to the jet axis.

**Figure 4.6:** Sketch showing the common principle of the identification of b-jets. Figure taken from [175]

1196 The b-tagging algorithm performances are evaluated taking into account two cases: discrim-  
 1197 ination of b-tagged jets originating from charm quarks, and discrimination of b-tagged jets  
 1198 against jets coming from gluons or light (u, d, s) quarks. In Figure 4.7, the misidentification  
 1199 probabilities for different b-tagging algorithms within CMS are shown. Based on the misidentifi-  
 1200 cation probabilities for a certain threshold on the CSVv2 discriminator, different working points  
 1201 are defined. These are shown in Table 4.6. The analysis presented in this thesis uses the loose  
 working point which has an average efficiency of 81% and a misidentification rate of 10%.

**NOTE:** Find reason why I am not using cMVA, omdat CSVv2 op ttbar events is gemeten en cMVA op multijet?

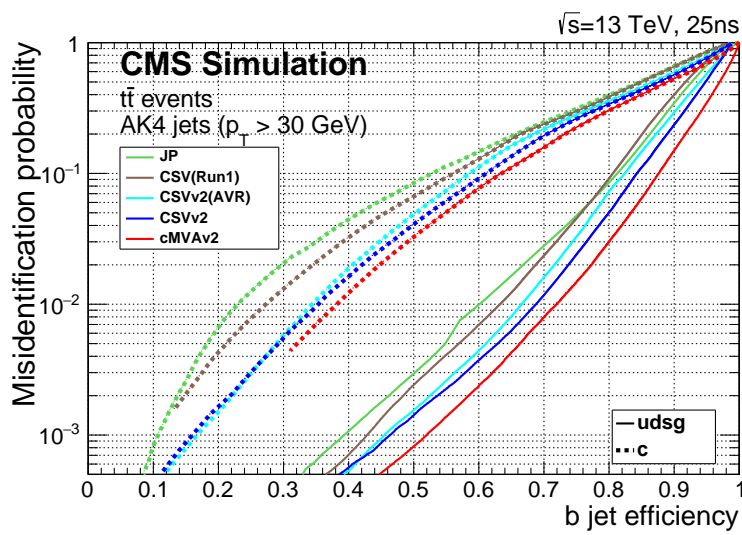


**Figure 4.7:** Misidentification probabilities of various b-tagging algorithm in simulation. Figure taken from [174].

**Table 4.6:** Working points used for tagging jets as coming from b quarks for the CSVv2 discriminant.

WP	CSVv2 discr cut	b-tag eff.	misid. prob.
Loose (L)	> 0.5426	≈ 81%	≈ 10%
Medium (M)	> 0.8484	≈ 66%	≈ 1%
Tight (T)	> 0.9535	≈ 46%	≈ 0.1%

1202

1203 The efficiency of tagging a jet as coming from a bottom quark in simulation typically deviates  
 1204 somewhat from data. Efficiency scale factors  $\epsilon_b^{\text{data}}/\epsilon_b^{\text{MC}}$  are derived from data to account for  
 1205 those differences. These scale factors are  $\eta$ -,  $p_T$ -, and flavour dependent, where the flavour  
 1206 of the jet is determined from matched generated hadrons. For cut based analyses these scale  
 1207 factors are applied to the b-tagging efficiencies and mistag rates according to the chosen working  
 1208 point [174]. For shape based analysis however, such as the one presented in this thesis, the  
 1209 scale factors are applied on the distribution of the b-tagging discriminator. This is the so-called  
 1210 IterativeFit method [176].

1211 The uncertainties related to the IterativeFit method cover possible shape discrepancies between  
 1212 data and simulation. The uncertainty coming from the purity of the sample is subdivided into  
 1213 two uncorrelated uncertainties based on the purity of the light flavoured (lf) and heavy flavoured  
 1214 (hf) jet contributions in the sample. Furthermore, the jet energy scale results in jets migrating  
 1215 from one  $p_T$  bin to an other, having an influence on bin dependent scale factors. The statistical  
 1216 fluctuations of the limited amount of entries in each bin are also accounted for and have an  
 1217 influence on the scale factor uncertainties. These have four uncorrelated sources: two for heavy  
 1218 flavour and two for light flavour jets. Since the uncertainty on the scale factors for the jets  
 1219 originating from a charm quark (cf) is determined from the uncertainty on the b scale factors  
 1220 resulting in two independent uncertainties [176].

#### 1221 4.4.5 Missing transverse energy

The missing transverse momentum  $\vec{p}_T$  and energy  $E_T^{\text{miss}}$  resulting from particles that do not interact with the detector material, are calculated by balancing the vectorial sum of the transverse momenta of all particles:

$$E_T = |\vec{p}_T|, \quad (4.5)$$

$$\vec{p}_T = - \sum_{i=1}^{N_{\text{particles}}} \vec{p}_{T,i}.$$

1222 The missing transverse energy is influenced by the minimum thresholds in calorimeters, the  
 1223 inefficiencies in the tracker, and the non-linear response of the calorimeter to hadronic particles.  
 1224 The bias is reduced by correcting the transverse momentum of the jets to particle jet  $p_T$  via the  
 1225 JEC and propagating it to the missing transverse momentum. The performance of the missing  
 1226 transverse energy reconstruction can be found in [177].

## 1227 4.5 Summary of corrections

1228 Throughout the chapter several corrections are introduced to improve the agreement between  
 1229 data and simulation. These corrections are sources of systematic uncertainties for the anal-  
 1230 ysis presented in this thesis. Therefore a summary of the corrections and their associated  
 1231 uncertainties is provided.

1232 **Lepton scale factors** The systematic uncertainty on the lepton scale factors consist of three  
 1233 sources: identification, isolation and tracking. The applied scale factors are varied  
 1234 independently within one standard deviation of their measured uncertainties to account  
 1235 for their systematic impact on the measurements.

1236 **Jet energy corrections** The momenta of the reconstructed jets are corrected to match the  
 1237 expected true energy derived from the hadronisation products of partons in simulation.  
 1238 Furthermore, residual corrections and smearing is applied to match the overall energy  
 1239 scale and resolution for simulation and data. These corrections are also propagated to  
 1240 the missing transverse energy. The systematic uncertainties due to these scale factors are  
 1241 estimated by varying them within their uncertainties and repeating the measurements  
 1242 with recalibrated jets and missing transverse energy.

1243 **CSVv2 discriminant shape reweighting** There are three sources of uncertainty contributing  
1244 to the measurement of the scale factors: statistical uncertainties, jet energy scale and  
1245 the purity of the sample. The jet energy scale uncertainty is 100% correlated to the jet  
1246 energy uncertainties and is evaluated simultaneously. The uncertainty coming from the  
1247 purity of the sample is subdivided into two uncorrelated uncertainties based on the purity  
1248 of the light flavoured (lf) and heavy flavoured (hf) jet contributions in the sample. A  
1249 one sigma shift in each of the two purity contributions corresponds to a higher/lower  
1250 contribution in the purity of the considered flavours. The statistical uncertainties has  
1251 four uncorrelated sources, two for heavy flavour and two for light flavour jets. One of  
1252 the uncertainties correspond to the shift consistent with the statistical uncertainties of  
1253 the sample, while the other is propagated in a way that the upper and lower ends of the  
1254 distribution are affected with respect to the centre of the distribution. The uncertainty  
1255 on the charm jet scale factors (cf) is obtained from the uncertainty on the heavy flavour  
1256 scale factors, doubling it in size and constructing two nuisance parameters to control the  
1257 charm flavour scale factors and treating them as independent uncertainties.

1258 **Pileup** Varying the minimum bias cross section, used to calculate the pileup distribution by  
1259  $\pm 4.6\%$ , results in a systematic shift in the pileup distribution. The uncertainty is estimated  
1260 by recalculating the pileup weights to the distributions associated to the minimum bias  
1261 cross sections.

1262 **Luminosity** The luminosity is measured with a global uncertainty of 2.5%, affecting the ex-  
1263 pected number of events.

1264

# Event selection and categorisation

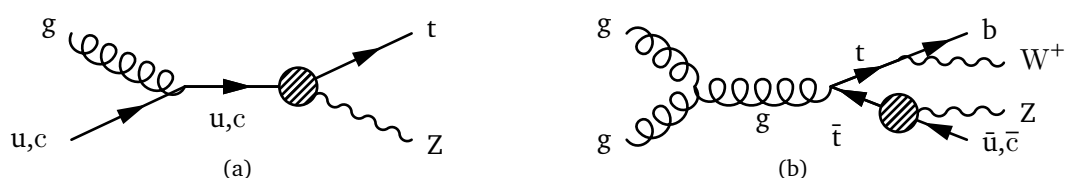
# 5

1265 A basic event selection is made for selecting signal like events. The necessary event requirement  
 1266 are discussed in [Section 5.2](#).

1267 The analysis uses signal and background regions to constrain the huge SM background  
 1268 compared to the expected signal. [Section 5.4](#) discusses each region that is entering the analysis.  
 1269 On top of the use of background estimation from control regions, backgrounds that have prompt  
 1270 leptons contaminated by real leptons either from decays of tau leptons or from hadronized  
 1271 mesons or baryons (collectively commonly referred as “non-prompt leptons”) as well as by  
 1272 hadrons or jets misidentified as leptons<sup>1</sup> are evaluated with a data-driven method discussed in  
 1273 [Section 5.3](#).

## 1274 5.1 Baseline event selection and filters

1275 The CMS collaboration recorded in the course of 2016 proton at 13 TeV collisions data with a  
 1276 total recorded integrated luminosity of  $35.9 \pm 2.5\% \text{ fb}^{-1}$ . The baseline event selection has a  
 1277 goal to substantially reject SM background events, whilst maintaining a high signal efficiency.  
 1278 In this analysis a search is performed in a final state made up of a Z boson and a top quark,  
 1279 associated or not with a jet, in the leptonic decay of the Z boson and the top quark. The leading  
 order Feynman diagrams can be seen in [Figure 5.1](#).



**NOTE:**  
adapt to  
leptonic de-  
cay

**Figure 5.1:** Feynman diagrams for the tZq FCNC interaction with a fully leptonic decay, where the FCNC interaction is indicated with the shaded dot. (a) Single top production through an FCNC interaction. (b) Top pair production with an FCNC induced decay.

1280

<sup>1</sup>These two classes of contamination will be referred to as not prompt-lepton (NPL) samples.

1281 The signal considers both the single top quark FCNC ( $tZ$  in the final state) and the top quark  
 1282 pair FCNC ( $tZq$  in the final state) events. Their final state signatures consist of three leptons,  
 1283 considering electrons or muons in our analysis, and a jet originating from a  $b$  quark. For FCNC  
 1284  $tZq$ , there is an additional up or charm jet. Leptons from tau decays are not vetoed and are  
 1285 entering the analysis. Four different lepton channels based on lepton flavour are considered  
 1286 ( $eee$ ,  $e\mu\mu$ ,  $\mu\mu\mu$ , and  $\mu\mu\mu$ ).

1287 The CMS trigger system, described in Section 2.2.3, filters out the main of the collision events  
 1288 from uninteresting processes and dedicated trigger paths are define to single out the events  
 1289 with our required detector signature. The trigger paths are chosen based on on-line triggering  
 1290 objects with at least one muon (M), at least one electron (E), at least two muons (MM), at  
 1291 least two electrons (EE), at least one muon and an electron (ME), at least three muons (MMM),  
 1292 at least three electrons (EEE), at least two muons and one electron (MME), or at least two  
 1293 electrons and one muon (EEM). For the MC simulation a simple *or* of all triggers is taken and  
 1294 the event is taken if it passes one of the trigger paths. For data however, double counting of the  
 1295 same event has to be taken into account and a procedure to avoid double counting has been  
 1296 put into place. It consists of vetoing in a given dataset the events that are already selected in  
 another, as given in Table 5.1.

**Table 5.1:** Trigger logic used to select data events in order to avoid double counting

Dataset	Trigger Logic
$e\mu$	$EM \parallel EEM \parallel MME$
$\mu\mu$	$(MM \parallel MMM) \&& !(EM \parallel EEM \parallel MME)$
$ee$	$(EE \parallel EEE) \&& !(MM \parallel MMM) \&& !(EM \parallel EEM \parallel MME)$
single $\mu$	$M \&& !(EE \parallel EEE) \&& !(MM \parallel MMM) \&& !(EM \parallel EEM \parallel MME)$
single $e$	$E \&& !M \&& !(EE \parallel EEE) \&& !(MM \parallel MMM) \&& !(EM \parallel EEM \parallel MME)$

1297

1298 This trigger selection strategy is to allow the maximum statistics on the signal region since it  
 1299 does not discard events from any dataset. For the single lepton triggers, at least one electron  
 1300 (muon) with a transverse momentum  $p_T$  higher than 32 GeV (24 GeV) is required. The dilepton  
 1301 triggers require an electron (muon) with  $p_T > 23$  GeV and a muon (electron) with  $p_T > 8$  GeV,  
 1302 or an electron (muon) with  $p_T > 23$  GeV (17 GeV) and an electron (muon) with  $p_T > 12$  GeV  
 1303 (8 GeV). Events collected by the trilepton triggers require an electron (muon) with  $p_T > 16$  GeV  
 1304 (12 GeV), a second electron (muon) of  $p_T > 12$  GeV (10 GeV), and a third electron (muon)  
 1305 with  $p_T > 8$  GeV (5 GeV). The mixed trilepton trigger events require two electrons (muons)  
 1306 with  $p_T > 12$  GeV (9 GeV) and a third muon (electron) with  $p_T > 8$  GeV (9 GeV). The HLT  
 1307 trigger paths used in data and simulation are summarised in Table 5.2.

1308 In order to ensure a full trigger efficiency, the offline  $p_T$  threshodls are set higher than the on-  
 1309 line trigger thresholds. Selected electrons (muons) are required to have  $p_T > 35$  (30) GeV and  
 1310  $|\eta| < 2.1(2.4)$ . A quantity for evaluating lepton isolation is calculated as the summed energy of

**Table 5.2:** HLT trigger paths used to select data and simulation events.

Trigger path name	Trigger type
HLT_Mu23_TrkIsoVVL_Ele8_CaloIdL_TrackIdL_IsoVL_v	ME
HLT_Mu23_TrkIsoVVL_Ele8_CaloIdL_TrackIdL_IsoVL_DZ_v	ME
HLT_Mu8_TrkIsoVVL_Ele23_CaloIdL_TrackIdL_IsoVL_v	ME
HLT_Mu8_TrkIsoVVL_Ele23_CaloIdL_TrackIdL_IsoVL_DZ_v	ME
HLT_DiMu9_Ele9_CaloIdL_TrackIdL_v	MME
HLT_Mu8_DiEle12_CaloIdL_TrackIdL_v	EEM
HLT_IsoMu24_v	M
HLT_IsoTkMu24_v	M
HLT_Ele32_eta2p1_WPTight_Gsf_v	E
HLT_Mu17_TrkIsoVVL_Mu8_TrkIsoVVL_v	MM
HLT_Mu17_TrkIsoVVL_TkMu8_TrkIsoVVL_v	MM
HLT_Mu17_TrkIsoVVL_Mu8_TrkIsoVVL_DZ_v	MM
HLT_Mu17_TrkIsoVVL_TkMu8_TrkIsoVVL_DZ_v	MM
HLT_TripleMu_12_10_5_v	MMM
HLT_Ele23_Ele12_CaloIdL_TrackIdL_IsoVL_DZ_v	EE
HLT_Ele16_Ele12_Ele8_CaloIdL_TrackIdL_v	EEE

1311 all particles (charged hadrons, neutral hadrons, photons) in a cone of radius  $\Delta R < 0.3$  (0.4)  
 1312 around the electron (muon), excluding the electron (muon) itself, and divided by the lepton  $p_T$   
 1313 . An electron candidate is selected if this isolation quantity is below 0.059 in the barrel region  
 1314 and below 0.057 in the end caps. A muon candidate is selected if this isolation quantity is  
 1315 below 0.15. Other lepton selection criteria are applied in analysis based on the values of various  
 1316 quantities determined during the reconstruction, such as number of missing track hits or the  
 1317 electromagnetic shower created by the particles. These are given in [Section 4.4.1](#) ([Table 4.1](#))  
 1318 and [Section 4.4.2](#) ([Table 4.3](#)). The trigger efficiency estimation is described in [Section 5.1.2](#).

1319 The samples are pre-selected off-line to ensure that all reconstructed particles considered  
 1320 for the analysis are corresponding to a proton interaction and that signals from beam halo  
 1321 particles as well as detector noise is removed. For this reason, several filters are used. These are  
 1322 described in [Section 5.1.1](#).

1323 On top of leptons, jets and missing transverse energy are expected from the signal signature.  
 1324 The jets are reconstructed using the anti- $k_T$  algorithm with a distance parameter of 0.4 using

1325 the particle flow particles that are not identified as isolated leptons as input. The jet momentum  
 1326 is determined as the vectorial sum of the particles contained in the jet. Additional selection  
 1327 criteria are applied to each event to remove spurious jet-like features originating from isolated  
 1328 noise patterns in certain hadron calorimeter regions. More information about the jets used for  
 1329 this analysis can be found in [Section 4.4.3](#). The jets are calibrated in simulation and in data  
 1330 separately, accounting for deposits from pileup and the non-linear detector response. Calibrated  
 1331 jets with  $p_T > 30$  GeV and  $|\eta| < 2.4$  are selected. A selected jet may still overlap with the  
 1332 selected leptons leading to a double-counting. To prevent such cases, jets that are found within  
 1333 a cone of  $R = 0.3$  around any of the signal electrons (muons) are removed from the set of  
 1334 selected jets.

1335 The jets originating from b quarks are tagged using the CSVv2 algorithm, which combines  
 1336 the information of displaced tracks with information of secondary vertices associated with the  
 1337 jet using a multivariate technique. The jets are tagged as a jet coming from a b quark (b-tagged)  
 1338 if the CSVv2 discriminator is above a certain threshold. This analysis uses a threshold that  
 1339 results in an average b-tagging efficiency of 81% and a misidentification rate of 10%. More  
 1340 information about b-tagging can be found in [Section 4.4.4](#).

1341 The missing transverse momentum vector  $\vec{p}_T$  is defined as the projection on the plane  
 1342 perpendicular to the beams of the negative vector sum of the momenta of all reconstructed  
 1343 particles in an event. Its magnitude is denoted by  $E_T^{\text{miss}}$  as shown in [Section 4.4.5](#). Its longitudinal  
 1344 component is calculated by limiting the lepton + neutrino to the W boson mass. In case two  
 1345 solutions arise, the mass closest to the known top quark mass is used. The events and their  
 1346 corresponding object collections reconstructed using the reconstruction criteria described in  
 1347 [Section 4.1](#), are used as input for the analysis. Further requirements on the momenta and the  
 1348 pseudo rapidities are made to fulfil the trigger requirements and reconstruction algorithms.

### 1349 5.1.1 Event cleaning

1350 Some events arising from instrumental noise and beam backgrounds might end up in the  
 1351 data [[177](#), [178](#)]. Spurious deposits may appear in the ECAL from non collision origins such  
 1352 as beam halo particles, or from particles striking the sensors in the ECAL photo detectors.  
 1353 Conjointly, dead ECAL cells can cause artificial missing transverse energy. The HCAL can cause  
 1354 spurious energy from particle interactions with the light guides and the photomultiplier tubes  
 1355 of the HF, as well as noisy hybrid photo diodes. In CMS, different algorithms, so-called filters,  
 1356 are developed to identify and suppress these events.

1357 The ECAL electronics noise and spurious signals from particle interactions with photo detectors  
 1358 are mostly removed via topological and timings based selection using ECAL information only.  
 1359 The remaining effects such as anomalously high energy crystals and the lack of information  
 1360 for channels due to inefficiencies in the read out are removed through dedicated events filters.  
 1361 Five ECAL endcap supercrystal have been identified for giving anomalously high energies due  
 1362 to high amplitude pulses in several channels at once, and are masked. Furthermore, the crystal  
 1363 read out from a small amount of ECAL towers is not available. However, their trigger primitive  
 1364 information is still available making it possible to estimate the magnitude of unmeasured energy  
 1365 and when the value is too large, the event is filtered out.

1366     The machine induced particles, via beam-gas / beam-pipe/... interactions, that are flying with  
 1367     the beam affect the physics analysis. They leave a calorimeter deposit along a line at constant  
 1368      $\phi$  in the calorimeter, and interactions in the CSCs will often line up with this deposit. This  
 1369     can be seen in [Figure 5.2](#). Therefore, events containing such beam halo particles are removed  
 1370     from the selection with the CSC Beam Halo Filter. This filter uses information related to the  
 1371     geometric quantities, energy deposits, and timing signatures. For 2016, the filter rejects 85% in  
 1372     a halo-enriched sample, whereas the mistag probability determined from simulation if found to  
 1373     be less than 0.01%.

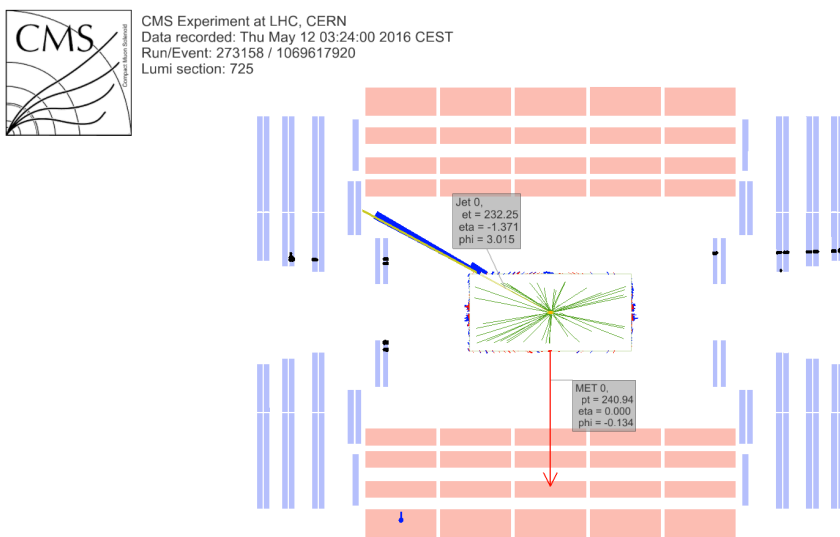


**Figure 5.2:** Event display of a beam halo event with collinear hits in the CSC (black), missing transverse energy of 250 GeV and a jet of 232 GeV. The hadronic deposit is spread in  $\eta$ , but narrow in  $\phi$ . Figure taken from [\[177\]](#).

1373

1374     Furthermore, there is anomalous high missing transverse energy coming from low quality  
 1375     muons that lead to high- $p_T$  tracks, but are considered not good by the particle flow algorithm.  
 1376     These low quality tracks will be mislabelled as charged hadrons and will therefore be used in  
 1377     the calculation of the missing transverse energy. By investigation the purity of the reconstructed  
 1378     tracks and the relative transverse momentum error of the muons, these events can be filtered  
 1379     out.

1380     Supplementary to previous filters, only events with where the first primary vertex is a well  
 1381     reconstructed primary vertex are selected. The reconstructed primary vertex should have at  
 1382     least five degrees of freedom, the longitudinal distance from the beam spot is maximally 24 cm  
 1383     ( $d_z < 24$  cm), and the transversal distance from the beam spot is maximally 2 cm ( $d_{xy} < 2$  cm).

1384 **5.1.2 Estimation of the trigger efficiency**

1385 The trigger efficiency in data is estimated using a data sample collected using unprescaled  $E_T^{\text{miss}}$   
 1386 triggers. These allow events with a missing transverse energy higher than 110 GeV(120 GeV)  
 1387 and that the scalar sum of the transverse momenta of the reconstructed PF jets  $H_T^{\text{trig.}}$  is at least  
 1388 300 GeV (120 GeV), or a calorimeter/PF  $E_T^{\text{miss}}$  higher than 200 GeV/300 GeV. For an HB-HE  
 1389 cleaned event the PF missing transverse energy threshold is lowered to 170 GeV. These trigger  
 1390 paths are summarised in [Table 5.3](#) and chosen to be completely uncorrelated with the lepton  
 triggers given in [Table 5.2](#).

**Table 5.3:** Unprescaled  $E_T^{\text{miss}}$  HLT trigger paths for estimating the trigger efficiency. An *or* of the triggers  
 is used to select events.

Trigger path	Requirement
HLT_PFHT300_PFMET110_v*	PF $E_T^{\text{miss}} > 110$ GeV, PF $H_T^{\text{trig.}} > 300$ GeV
HLT_MET200_v*	calorimeter $E_T^{\text{miss}} > 200$ GeV
HLT_PFMET300_v*	PF $E_T^{\text{miss}} > 300$ GeV
HLT_PFMET120_PFHT120_IDTight_v*	PF $E_T^{\text{miss}} > 120$ GeV, PF $H_T^{\text{trig.,tightWP}} > 120$ GeV
HLT_PFMET170_HBHECleaned_v*	PF $E_T^{\text{miss}} > 170$ GeV, cleaned for HB/HE anomalous signals

The studied simulation sample is the main background, WZ+jets, with all corrections applied. For this study, the events passing a three lepton cut and at least one jet are being used. The corresponding efficiencies are then calculated as

$$\epsilon_{data} = \frac{\text{Nb. of events passing lepton and MET triggers}}{\text{Nb. of events passing MET triggers}} \quad (5.1)$$

$$\epsilon_{MC} = \frac{\text{Nb. of events passing lepton triggers}}{\text{Nb. of total events}} \quad (5.2)$$

The resulting efficiencies and scale factors can be found in [Table 5.4](#), where the scale factors are defined as

$$SF = \frac{\epsilon_{data}}{\epsilon_{MC}}. \quad (5.3)$$

More detailed scale factors and efficiencies can be found in [Appendix A](#).

**Table 5.4:** Trigger scale factors for each channel, after three lepton + jets cut, in the Z mass window. by counting number of events.

	all	$\mu\mu\mu$	eee	$ee\mu$	$e\mu\mu$
	1.0000	1.0000	0.9541	1.0006	1.0004%

1392

1393 The trigger efficiencies are also measured in function of the  $p_T$  of the leptons for which the  
 1394 distributions can be found in [Appendix A](#). The resulting scale factors in can be found in Figure  
 1395 [Figure 5.3](#). The trigger efficiencies are measured to be nearly 100% for both simulation and  
 1396 data. The results are dominated by statistics and assigning a large uncertainty to the trigger  
 1397 efficiency based on the dataset collected by  $E_T^{\text{miss}}$  triggers would be over conservative. A one  
 1398 percent uncertainty on the trigger selection for the  $ee\mu$  and  $\mu\mu\mu$  final states, and 5% for the  
 1399  $eee$  and  $e\mu\mu$  final states is assigned instead. No scale factors will be applied on simulation as  
 1400 they are close to unity. Control plots are made in the dilepton region to validate all corrections  
 1401 applied to simulation and can be found in [Appendix B](#).

**NOTE:**  
Make sure  
this is the  
case

### 1402 5.1.3 Corrections

1403 Mismatches between data and simulation are corrected for via the use of scale frcators. These  
 1404 are elaborately discussed in [Section 4.4](#). In this section a short overview of the applied corrections  
 1405 is given and their effect on a dilepton selection is shown.

### 1406 Pile up reweighting

1407 In data, the number of interactions per bunch crossing (pile up) is calculated with a minimum  
 1408 bias cross section of 69.2 mb. The number of simulated pile up events is then reweighed to  
 1409 match the expected number of pile up events in data. Pile up reweighting manifests itself as an  
 1410 altered shape of the number of reconstructed primary vertices as can be seen in [Figure 5.4](#).

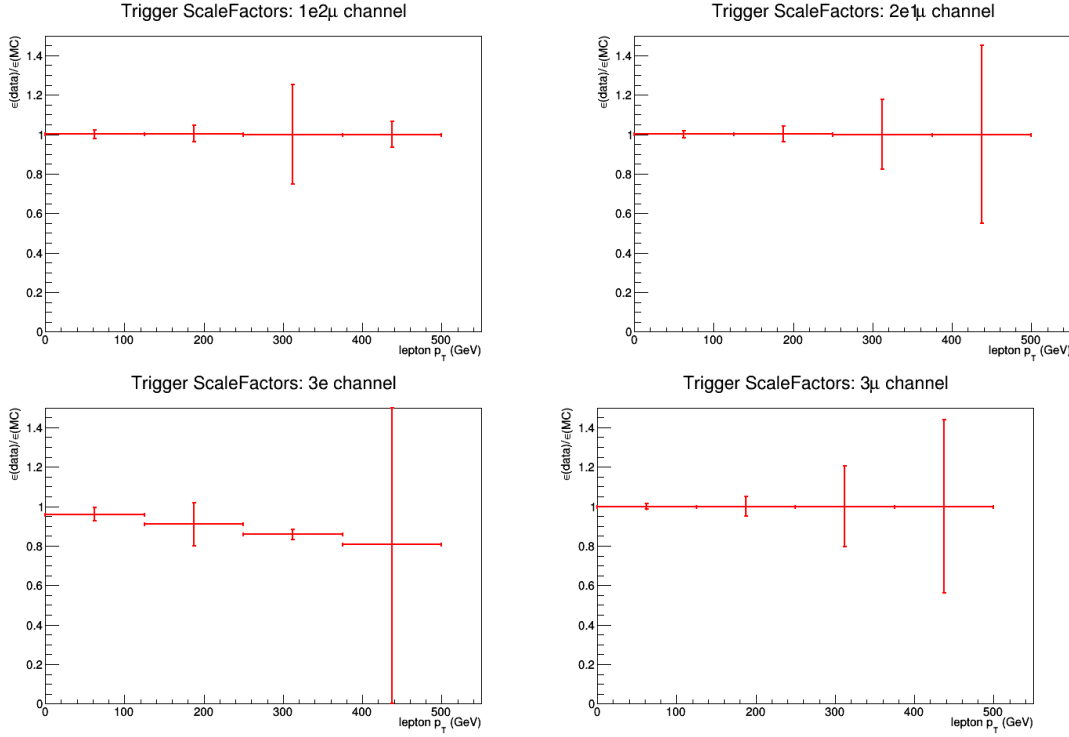


**Figure 5.3:** The trigger scale factors measured as a function of lepton  $p_T$ , using the dataset collected by  $E_T^{\text{miss}}$  triggers and WZ simulation, after a 3 lepton and jets selection, in the Z mass window. All corrections to simulation are applied. Left, upper: eeμ channel. Right, upper: eeμ channel. Left, lower: eee channel. Right, lower: μμμ channel

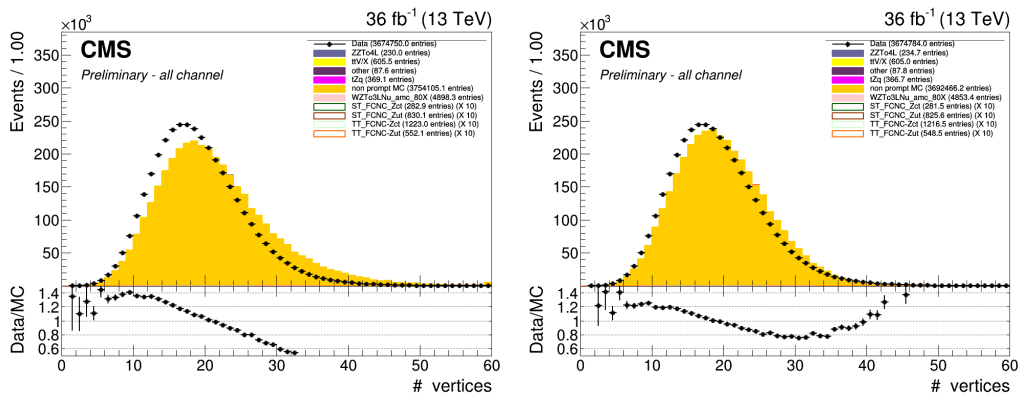


**Figure 5.4:** The number of primary vertices before (left) and after (right) pile up reweighting. After a 2 lepton plus jets selection, in the Z mass window.

1411 Note that [Figure 5.4](#) indicates that even after pile up reweighting, the primary vertex multiplicity  
 1412 is not well described by simulation. This is a known effect, and using a minimum bias  
 1413 cross section with a slightly lower value is found to better describe the data. However, the b  
 1414 tagging scale factors are only provided for the nominal inelastic cross section, and thus this  
 1415 value is used.

1416 **Lepton scale factors**

The efficiency to select leptons is different in simulation ( $\epsilon_{\text{MC}}$ ) compared to the data ( $\epsilon_{\text{data}}$ ). This is corrected for by applying lepton scale factors (SF) to the simulation that are defined as

$$SF = \frac{\epsilon_{\text{data}}}{\epsilon_{\text{MC}}} \quad (5.4)$$

These scale factors are measured for the identification, isolation, tracking and trigger efficiencies of the objects as a function of  $p_T$  and  $\eta$  (see [Section 4.4.1](#) and [Section 4.4.2](#)). Multiplying these scale factors for each lepton provides an overall efficiency:

$$SF_{\text{global}}^{\mu} = \prod_i^{\#\mu} SF_{\text{ID}}^{\mu}(p_T, \eta) SF_{\text{Iso.}}^{\mu}(p_T, \eta) SF_{\text{Trig.}}^{\mu}(p_T, \eta) SF_{\text{track}}^{\mu}(p_T, \eta), \quad (5.5)$$

$$SF_{\text{global}}^e = \prod_i^{\#e} SF_{\text{ID}}^e(p_T, \eta) SF_{\text{Iso.}}^e(p_T, \eta) SF_{\text{Trig.}}^e(p_T, \eta) SF_{\text{track}}^e(p_T, \eta). \quad (5.6)$$

1417 The effect of the scale factors can be found in [Figure 5.6](#) for the electron scaling and [Figure 5.5](#)  
 1418 for the muons. The trigger efficiencies are estimated in [Section 5.1.2](#).

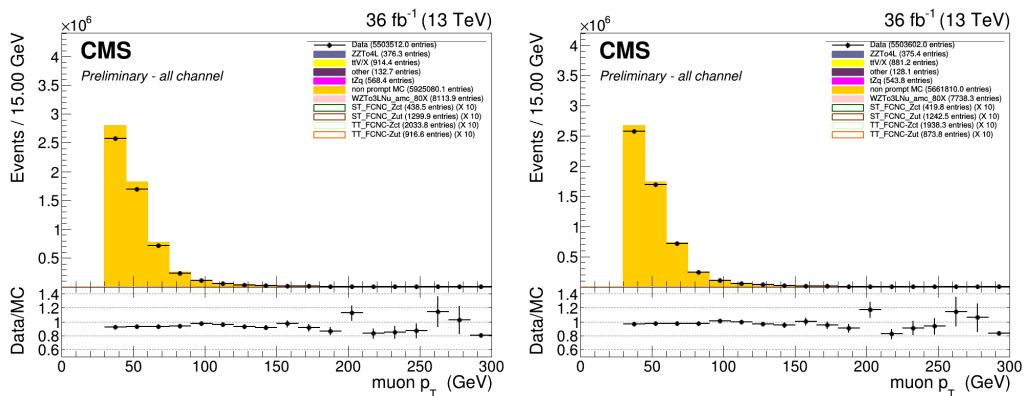


**Figure 5.5:** The  $p_T$  of the muons before (left) and after (right) muon scale factors. After a 2 lepton plus jets selection, in the Z mass window. Both after the Rochester correction.

1419 Additionally, corrections are made for the energy resolution of the leptons. For the electrons,  
 1420 energy smearing and regression is applied [179]. The energy regression uses the detector  
 1421 information to correct the electron energy in order to have the best energy resolution by  
 1422 correcting local energy containment, material effects, etc.. The energy scale and smearing

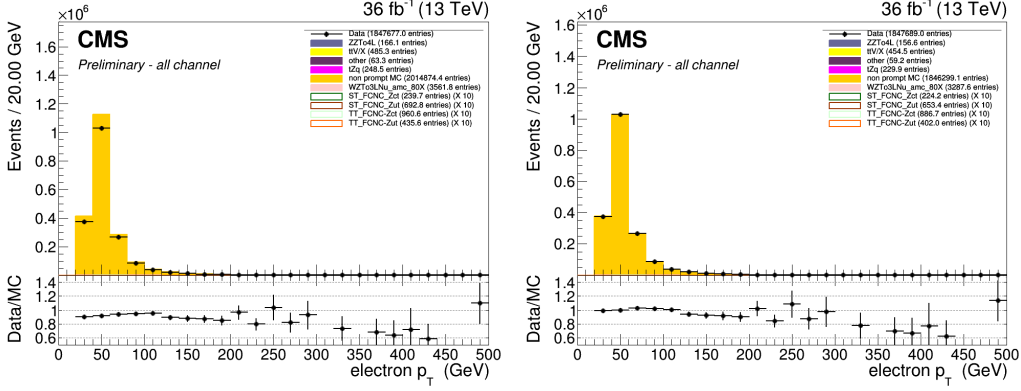


**Figure 5.6:** The  $p_T$  of the electrons before (left) and after (right) electron scale factors. After a 2 lepton plus jets selection, in the Z mass window. Both after energy scale corrections and smearing.

is done in order to bring the data energy scale to simulation level. It smears the simulation energies to have identical energy resolution in simulation and data. For the muons, the  $p_T$  is corrected using the Rochester method [180, 181]. This correction removes the bias of the muon  $p_T$  from any detector misalignment or any possible error of the magnetic field. The effect of the Rochester correction can be found in [Figure 5.7](#).

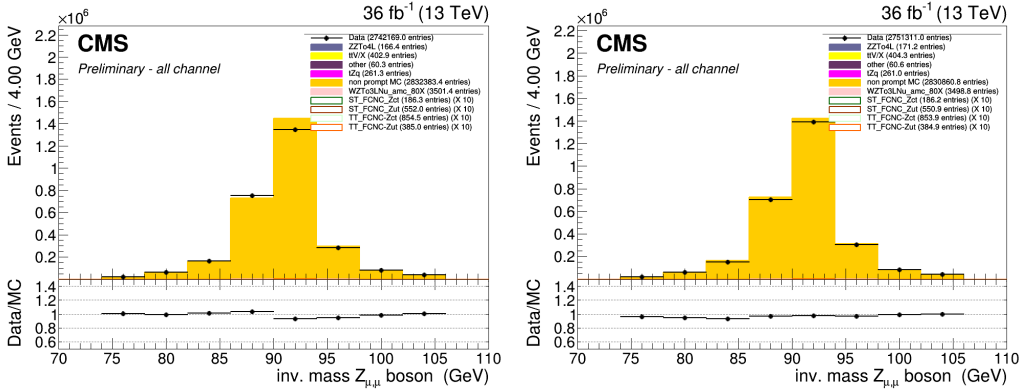


**Figure 5.7:** The mass of the Z boson consisting of the muons before (left) and after (right) the rochester correction. After a 2 lepton plus jets selection, in the Z mass window.

1428 **CSVv2 shape correction**

1429 In order to make the shape of the CSVv2 b-tagging discriminant in simulation agree with data,  
 1430 jet-by-jet based scale factors are applied. These scale factors are a function of the  $p_T$ ,  $\eta$  and  
 1431 CSVv2 value of the jet as discussed in [Section 4.4.4](#). The effect of these scale factors can be  
 1432 found in [Figure 5.8](#).

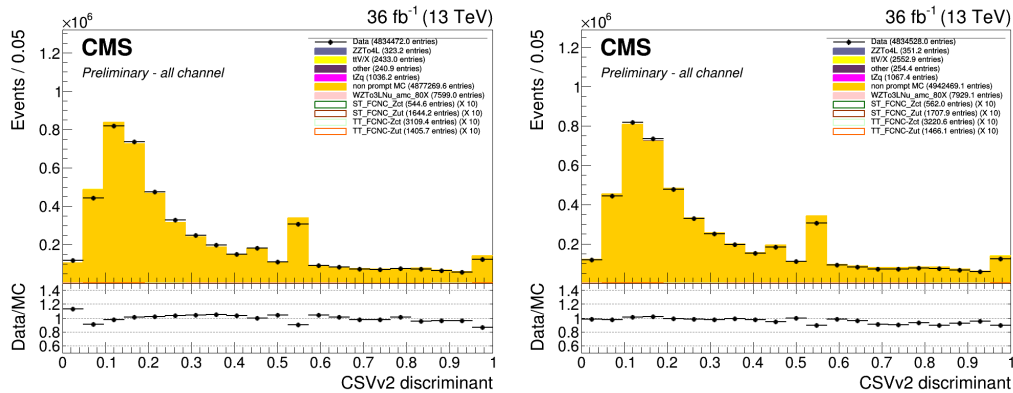


**Figure 5.8:** The CSVv2 discriminant of the jets before (left) and after (right) b-tag scale factors. After a 2 lepton plus jets selection, in the Z mass window.

1433 **Jet energy**

1434 The jet energy in data and simulation is corrected by the measured energy response of the  
 1435 detector. This provides  $p_T$ -  $\eta$  dependent scale factors and are directly taken from the frontier  
 1436 condition database as discussed in [Section 4.4.3](#). The effect of the jet energy corrections can be  
 1437 found in [Figure 5.9](#) and [Figure 5.10](#).

**NOTE:** Fix  
jer plot

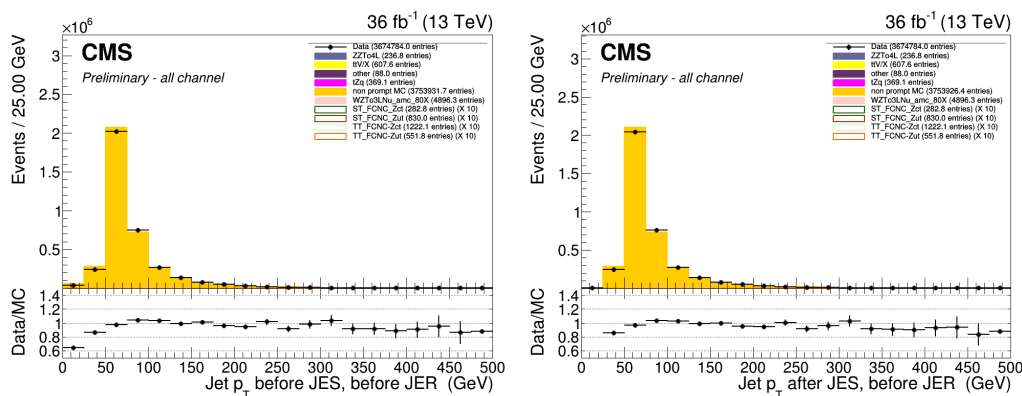


**Figure 5.9:** The  $p_T$  of the jets before (left) and after (right) jet energy scale corrections. After a 2 lepton plus jets selection, in the Z mass window.

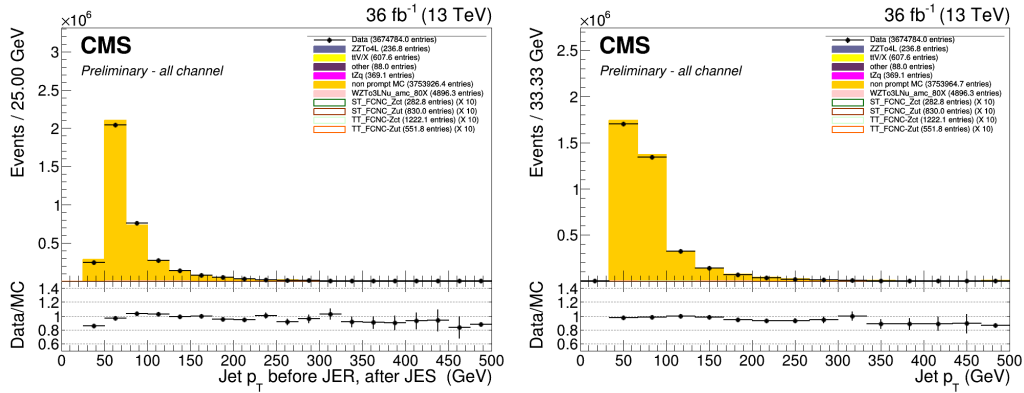


**Figure 5.10:** The  $p_T$  of the jets before (left) and after (right) jet energy resolution smearing. After a 2 lepton plus jets selection, in the Z mass window.

### 1438 Missing transverse energy

1439 The energy scale and resolution corrections applied to the jets are propagated back to the  
 1440 missing transverse energy (smeared Type I correction). This rebalances the transverse net  
 1441 momentum of the event and improves the missing transverse energy resolution itself.

## 1442 5.2 Analysis Strategy

1443 The analysis strategy uses five statistically independent regions to extract limits using a likelihood  
 1444 fit of various observables. Two signal regions, the tZ (STS<sub>R</sub>) and tZq (TTS<sub>R</sub>) signal region, are  
 1445 constructed using the jet multiplicity, focussed on each signal signature (see Tab. 5.7). In order  
 1446 to constrain the rate of WZ+jet events as well as that of NPL backgrounds three control regions  
 1447 are defined. The WZ control region (WZCR) focusses on NPLs originating from  $Z/\gamma^*$  + jets and  
 1448 simultaneously constrains the WZ+jets background rate. The NPL backgrounds coming from  
 1449  $t\bar{t}$ , are constrained by two control regions, TT<sub>CR</sub> and ST<sub>CR</sub>, one for each signal region (TTS<sub>R</sub>  
 1450 and STS<sub>R</sub>). In the STS<sub>R</sub> and TTS<sub>R</sub> multivariate discriminants based on Boosted Decision Trees  
 1451 (BDT) are used to respectively discriminate FCNC tZ and FCNC tZq from backgrounds. In the  
 1452 WZCR a discriminating variable between the two backgrounds, WZ+jets and NPLs, is used.  
 1453 In TT<sub>CR</sub> and ST<sub>CR</sub> the dominating process is  $t\bar{t}$ +jets, and its rate is estimated by subtracting  
 1454 all other background predictions from data. A simultaneous global fit is performed taking  
 1455 into account each region (STS<sub>R</sub>, TTS<sub>R</sub>, WZCR, TT<sub>CR</sub> and ST<sub>CR</sub>) for the four different leptonic  
 1456 channels.

## 1457 5.3 Data driven NPL background simulation

1458 The MC samples are used to model the backgrounds as well as for training the boosted decision  
 1459 trees for signal to background separation. One of the most important background consist of  
 1460 events with not prompt leptons. These are mostly instrumental background and are therefore  
 1461 very difficult to model. The NPL background is estimated from data for both its shape and its  
 1462 normalisation.

1463 The NPL sources are

- 1464 • hadronic objects wrongly reconstructed as leptons,  
 1465 • real leptons coming from the semi leptonic decay of a b or c hadron,  
 1466 • real leptons coming from the conversion of photons,

1467 that pass the identification and isolation requirements. The dominant source of these NPLs  
 1468 depend on the flavour of the lepton and therefore the events with a noy prompt muon (NP $\mu$ )  
 1469 are treated differently than those with a not prompt electron (NPE). For muons, the dominant  
 1470 source is the semi leptonic decay of heavy flavour hadrons. For electrons, the dominant sources  
 1471 are hadrons and photon conversions.

1472 The backgrounds causing NPL contributions are mostly  $Z/\gamma^*$  + jets(Drell–Yan) and  $t\bar{t}$ +jets  
 1473 dilepton processes, and in a smaller amount WW and tWZ. All of these backgrounds contain  
 1474 two real leptons and one NPLDue to the fact that the probability for a lepton to be a NPL is  
 1475 small, backgrounds containing two or more NPL s are neglected. The assumption is made that  
 1476 for DY the two leptons compatible with a Z boson decay are the real leptons, and the additional  
 1477 lepton is coming from a NPL source, while for  $t\bar{t}$ +jets the NPL is associated to the Z boson.

1478 The NPL sample is constructed from data by requiring exactly three leptons, from which two  
 1479 are considered real, isolated leptons and the third is a NPL. This NPL is created by loosening its  
 1480 identification and inverting its isolation criteria. The full requirements on the not prompt leptons  
 1481 are given in [Table 5.5](#) and [Table 5.6](#). For NPEs, a large fraction is coming from misidentified  
 1482 photons. These are removed by applying a tighter cut on the  $1/E - 1/p$  variable, and by limiting  
 1483 the isolation values to be smaller than one.

1484 The NPL samples are defined in a given control region and are used to describe their contribu-  
 1485 tion in the other regions.

## 1486 5.4 Regions and channels

1487 The regions are defined as in Table [5.7](#) after a common selection of

- 1488 • exactly 3 leptons containing one opposite sign, same flavour pair that are assigned to the  
 1489 Z boson,  
 1490 • at least 1 jet and at the most 3 jets,  
 1491 • the transverse mass of the W boson to be maximal 300 GeV,

The cut on the transverse mass of the W boson is done to remove events that are passing the events cleaning elading to anomalous large missing transverse energy. The transverse mass  $m_T(W)$  is reconstructed using

$$m_T(W) = \sqrt{(p_T(l_W) + p_T(v_W))^2 - (p_x(l_W) + p_x(v_W))^2 - (p_y(l_W) + p_y(v_W))^2} \quad (5.7)$$

**Table 5.5:** Non prompt electron requirements used in this analysis. The requirements are set in the barrel ( $|\eta_{supercluster}| \leq 1.479$ ) and the end caps ( $|\eta_{supercluster}| > 1.479$ ).

	$ \eta_{supercluster}  \leq 1.479$	$ \eta_{supercluster}  > 1.479$
$\sigma_{\eta\eta}$	< 0.011	< 0.0314
$ \Delta\eta_{in} $	< 0.00477	< 0.00868
$ \Delta\phi_{in} $	< 0.222	< 0.212
H/E	< 0.298	< 0.101
relative isolation	$\geq 0.0588 \ \&\ & < 1$	$\geq 0.0571 \ \&\ & < 1$
$ 1/E - 1/p $	$< 0.0129 \text{ GeV}^{-1}$	$< 0.0129 \text{ GeV}^{-1}$
expected missing inner hits	$\leq 1$	$\leq 1$
pass conversion veto	Y	Y
$p_T$	$> 35 \text{ GeV}$	$> 35 \text{ GeV}$

**Table 5.6:** Non prompt muon requirements used in the analysis.

	modified Loose Muon WP
Global muon or Tracker Muon	Both
Particle Flow muon	Y
$\chi^2/ndof$ of global muon track fit	N/A
Nb. of hit muon chambers	N/A
Nb. of muon stations contained in the segment	N/A
Size of the transverse impact parameter of the track wrt. PV	N/A
Longitudinal distance wrt. PV	N/A
Nb. of pixel hits	N/A
Nb. of tracker layers with hits	N/A
Relative Isolation	$\geq 0.15$
$p_T$	$> 30 \text{ GeV}$

**Table 5.7:** The statistically independent regions used in the analysis.

	WZCR	STS R	TTSR	STCR	TTCR
Number of jets	$\geq 1$	1	$\geq 2$	1	$\geq 2$
Number of b jets	0	1	$\geq 1$	1	$\geq 1$
$ m_Z^{\text{reco}} - m_Z  < 7.5 \text{ GeV}$	Yes	Yes	Yes	No	No

Additional leptons are vetoed in order to reduce the contamination of backgrounds with four or more leptons in the final state, e.g. ZZ,  $t\bar{t}Z$ , and  $t\bar{t}H$ . The most important backgrounds are the ones that contain three prompt leptons in the final state. These are mainly WZ+jets,  $t\bar{t}Z$  and SM tZq. For these backgrounds, the three lepton topology is identical to the FCNC signal: two opposite sign leptons of the same flavour decaying from the Z boson, and a third additional, high  $p_T$  lepton coming from the W boson decay.

For the FCNC tZ final state, one b jet coming from the SM top decay is expected. For the FCNC tZq, an additional light jet is expected. In the  $t\bar{t}Z$  final state, two b jets are present in the final state. However, due to inefficiencies of the b-tagging algorithm, one of the two b jets may be identified as a light quark jet, giving the same final state as the FCNC tZq final state. For the WZ+jets final states, one of the b jets produced by gluon splitting can be b-tagged or light flavour jets coming from the WZ+jets production can be mis-tagged as b jets. The SM tZq final state expects the same signal as FCNC tZq.

The NPL events give a significant background contribution. This background is coming mainly from  $Z/\gamma^* + \text{jets}$  and  $t\bar{t} + \text{jets}$  processes (in a less significant way, also WW and tWZ contributes), which have very high cross sections and causes a large number of NPL background events compared to signal.

In order to reduce the large uncertainties in backgrounds, five independent regions are used as defined in Table 5.7.

### 5.4.1 WZ control region

In this region, a fit is performed on the transverse mass of the W boson, in order to estimate the NPL yield coming from  $Z/\gamma^* + \text{jets}$  and the WZ+jets backgrounds.

A transfer factor is used to account for going from a region without b-tagged jets to a region with exactly one b-tagged jet, or at least one b-tagged jet. For this the probability of tagging at least one jet with the CSVv2 loose working point is used to calculate the expected number of events,  $N_b$ , after b tagging:

$$N_b = \frac{\sum_{\text{events}} \mathcal{P}_b}{\text{total nb of events}}, \quad (5.8)$$

where  $\mathcal{P}_b$  is the probability that an event survives the b-tagging requirement

$$\begin{aligned}\mathcal{P}_b &= 1 - P(\text{event doesn't survive b tag}) \\ &= 1 - \left( \prod_b P(\text{b not tagged}) \prod_c P(\text{c not tagged}) \prod_{uds} P(\text{light not tagged}) \right) \quad (5.9)\end{aligned}$$

with the products going over all b-, c-, and light jets. The jet flavour is determined by means of matching the reconstructed jet to the generated quark based on the distance in the  $\eta\phi$  plane. In order to estimate the probability for exactly one b-tagged jet, the expected number of events is corrected by the fraction of events with exactly one jet in the WZCR. The resulting transfer factors are given in [Appendix C](#). One can see that the yield of WZ+jets events in the signal region estimated using the above described transfer factor and the yield calculated with simulated events are in agreement.

**NOTE:** make app  
pendix

#### 5.4.2 TTCSR and STCSR

The TTCSR and STCSR have the same selection criteria as TTSR and STSR but are outside the Z mass window (sidebands):

$$7.5 \text{ GeV} < |m_Z^{\text{reco}} - m_Z| < 30 \text{ GeV}. \quad (5.10)$$

where  $M(Z_{\text{reco}})$  is the reconstructed mass of the Z boson in the event, and  $M(Z)$  the mass of the Z boson. These regions are dominated by  $t\bar{t}$ +jets (see [Appendix C](#)) and are used to estimate the NPL coming from  $t\bar{t}$ +jets in the STSR and TTSR. Since there aren't enough events entering these regions, no shapes are used in the fit. The distribution of the mass of the Z boson is flat for  $t\bar{t}$ +jets events, as shown in Fig. [Figure 5.11](#), and thus the number of expected events,  $N_s$ , in the signal regions estimated from the number of expected events,  $N_c$ , in the control region is obtained as

$$N_s = \frac{15}{60 - 15} N_c. \quad (5.11)$$

The resulting transfer factors are given in [Appendix C](#). The expected yield in the signal region estimated from the TTCSR (STCSR) is in agreement with the yield calculated from simulated events.

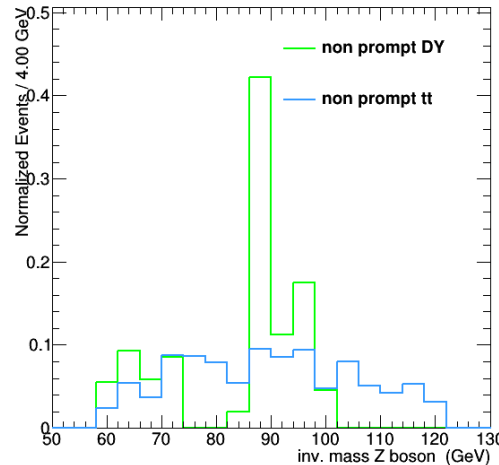


**Figure 5.11:** The normalized distribution for  $Z/\gamma^* + \text{jets}$  and  $t\bar{t} + \text{jets}$  events before dividing the events in to regions, after  $|m_Z^{\text{reco}} - m_Z| < 30$  GeV. All leptonic channels combined.

### 1525 5.4.3 TTSR and STSR

1526 The TTSR is defined to target top quark pair FCNC ( $tZq$ ), while the STSR focusses on single top  
 1527 quark FCNC ( $tZ$ ). They have NPL contributions coming from  $Z/\gamma^* + \text{jets}$  and  $t\bar{t} + \text{jets}$  events. In  
 1528 this region, the data driven NPL template is split into two templates based on the presence of  
 1529 the NPL in the  $Z$  boson:

- 1530 • NPL associated with  $W$  boson is assigned to  $Z/\gamma^* + \text{jets}$  and estimated in the WZCR.  
 1531 • NPL associated with  $Z$  boson is assigned to  $t\bar{t} + \text{jets}$  and estimated in the TTCR and STCR.



# The search for FCNC involving a top quark and a Z boson

1532

6

1533 **6.1 Construction of template distributions**

1534 **6.2 Systematic uncertainties**

1535 **6.3 Limit setting procedure**

1536 **6.4 Result and discussion**



# Denouement of the top-Z FCNC hunt at 13 TeV

1537

7

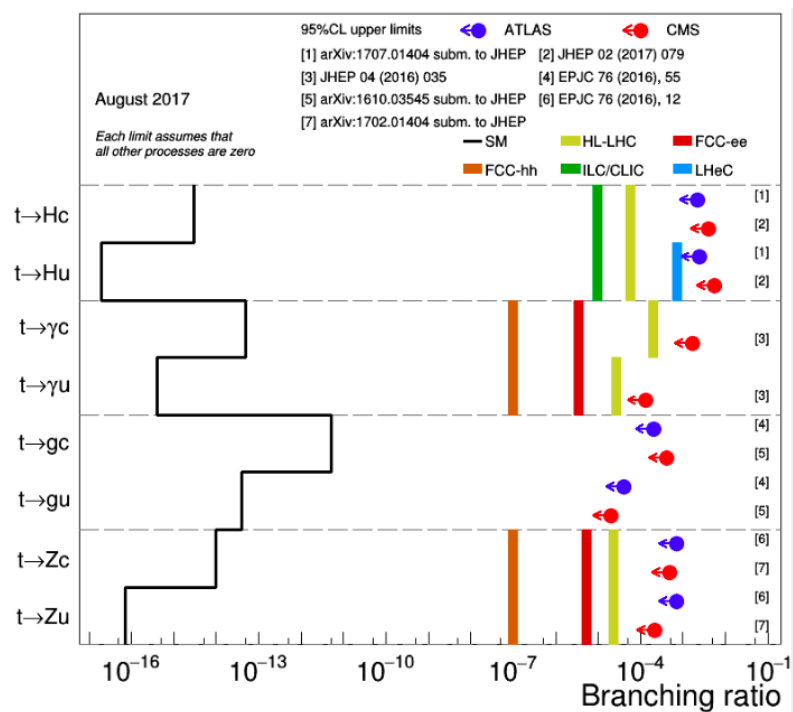


Figure 7.1:



# Trigger scale factors



1539 The trigger scale factors measured as a function of lepton  $p_T$ , using the dataset collected by  
 1540  $E_T^{\text{miss}}$  triggers and WZ simulation, after a 3 lepton and jets selection, in the Z mass window. All  
 1541 corrections to simulation are applied.

**Table A.1:** Trigger efficiencies on data events selected with  $E_T^{\text{miss}}$  triggers and WZ simulation for all leptonic channels together. The unweighed number of events is quoted. When there are no events passing the cuts, it is indicated with N/A. The uncertainties are statistical uncertainties.

ALL CHANNEL	data		WZ simulations	
	Efficiency	unc.	Efficiency	unc.
3 lep, at least one jet	117/118 = 99.15 %	12.94%	18047/18055 = 99.96%	1.05%
STSR	6/6 = 100.00%	57.74%	1541/1541 = 100.00%	3.60%
TTSR	26/27 = 96.30%	26.46%	1791/1792 = 99.94%	3.34%
WZCR	69/69 = 100.00 %	17.03%	14405/14412=99.95%	1.18%

**Table A.2:** Trigger efficiencies on data events selected with  $E_T^{\text{miss}}$  triggers and WZ simulation for  $\mu\mu\mu$  leptonic channel together. The unweighed number of events is quoted. When there are no events passing the cuts, it is indicated with N/A. The uncertainties are statistical uncertainties.

$\mu\mu\mu$ CHANNEL	data		WZ simulations	
	Efficiency	unc.	Efficiency	unc.
3 lep, at least one jet	40/40 = 100.00 %	22.36 %	7814/7814 = 100.00%	1.60%
STSR	N/A	N/A	687/687 = 100%	5.40%
TTSR	13/13 = 100.00%	39.22%	763/763 = 100.00%	5.12%
WZCR	22/22 = 100.00 %	30.15%	6238/6238=100.00%	1.79%

**Table A.3:** Trigger efficiencies on data events selected with  $E_T^{\text{miss}}$  triggers and WZ simulation for eee leptonic channel together. The unweighed number of events is quoted. When there are no events passing the cuts, it is indicated with N/A. The uncertainties are statistical uncertainties.

eee CHANNEL	data		WZ simulations	
	Efficiency	unc.	Efficiency	unc.
3 lep, at least one jet	20/21 = 95.24%	29.76%	2211/2215 = 99.82 %	3.00%
STSR	4/4 = 100.00%	70.71%	176/176 = 100.00%	10.66%
TTSR	2/3 = 66.67%	60.86%	242/242 = 100.00%	9.09%
WZCR	14/14 = 100.00 %	37.80%	1744/1748=99.77%	3.38%

**Table A.4:** Trigger efficiencies on data events selected with  $E_T^{\text{miss}}$  triggers and WZ simulation for ee $\mu$  leptonic channel together. The unweighed number of events is quoted. When there are no events passing the cuts, it is indicated with N/A. The uncertainties are statistical uncertainties.

ee $\mu$ CHANNEL	data		WZ simulations	
	Efficiency	unc.	Efficiency	unc.
3 lep, at least one jet	32/32 = 100.00 %	25.00 %	3116/3118 = 99.94%	2.53%
STSR	1/1 = 100.00%	141.42%	255/255 = 100%	8.86%
TTSR	9/9 = 100.00%	47.14%	291/291 = 100.00%	8.29%
WZCR	14/14 = 100.00 %	37.80%	2529/2531=99.92%	2.81%

**Table A.5:** Trigger efficiencies on data events selected with  $E_T^{\text{miss}}$  triggers and WZ simulation for e $\mu\mu$  leptonic channel together. The unweighed number of events is quoted. When there are no events passing the cuts, it is indicated with N/A. The uncertainties are statistical uncertainties.

e $\mu\mu$ CHANNEL	data		WZ simulations	
	Efficiency	unc.	Efficiency	unc.
3 lep, at least one jet	25/25 = 100.00%	28.28%	4906/4908 = 99.96 %	2.02%
STSR	1/1 = 100.00%	141.42%	423/423 = 100.00%	6.88%
TTSR	2/2 = 100.00%	100.00%	495/496 = 99.80%	6.34%
WZCR	19/19 = 100.00 %	32.44%	3894/3895 =99.97%	2.27%

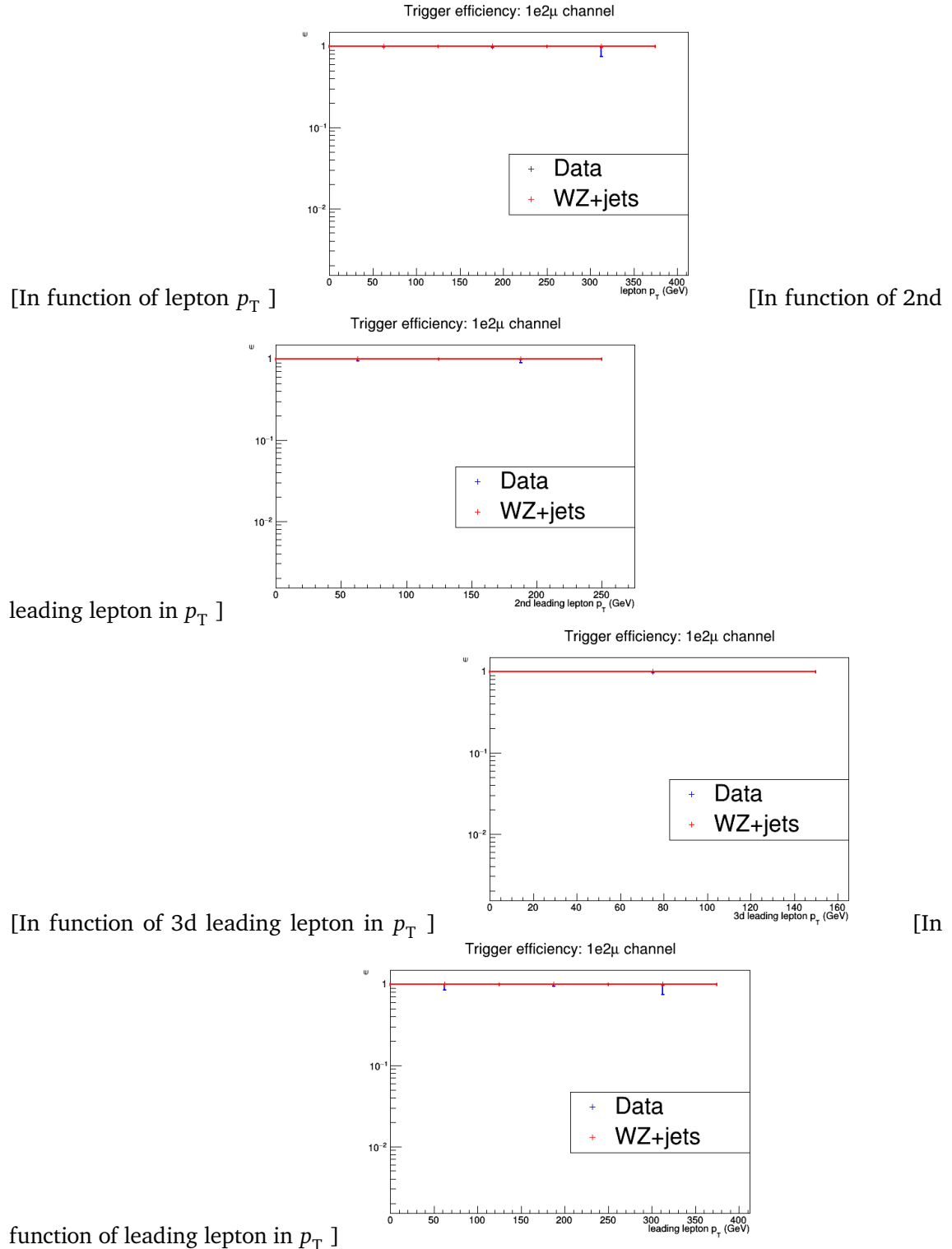


**Figure A.1:** The trigger efficiencies measured as a function of lepton  $p_T$ , using the dataset collected by  $E_T^{\text{miss}}$  triggers and WZ simulation, after a 3 lepton and jets selection, in the Z mass window. All corrections to simulation are applied. 1e2μ channel.

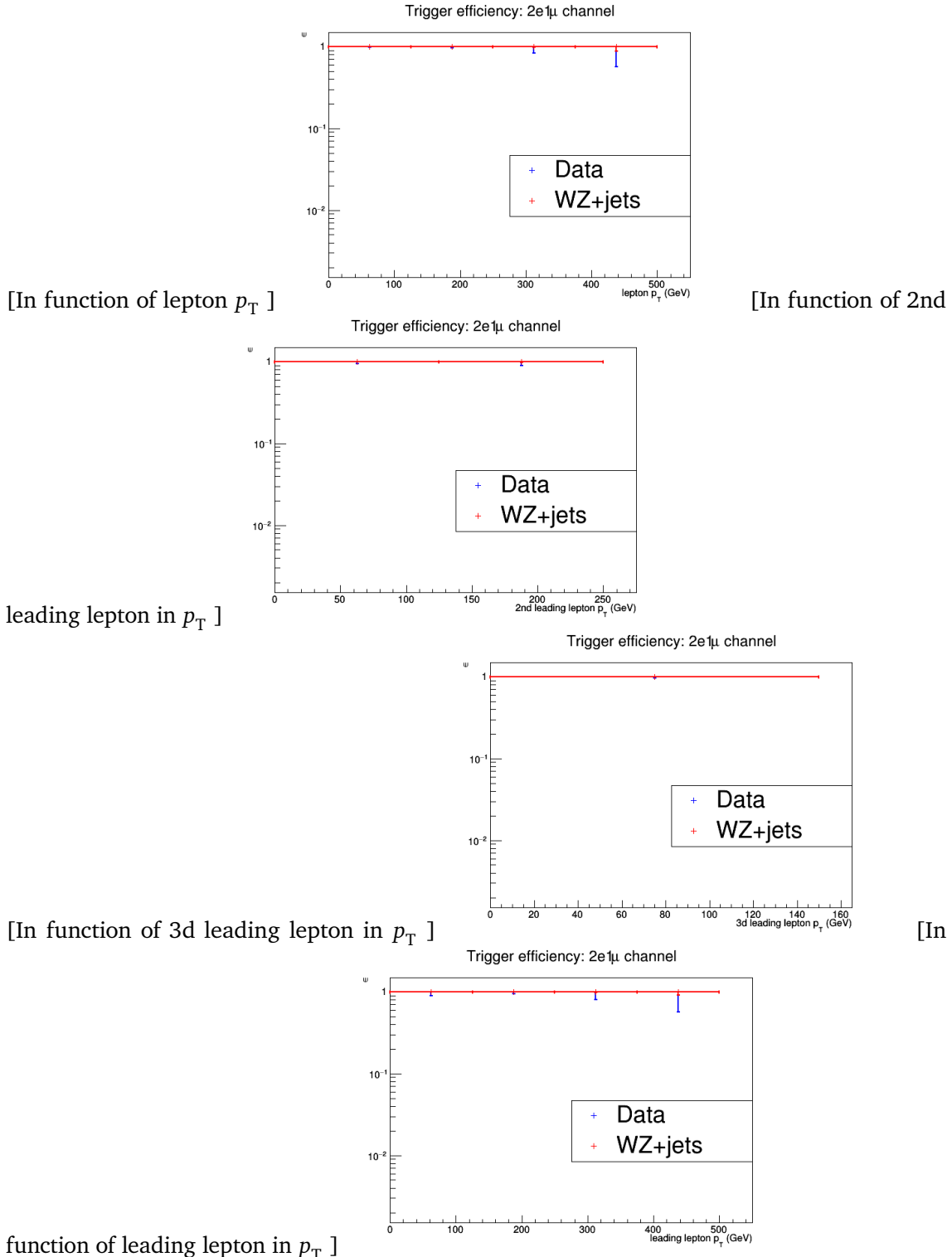


**Figure A.2:** The trigger efficiencies measured as a function of lepton  $p_T$ , using the dataset collected by  $E_T^{\text{miss}}$  triggers and WZ simulation, after a 3 lepton and jets selection, in the Z mass window. All corrections to simulation are applied. 2e1μ channel.

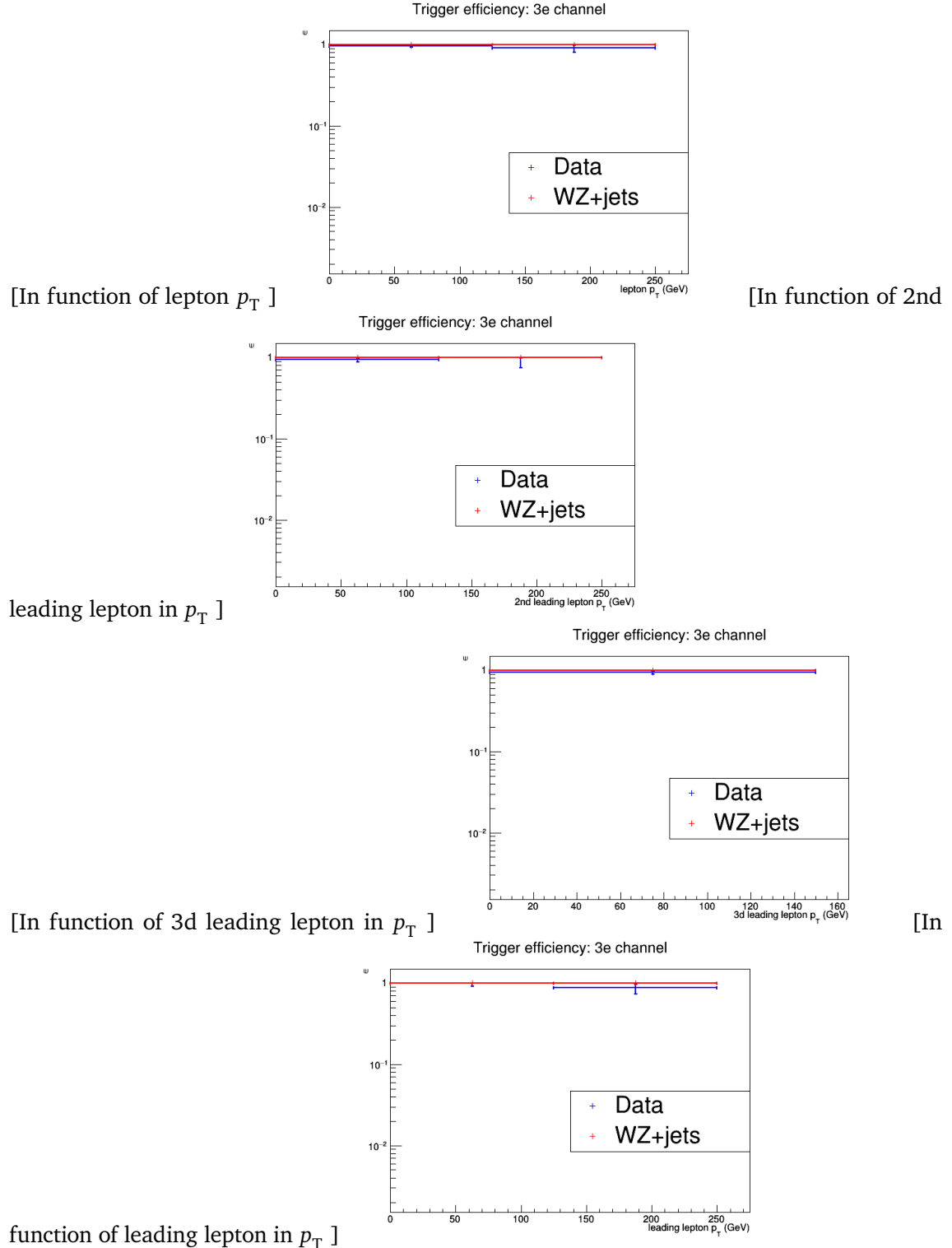


**Figure A.3:** The trigger efficiencies measured as a function of lepton  $p_T$ , using the dataset collected by  $E_T^{\text{miss}}$  triggers and WZ simulation, after a 3 lepton and jets selection, in the Z mass window. All corrections to simulation are applied. 3e channel.

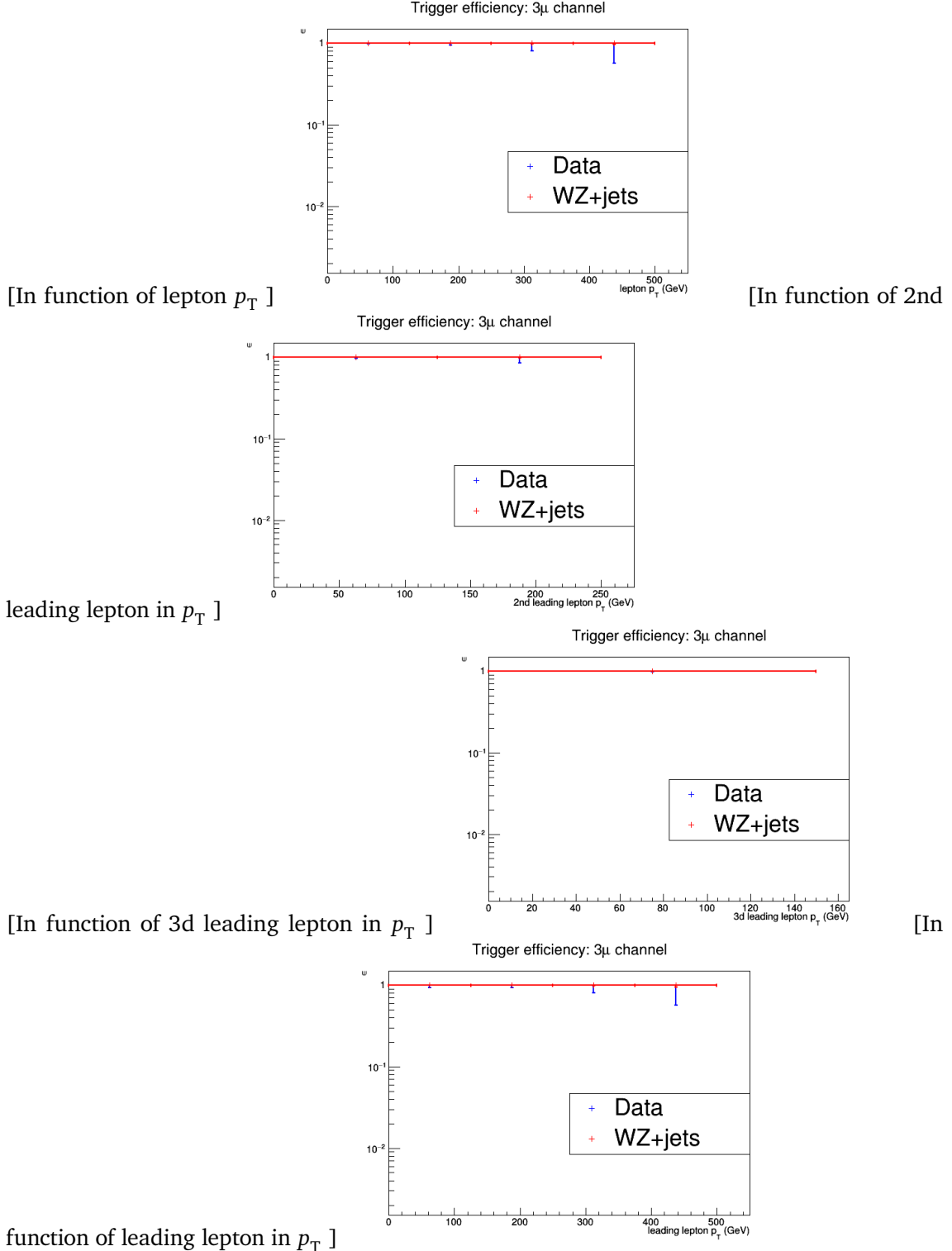


**Figure A.4:** The trigger efficiencies measured as a function of lepton  $p_T$ , using the dataset collected by  $E_T^{\text{miss}}$  triggers and WZ simulation, after a 3 lepton and jets selection, in the Z mass window. All corrections to simulation are applied. 3μ channel.

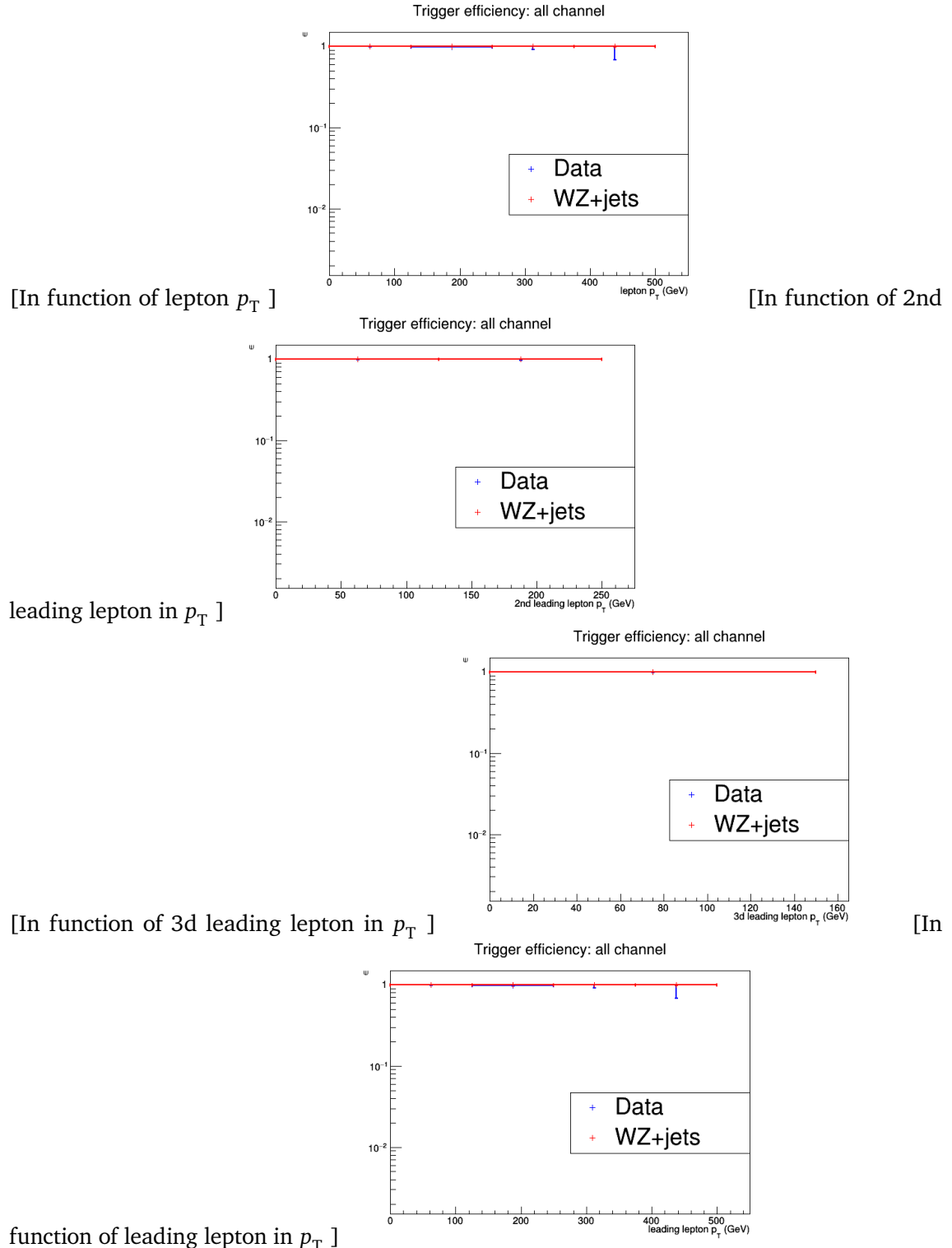


**Figure A.5:** The trigger efficiencies measured as a function of lepton  $p_T$ , using the dataset collected by  $E_T^{\text{miss}}$  triggers and WZ simulation, after a 3 lepton and jets selection, in the Z mass window. All corrections to simulation are applied. All channel.

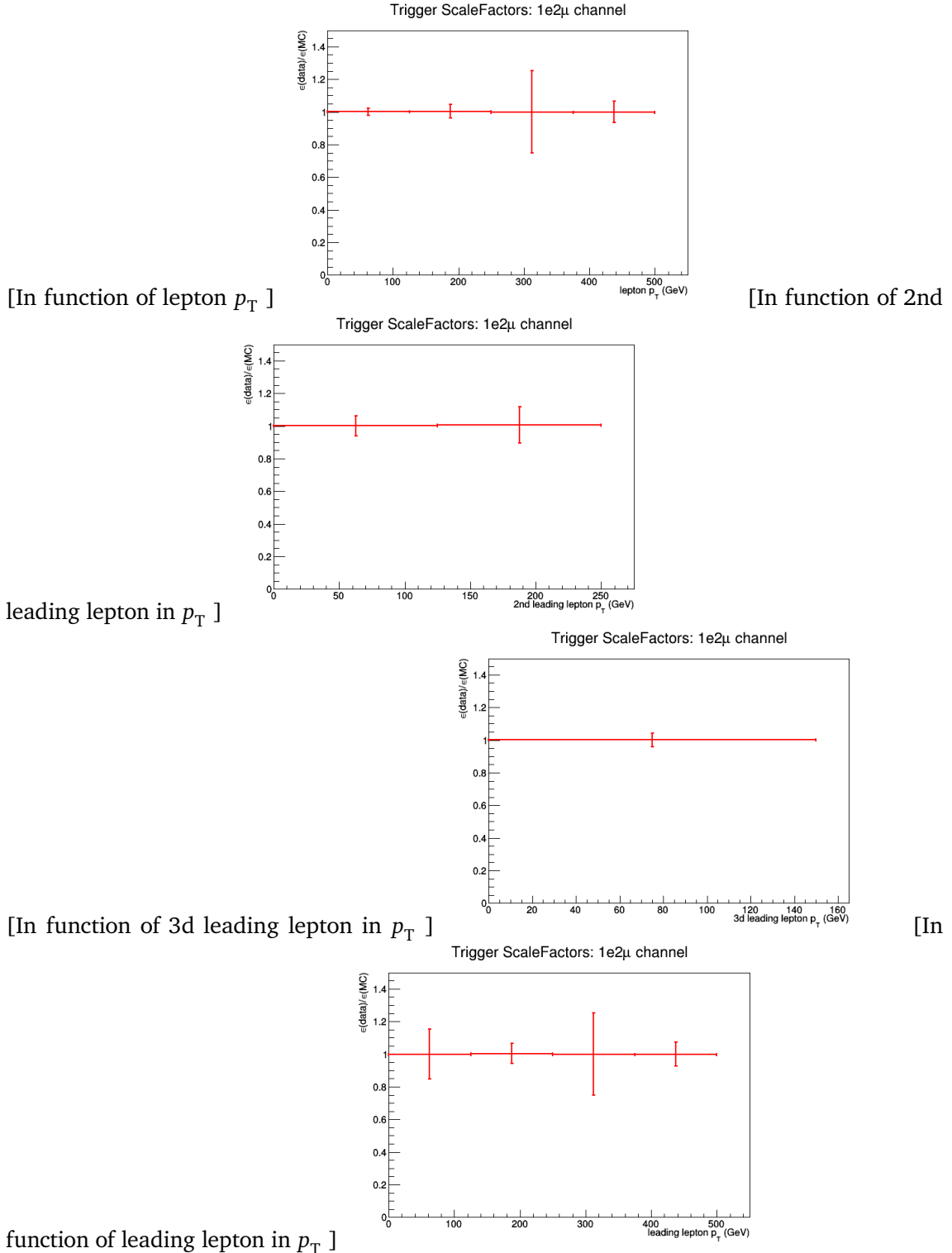


**Figure A.6:** The trigger scale factors measured as a function of lepton  $p_T$ , using the dataset collected by  $E_T^{\text{miss}}$  triggers and WZ simulation, after a 3 lepton and jets selection, in the Z mass window. All corrections to simulation are applied. 1e2μ channel.

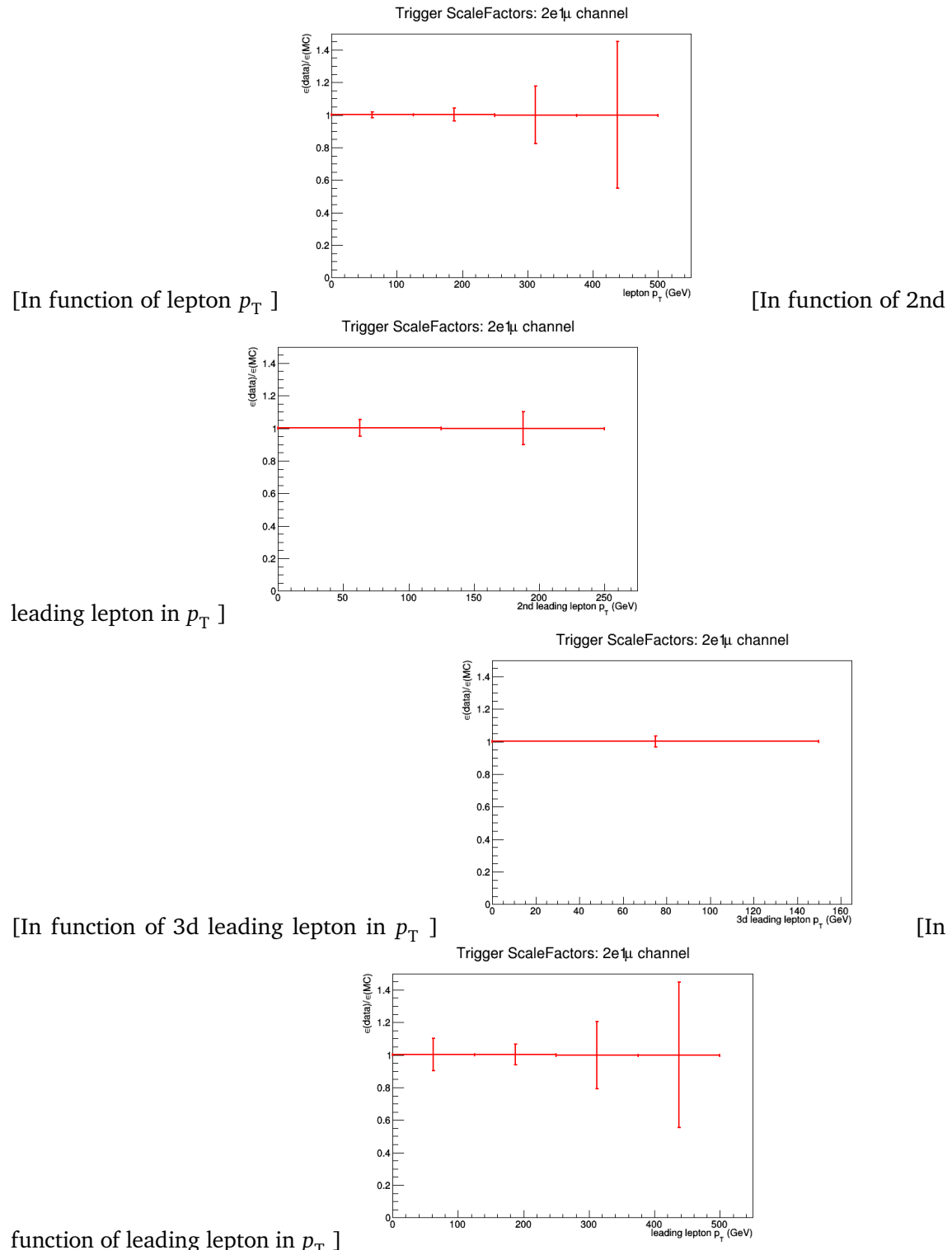


**Figure A.7:** The trigger scale factors measured as a function of lepton  $p_T$ , using the dataset collected by  $E_T^{\text{miss}}$  triggers and WZ simulation, after a 3 lepton and jets selection, in the Z mass window. All corrections to simulation are applied. 2e1μ channel.

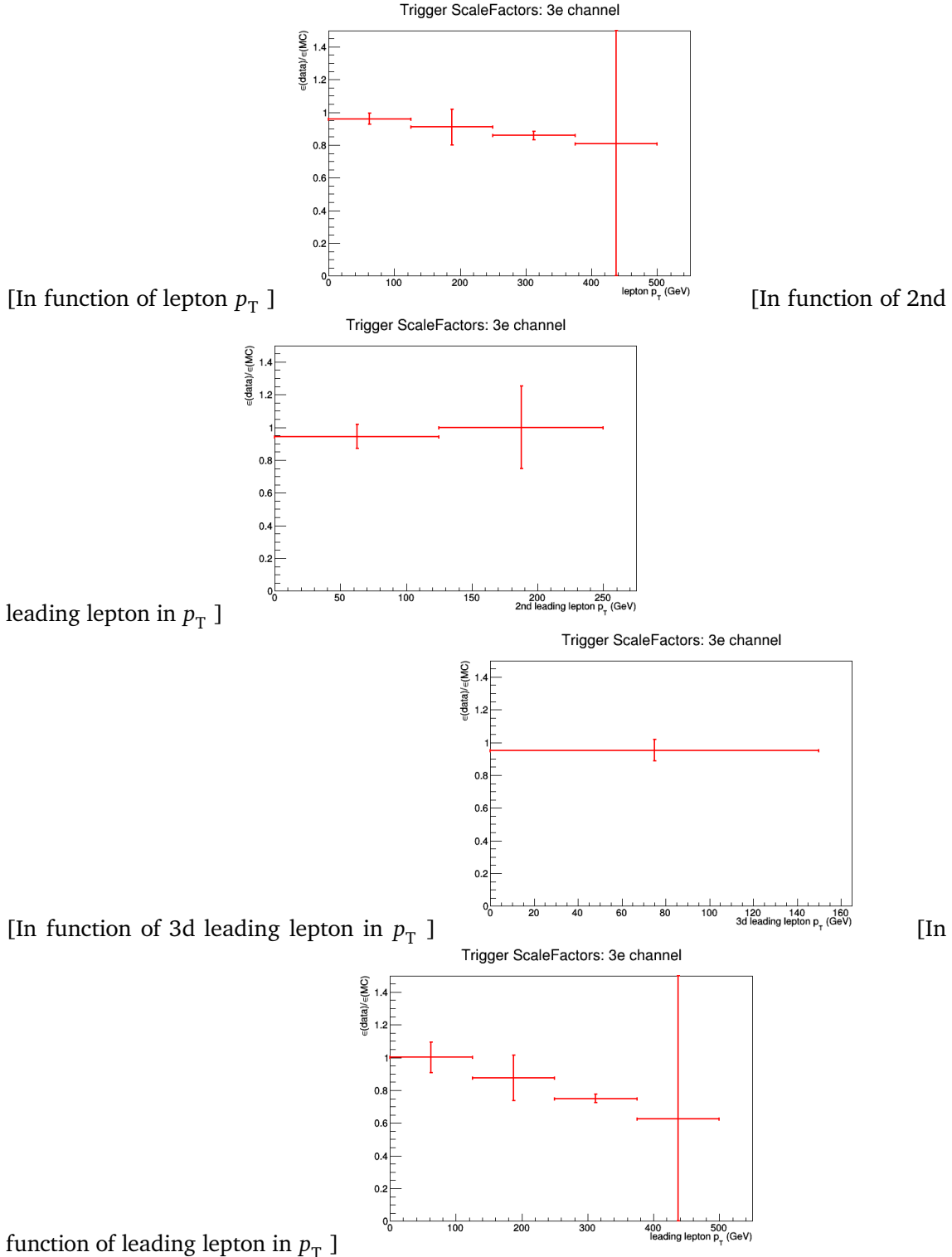


**Figure A.8:** The trigger scale factors measured as a function of lepton  $p_T$ , using the dataset collected by  $E_T^{\text{miss}}$  triggers and WZ simulation, after a 3 lepton and jets selection, in the Z mass window. All corrections to simulation are applied. 3e channel.

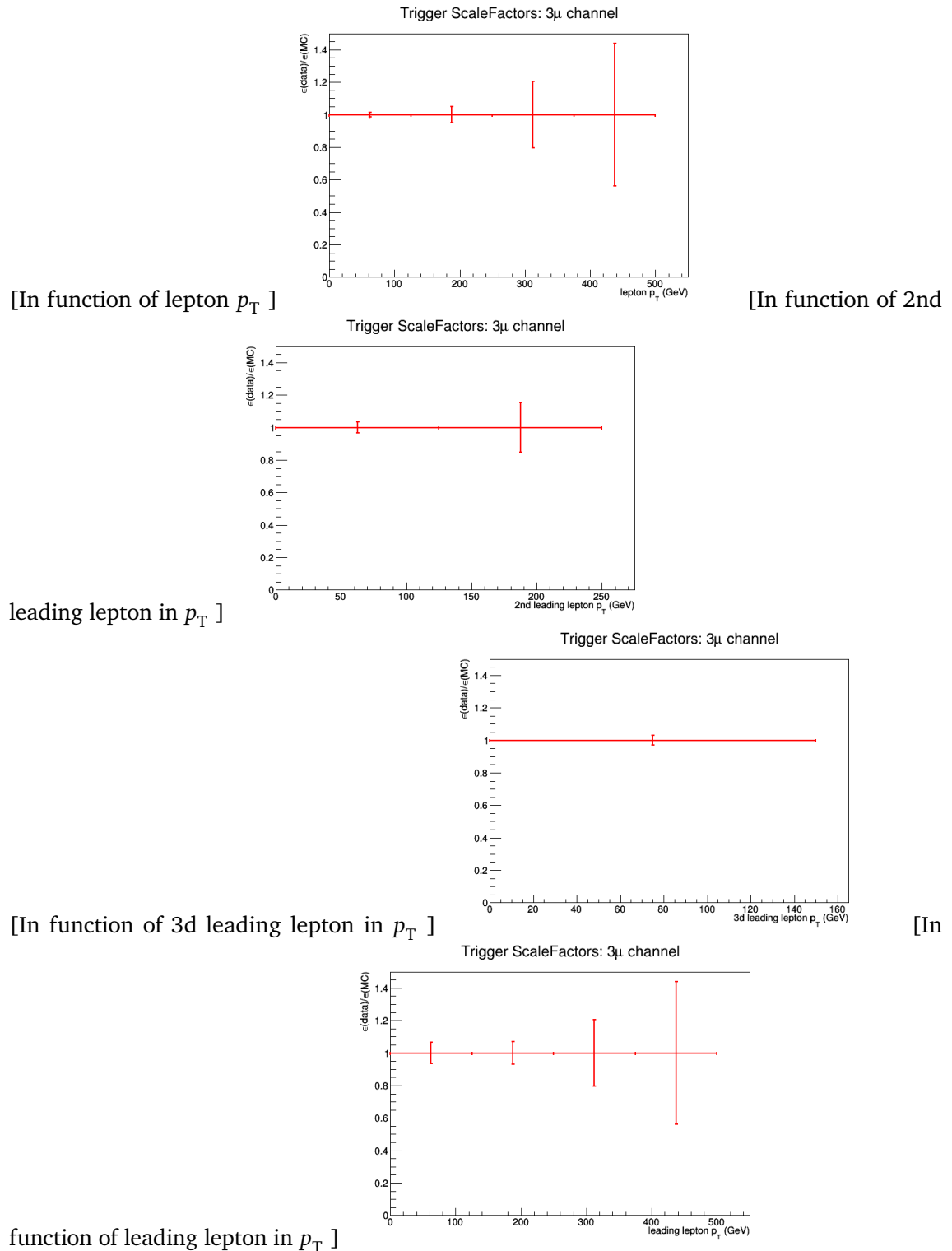


**Figure A.9:** The trigger scale factors measured as a function of lepton  $p_T$ , using the dataset collected by  $E_T^{\text{miss}}$  triggers and WZ simulation, after a 3 lepton and jets selection, in the Z mass window. All corrections to simulation are applied. 3μ channel.

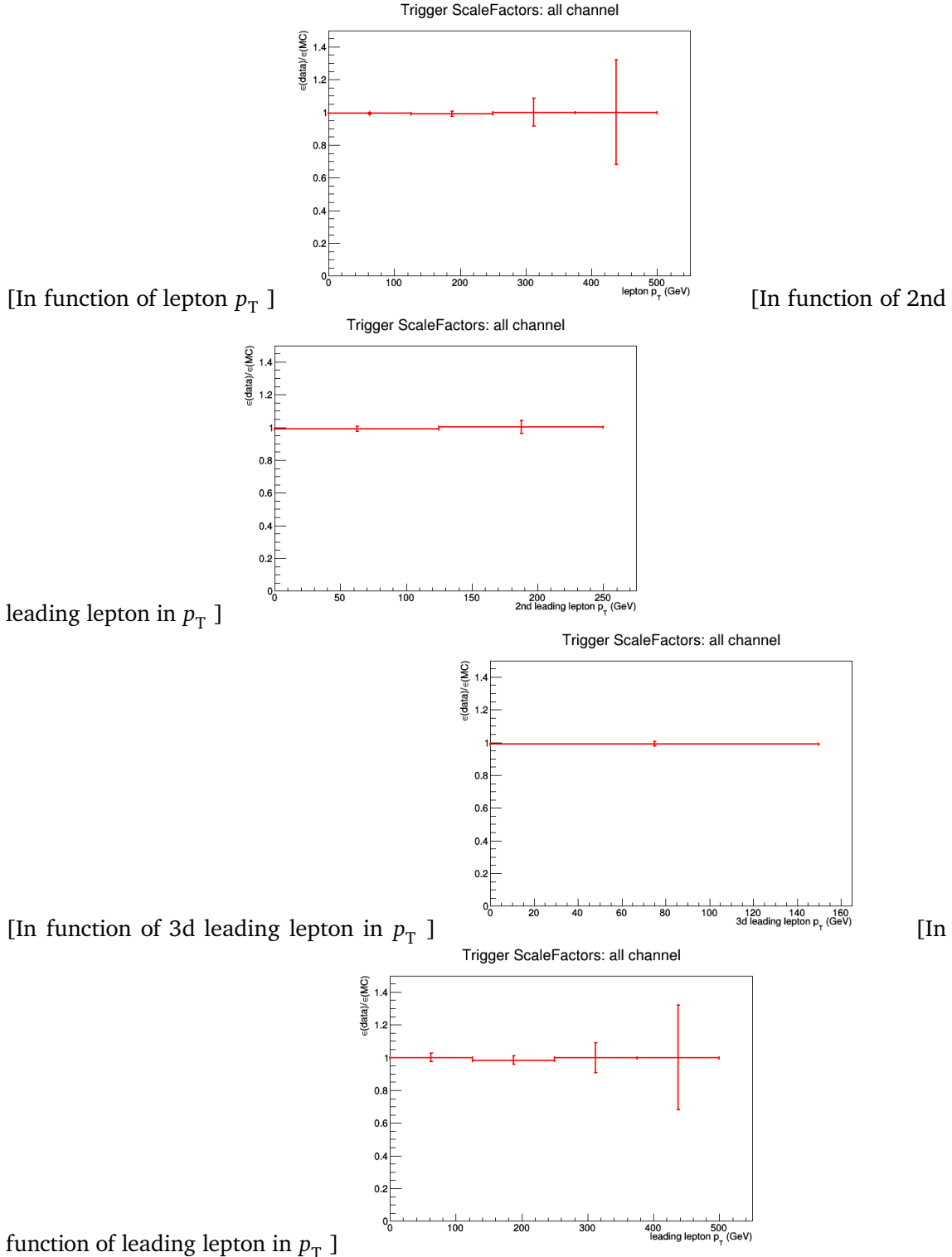


**Figure A.10:** The trigger scale factors measured as a function of lepton  $p_T$ , using the dataset collected by  $E_T^{\text{miss}}$  triggers and WZ simulation, after a 3 lepton and jets selection, in the Z mass window. All corrections to simulation are applied. All channel.

## Dilepton controlplots

B

---



# **Statistical independent regions**

---

1543

C



## Bibliography

---

- 1545 [1] MICHAEL E PESKIN and DANIEL V SCHROEDER: **An introduction to quantum field**  
 1546 **theory; 1995 ed.** Includes exercises. Boulder, CO: Westview, 1995. URL: <https://cds.cern.ch/record/257493> (see pp. 1, 5, 11, 16).
- 1547  
 1548 [2] C. P. BURGESS: **Introduction to Effective Field Theory**. In: *Ann. Rev. Nucl. Part. Sci.*, **57**: (2007), pp. 329–362. DOI: [10.1146/annurev.nucl.56.080805.140508](https://doi.org/10.1146/annurev.nucl.56.080805.140508). arXiv: [hep-th/0701053 \[hep-th\]](https://arxiv.org/abs/hep-th/0701053) (see p. 1).
- 1550  
 1551 [3] NADIA ROBOTTI: **The discovery of the electron: I**. In: *European Journal of Physics*,  
 1552 **18**:3 (1997), p. 133. URL: <http://stacks.iop.org/0143-0807/18/i=3/a=002> (see p. 2).
- 1553 [4] Y. FUKUDA et al.: **Evidence for oscillation of atmospheric neutrinos**. In: *Phys. Rev. Lett.*, **81**: (1998), pp. 1562–1567. DOI: [10.1103/PhysRevLett.81.1562](https://doi.org/10.1103/PhysRevLett.81.1562). arXiv: [hep-ex/9807003 \[hep-ex\]](https://arxiv.org/abs/hep-ex/9807003) (see pp. 2, 14).
- 1555  
 1556 [5] Y. ABE et al.: **Indication of Reactor  $\bar{\nu}_e$  Disappearance in the Double Chooz Experiment**. In: *Phys. Rev. Lett.*, **108**: (13 Mar. 2012), p. 131801. DOI: [10.1103/PhysRevLett.108.131801](https://doi.org/10.1103/PhysRevLett.108.131801) (see pp. 2, 14).
- 1558  
 1559 [6] C. PATRIGNANI et al.: **Review of Particle Physics**. In: *Chin. Phys.*, **C40**:10 (2016),  
 1560 p. 100001. DOI: [10.1088/1674-1137/40/10/100001](https://doi.org/10.1088/1674-1137/40/10/100001) (see pp. 2–3, 6–9, 42–43).
- 1561 [7] S. ABACHI et al.: **Observation of the top quark**. In: *Phys. Rev. Lett.*, **74**: (1995),  
 1562 pp. 2632–2637. DOI: [10.1103/PhysRevLett.74.2632](https://doi.org/10.1103/PhysRevLett.74.2632). arXiv: [hep-ex/9503003 \[hep-ex\]](https://arxiv.org/abs/hep-ex/9503003)  
 1563 (see p. 2).
- 1564 [8] F. ABE et al.: **Observation of top quark production in  $\bar{p}p$  collisions**. In: *Phys. Rev. Lett.*, **74**: (1995), pp. 2626–2631. DOI: [10.1103/PhysRevLett.74.2626](https://doi.org/10.1103/PhysRevLett.74.2626). arXiv: [hep-ex/9503002 \[hep-ex\]](https://arxiv.org/abs/hep-ex/9503002) (see p. 2).
- 1566  
 1567 [9] **First combination of Tevatron and LHC measurements of the top-quark mass**. In:  
 1568 (2014). arXiv: [1403.4427 \[hep-ex\]](https://arxiv.org/abs/1403.4427) (see p. 2).
- 1569 [10] SERGUEI CHATRCHYAN et al.: **Observation of a new boson at a mass of 125 GeV**  
 1570 **with the CMS experiment at the LHC**. In: *Phys. Lett.*, **B716**: (2012), pp. 30–61. DOI:  
 1571 [10.1016/j.physletb.2012.08.021](https://doi.org/10.1016/j.physletb.2012.08.021). arXiv: [1207.7235 \[hep-ex\]](https://arxiv.org/abs/1207.7235) (see pp. 2, 23).
- 1573 [11] GEORGES AAD et al.: **Observation of a new particle in the search for the Standard**  
 1574 **Model Higgs boson with the ATLAS detector at the LHC**. In: *Phys. Lett.*, **B716**:  
 1575 (2012), pp. 1–29. DOI: [10.1016/j.physletb.2012.08.020](https://doi.org/10.1016/j.physletb.2012.08.020). arXiv: [1207.7214 \[hep-ex\]](https://arxiv.org/abs/1207.7214)  
 (see pp. 2, 23).

- 1576 [12] NICOLA CABIBBO: **Unitary Symmetry and Leptonic Decays**. In: *Phys. Rev. Lett.*, **10**:  
 1577 (12 June 1963), pp. 531–533. doi: [10.1103/PhysRevLett.10.531](https://doi.org/10.1103/PhysRevLett.10.531) (see p. 5).
- 1578 [13] S. L. GLASHOW, J. ILIOPoulos, and L. MAIANI: **Weak Interactions with Lepton-Hadron  
 1579 Symmetry**. In: *Phys. Rev. D*, **2**: (7 Oct. 1970), pp. 1285–1292. doi: [10.1103/PhysRevD.2.1285](https://doi.org/10.1103/PhysRevD.2.1285) (see p. 5).
- 1580 [14] B.J. BJØRKEN and S.L. GLASHOW: **Elementary particles and SU(4)**. In: *Physics Letters*,  
 1581 **11**:3 (1964), pp. 255–257. doi: [https://doi.org/10.1016/0031-9163\(64\)90433-0](https://doi.org/10.1016/0031-9163(64)90433-0) (see  
 1582 p. 5).
- 1583 [15] LUCIANO MAIANI: **The GIM Mechanism: origin, predictions and recent uses**. In:  
 1584 *Proceedings, 48th Rencontres de Moriond on Electroweak Interactions and Unified Theories:  
 1585 La Thuile, Italy, March 2-9, 2013*. 2013, pp. 3–16. arXiv: [1303.6154 \[hep-ph\]](https://arxiv.org/abs/1303.6154). URL:  
 1586 <https://inspirehep.net/record/1225307/files/arXiv:1303.6154.pdf> (see p. 5).
- 1587 [16] PATRICK KOPPENBURG and SEBASTIEN DESCOTES-GENON: **The CKM Parameters**. In:  
 1588 (2017). arXiv: [1702.08834 \[hep-ex\]](https://arxiv.org/abs/1702.08834) (see p. 6).
- 1589 [17] J. A. AGUILAR-SAAVEDRA: **Top flavor-changing neutral interactions: Theoretical  
 1590 expectations and experimental detection**. In: *Acta Phys. Polon.*, **B35**: (2004),  
 1591 pp. 2695–2710. arXiv: [hep-ph/0409342 \[hep-ph\]](https://arxiv.org/abs/hep-ph/0409342) (see pp. 6, 15–17).
- 1592 [18] S. ABACHI et al.: **Observation of the top quark**. In: *Phys. Rev. Lett.*, **74**: (1995),  
 1593 pp. 2632–2637. doi: [10.1103/PhysRevLett.74.2632](https://doi.org/10.1103/PhysRevLett.74.2632). arXiv: [hep-ex/9503003 \[hep-ex\]](https://arxiv.org/abs/hep-ex/9503003)  
 1594 (see p. 6).
- 1595 [19] F. ABE et al.: **Observation of top quark production in  $\bar{p}p$  collisions**. In: *Phys. Rev.  
 1596 Lett.*, **74**: (1995), pp. 2626–2631. doi: [10.1103/PhysRevLett.74.2626](https://doi.org/10.1103/PhysRevLett.74.2626). arXiv: [hep-ex/9503002 \[hep-ex\]](https://arxiv.org/abs/hep-ex/9503002) (see p. 6).
- 1597 [20] LHCTOP WORKING GROUP: **LHCTopWG Summary plots**. Sept. 2017. URL: <https://twiki.cern.ch/twiki/bin/view/LHCPhysics/LHCTopWGSummaryPlots> (see pp. 8, 21).
- 1598 [21] ANDREA GIAMMANCO and JEANNINE WAGNER-KUHR: **Measurement of the t-channel  
 1601 single Top-quark production rates in pp collisions at 7 TeV**. Sept. 2011. URL: <http://cms.web.cern.ch/news/measurement-t-channel-single-top-quark-production-rates-pp-collisions-7-tev> (see p. 9).
- 1602 [22] LHCTOP WORKING GROUP: **ATLAS-CMS recommended predictions for single top  
 1603 cross sections using the Hathor v2.1 program**. Sept. 2017. URL: [https://twiki.cern.ch/twiki/bin/view/LHCPhysics/SingleTopRefXsec#Predictions\\_at\\_7\\_8\\_13\\_and\\_14\\_TeV](https://twiki.cern.ch/twiki/bin/view/LHCPhysics/SingleTopRefXsec#Predictions_at_7_8_13_and_14_TeV) (see p. 9).
- 1604 [23] CMS COLLABORATION: **Summaries of CMS cross section measurements**. Oct. 2017.  
 1605 URL: <https://twiki.cern.ch/twiki/bin/view/CMSPublic/PhysicsResultsCombined> (see pp. 10, 20, 22, 50).
- 1606 [24] CÉLINE DEGRANDE: **Effective field theories in the Standard Model and beyond**.  
 1607 Thesis. Université Catholique de Louvain, Sept. 2011. URL: <https://cp3.irmp.ucl.ac.be/upload/theses/phd/degrande.pdf> (see pp. 10–11).
- 1608 [25] ENRICO FERMI: **Tentativo di una Teoria Dei Raggi  $\beta$** . In: *Il Nuovo Cimento (1924-1942)*, **11**:1 (Sept. 20, 2008), p. 1. doi: [10.1007/BF02959820](https://doi.org/10.1007/BF02959820) (see p. 10).

- 1617 [26] B. GRZADKOWSKI, M. ISKRZYNSKI, M. MISIAK, and J. ROSIEK: **Dimension-Six Terms**  
 1618 **in the Standard Model Lagrangian.** In: *JHEP*, **1010**: (2010), p. 085. doi: [10.1007/JHEP10\(2010\)085](https://doi.org/10.1007/JHEP10(2010)085). arXiv: [1008.4884 \[hep-ph\]](https://arxiv.org/abs/1008.4884) (see pp. 12–13, 16).
- 1620 [27] J.A. AGUILAR SAVVEDRA, C. DEGRANDE, G. DURIEUX, et al.: **Constraining the MSMEFT**  
 1621 **in the top sector at the LHC.** Working document for the TOP LHC WG. June 2017.  
 1622 URL: [http://www.desy.de/~durieux/topbasis/basis\\_note.pdf](http://www.desy.de/~durieux/topbasis/basis_note.pdf) (see p. 12).
- 1623 [28] ANDY BUCKLEY, CHRISTOPH ENGLERT, JAMES FERRANDO, et al.: **Constraining top**  
 1624 **quark effective theory in the LHC Run II era.** In: *JHEP*, **04**: (2016), p. 015. doi:  
 1625 [10.1007/JHEP04\(2016\)015](https://doi.org/10.1007/JHEP04(2016)015). arXiv: [1512.03360 \[hep-ph\]](https://arxiv.org/abs/1512.03360) (see p. 13).
- 1626 [29] YORIKIYO NAGASHIMA: **Beyond the standard model of elementary particle physics.**  
 1627 Weinheim, Germany: Wiley-VCH Verlag, 2014. URL: [http://www-spires.fnal.gov/  
 1628 spires/find/books/www?cl=QC793.2.N34::2014](http://www-spires.fnal.gov/spires/find/books/www?cl=QC793.2.N34::2014) (see p. 14).
- 1629 [30] P. A. R. ADE et al.: **Planck 2015 results. XIII. Cosmological parameters.** In: *Astron.*  
 1630 *Astrophys.*, **594**: (2016), A13. doi: [10.1051/0004-6361/201525830](https://doi.org/10.1051/0004-6361/201525830). arXiv: [1502.01589  
 1631 \[astro-ph.CO\]](https://arxiv.org/abs/1502.01589) (see p. 14).
- 1632 [31] P. J. E. PEEBLES and BHARAT RATRA: **The Cosmological constant and dark energy.**  
 1633 In: *Rev. Mod. Phys.*, **75**: (2003), pp. 559–606. doi: [10.1103/RevModPhys.75.559](https://doi.org/10.1103/RevModPhys.75.559). arXiv:  
 1634 [astro-ph/0207347 \[astro-ph\]](https://arxiv.org/abs/astro-ph/0207347) (see p. 14).
- 1635 [32] A. D. SAKHAROV: **Violation of CP Invariance, c Asymmetry, and Baryon Asym-**  
 1636 **metry of the Universe.** In: *Pisma Zh. Eksp. Teor. Fiz.*, **5**: (1967). [*Usp. Fiz.*  
 1637 *Nauk* **161**, 61(1991)], pp. 32–35. doi: [10.1070/PU1991v034n05ABEH002497](https://doi.org/10.1070/PU1991v034n05ABEH002497) (see p. 14).
- 1638 [33] GUSTAVO BURDMAN: **New solutions to the hierarchy problem.** In: *Braz. J. Phys.*, **37**:  
 1639 (2007), pp. 506–513. doi: [10.1590/S0103-97332007000400006](https://doi.org/10.1590/S0103-97332007000400006). arXiv: [hep-ph/0703194  
 1640 \[hep-ph\]](https://arxiv.org/abs/hep-ph/0703194) (see p. 14).
- 1641 [34] T. ET AL. AALTONEN: **Search for the Flavor-Changing Neutral-Current Decay  $t \rightarrow Zq$**   
 1642 **in  $p\bar{p}$  Collisions at  $\sqrt{s} = 1.96$  TeV.** In: *Phys. Rev. Lett.*, **101**: (19 Nov. 2008),  
 1643 p. 192002. doi: [10.1103/PhysRevLett.101.192002](https://doi.org/10.1103/PhysRevLett.101.192002) (see p. 15).
- 1644 [35] VICTOR MUKHAMEDOVICH ABAZOV et al.: **Search for flavour changing neutral cur-**  
 1645 **rents via quark-gluon couplings in single top quark production using  $2.3 \text{ fb}^{-1}$  of**  
 1646  **$p\bar{p}$  collisions.** In: *Phys. Lett.*, **B693**: (2010), pp. 81–87. doi: [10.1016/j.physletb.2010.08.011](https://doi.org/10.1016/j.physletb.2010.08.011). arXiv: [1006.3575 \[hep-ex\]](https://arxiv.org/abs/1006.3575) (see p. 15).
- 1648 [36] GEORGES AAD et al.: **Search for flavour-changing neutral current top-quark decays**  
 1649 **to  $qZ$  in  $pp$  collision data collected with the ATLAS detector at  $\sqrt{s} = 8$  TeV.** In: *Eur. Phys. J.*, **C76**:1 (2016), p. 12. doi: [10.1140/epjc/s10052-015-3851-5](https://doi.org/10.1140/epjc/s10052-015-3851-5). arXiv:  
 1651 [1508.05796 \[hep-ex\]](https://arxiv.org/abs/1508.05796) (see p. 15).
- 1652 [37] GEORGES AAD et al.: **Search for single top-quark production via flavour-changing**  
 1653 **neutral currents at 8 TeV with the ATLAS detector.** In: *Eur. Phys. J.*, **C76**:2 (2016),  
 1654 p. 55. doi: [10.1140/epjc/s10052-016-3876-4](https://doi.org/10.1140/epjc/s10052-016-3876-4). arXiv: [1509.00294 \[hep-ex\]](https://arxiv.org/abs/1509.00294) (see pp. 15,  
 1655 19).
- 1656 [38] GEORGES AAD et al.: **Search for flavour-changing neutral current top quark decays**  
 1657  **$t \rightarrow Hq$  in  $pp$  collisions at  $\sqrt{s} = 8$  TeV with the ATLAS detector.** In: *JHEP*, **12**:  
 1658 (2015), p. 061. doi: [10.1007/JHEP12\(2015\)061](https://doi.org/10.1007/JHEP12(2015)061). arXiv: [1509.06047 \[hep-ex\]](https://arxiv.org/abs/1509.06047) (see  
 1659 p. 15).

- 1660 [39] MORAD AABOUD et al.: **Search for top quark decays  $t \rightarrow qH$ , with  $H \rightarrow \gamma\gamma$ , in**
- 1661  $\sqrt{s} = 13$  TeV  $pp$  collisions using the ATLAS detector. In: (2017). arXiv: [1707.01404](https://arxiv.org/abs/1707.01404) [hep-ex] (see pp. 15, 19).
- 1663 [40] **Search for flavour-changing neutral current top quark decays  $t \rightarrow qZ$  in proton-**
- 1664 **proton collisions at  $\sqrt{s} = 13$  TeV with the ATLAS Detector.** Tech. rep. ATLAS-CONF-
- 1665 2017-070. Geneva: CERN, Sept. 2017. URL: <https://cds.cern.ch/record/2285808>
- 1666 (see pp. 15, 19).
- 1667 [41] ALBERT M SIRUNYAN et al.: **Search for associated production of a Z boson with a**
- 1668 **single top quark and for tZ flavour-changing interactions in pp collisions at  $\sqrt{s}$**
- 1669 **= 8 TeV.** In: (2017). arXiv: [1702.01404](https://arxiv.org/abs/1702.01404) [hep-ex] (see pp. 15, 19).
- 1670 [42] SERGUEI CHATRCHYAN et al.: **Search for Flavor-Changing Neutral Currents in Top-**
- 1671 **Quark Decays  $t \rightarrow Zq$  in pp Collisions at  $\sqrt{s} = 8$ TeV.** In: *Phys. Rev. Lett.*, **112**:17
- 1672 (2014), p. 171802. doi: [10.1103/PhysRevLett.112.171802](https://doi.org/10.1103/PhysRevLett.112.171802). arXiv: [1312.4194](https://arxiv.org/abs/1312.4194) [hep-ex]
- 1673 (see p. 15).
- 1674 [43] VARDAN KHACHATRYAN et al.: **Search for anomalous single top quark production in**
- 1675 **association with a photon in pp collisions at  $\sqrt{s} = 8$  TeV.** In: *JHEP*, **04**: (2016),
- 1676 p. 035. doi: [10.1007/JHEP04\(2016\)035](https://doi.org/10.1007/JHEP04(2016)035). arXiv: [1511.03951](https://arxiv.org/abs/1511.03951) [hep-ex] (see pp. 15, 19).
- 1677 [44] VARDAN KHACHATRYAN et al.: **Search for top quark decays via Higgs-boson-mediated**
- 1678 **flavor-changing neutral currents in pp collisions at  $\sqrt{s} = 8$  TeV.** In: *JHEP*, **02**:
- 1679 (2017), p. 079. doi: [10.1007/JHEP02\(2017\)079](https://doi.org/10.1007/JHEP02(2017)079). arXiv: [1610.04857](https://arxiv.org/abs/1610.04857) [hep-ex] (see
- 1680 p. 15).
- 1681 [45] **Search for the flavor-changing interactions of the top quark with the Higgs boson**
- 1682 **in  $H \rightarrow b\bar{b}$  channel at  $\sqrt{s} = 13$  TeV.** Tech. rep. CMS-PAS-TOP-17-003. Geneva:
- 1683 CERN, 2017. URL: <https://cds.cern.ch/record/2284743> (see p. 15).
- 1684 [46] M. BENEKE et al.: **Top quark physics.** In: *1999 CERN Workshop on standard model*
- 1685 *physics (and more) at the LHC, CERN, Geneva, Switzerland, 25-26 May: Proceedings.*
- 1686 2000, pp. 419–529. arXiv: [hep-ph/0003033](https://arxiv.org/abs/hep-ph/0003033) [hep-ph]. URL: <http://weblib.cern.ch/abstract?CERN-TH-2000-100> (see p. 17).
- 1688 [47] JUN GAO, CHONG SHENG LI, and HUA XING ZHU: **Top Quark Decay at Next-to-Next-**
- 1689 **to Leading Order in QCD.** In: *Phys. Rev. Lett.*, **110**:4 (2013), p. 042001. doi:
- 1690 [10.1103/PhysRevLett.110.042001](https://doi.org/10.1103/PhysRevLett.110.042001). arXiv: [1210.2808](https://arxiv.org/abs/1210.2808) [hep-ph] (see pp. 18, 47).
- 1691 [48] STEPHEN MYERS: **The LEP Collider, from design to approval and commissioning.**
- 1692 John Adams' Lecture. Delivered at CERN, 26 Nov 1990. Geneva: CERN, 1991. URL:
- 1693 [http://cds.cern.ch/record/226776](https://cds.cern.ch/record/226776) (see p. 23).
- 1694 [49] STEPHEN HOLMES, RONALD S MOORE, and VLADIMIR SHILTSEV: **Overview of the**
- 1695 **Tevatron collider complex: goals, operations and performance.** In: *Journal of In-*
- 1696 *strumentation*, **6**:08 (2011), T08001. URL: <http://stacks.iop.org/1748-0221/6/i=08/a=T08001> (see p. 23).
- 1698 [50] R. BARATE et al.: **Search for the standard model Higgs boson at LEP.** In: *Phys.*
- 1699 *Lett.*, **B565**: (2003), pp. 61–75. doi: [10.1016/S0370-2693\(03\)00614-2](https://doi.org/10.1016/S0370-2693(03)00614-2). arXiv: [hep-ex/0306033](https://arxiv.org/abs/hep-ex/0306033) [hep-ex] (see p. 23).

- 1701 [51] KENNETH HERNER: **Higgs Boson Studies at the Tevatron**. In: *Nucl. Part. Phys. Proc.*,  
1702 273-275: (2016), pp. 852–856. doi: [10.1016/j.nuclphysbps.2015.09.131](https://doi.org/10.1016/j.nuclphysbps.2015.09.131) (see p. 23).
- 1703 [52] ABDELHAK DJOUADI: **The Anatomy of electro-weak symmetry breaking. I: The  
1704 Higgs boson in the standard model**. In: *Phys. Rept.*, 457: (2008), pp. 1–216. doi:  
1705 [10.1016/j.physrep.2007.10.004](https://doi.org/10.1016/j.physrep.2007.10.004). arXiv: [hep-ph/0503172 \[hep-ph\]](https://arxiv.org/abs/hep-ph/0503172) (see p. 23).
- 1706 [53] LYNDON EVANS and PHILIP BRYANT: **LHC Machine**. In: *Journal of Instrumentation*,  
1707 3:08 (2008), S08001. url: <http://stacks.iop.org/1748-0221/3/i=08/a=S08001> (see  
1708 p. 23).
- 1709 [54] THOMAS SVEN PETTERSSON and P LEFÈVRE: **The Large Hadron Collider: conceptual  
1710 design**. Tech. rep. CERN-AC-95-05-LHC. Oct. 1995, p. 20 and 22. URL: <https://cds.cern.ch/record/291782> (see p. 23).
- 1712 [55] JORG WENNINGER and EZIO TODESCO: **Large Hadron Collider momentum calibration  
1713 and accuracy**. Tech. rep. CERN-ACC-2017-0007. Geneva: CERN, Feb. 2017. URL:  
1714 <https://cds.cern.ch/record/2254678> (see p. 24).
- 1715 [56] CINZIA DE MELIS: **The CERN accelerator complex. Complexe des accélérateurs du  
1716 CERN**. In: (July 2016). General Photo. URL: <https://cds.cern.ch/record/2197559>  
1717 (see p. 24).
- 1718 [57] ANTONELLA DEL ROSSO: **HL-LHC updates in Japan. Projet HL-LHC : une réunion  
1719 fait le point au Japon**. In: BUL-NA-2014-272. 51/2014 (Dec. 2014), p. 4. URL:  
1720 <https://cds.cern.ch/record/1975962> (see p. 25).
- 1721 [58] OLIVER SIM BRÜNING, PAUL COLLIER, P LEBRUN, et al.: **LHC Design Report**. CERN  
1722 Yellow Reports: Monographs. Geneva: CERN, 2004. URL: <https://cds.cern.ch/record/782076> (see p. 25).
- 1724 [59] G. AAD et al.: **The ATLAS Experiment at the CERN Large Hadron Collider**. In: *JINST*,  
1725 3: (2008), S08003. doi: [10.1088/1748-0221/3/08/S08003](https://doi.org/10.1088/1748-0221/3/08/S08003) (see p. 25).
- 1726 [60] S. CHATRHYAN et al.: **The CMS Experiment at the CERN LHC**. In: *JINST*, 3: (2008),  
1727 S08004. doi: [10.1088/1748-0221/3/08/S08004](https://doi.org/10.1088/1748-0221/3/08/S08004) (see pp. 25, 33–35).
- 1728 [61] K. AAMODT et al.: **The ALICE experiment at the CERN LHC**. In: *JINST*, 3: (2008),  
1729 S08002. doi: [10.1088/1748-0221/3/08/S08002](https://doi.org/10.1088/1748-0221/3/08/S08002) (see p. 25).
- 1730 [62] A. AUGUSTO ALVES JR. et al.: **The LHCb Detector at the LHC**. In: *JINST*, 3: (2008),  
1731 S08005. doi: [10.1088/1748-0221/3/08/S08005](https://doi.org/10.1088/1748-0221/3/08/S08005) (see p. 25).
- 1732 [63] M. BONGI et al.: **Astroparticle physics at LHC: The LHCf experiment ready for data  
1733 taking**. In: *Nucl. Instrum. Meth.*, A612: (2010), pp. 451–454. doi: [10.1016/j.nima.2009.08.039](https://doi.org/10.1016/j.nima.2009.08.039) (see p. 26).
- 1735 [64] G. ANELLI et al.: **The TOTEM experiment at the CERN Large Hadron Collider**. In:  
1736 *JINST*, 3: (2008), S08007. doi: [10.1088/1748-0221/3/08/S08007](https://doi.org/10.1088/1748-0221/3/08/S08007) (see p. 26).
- 1737 [65] B. ACHARYA et al.: **The Physics Programme Of The MoEDAL Experiment At The LHC**.  
1738 In: *Int. J. Mod. Phys.*, A29: (2014), p. 1430050. doi: [10.1142/S0217751X14300506](https://doi.org/10.1142/S0217751X14300506).  
1739 arXiv: [1405.7662 \[hep-ph\]](https://arxiv.org/abs/1405.7662) (see p. 26).
- 1740 [66] BY JAMES GILLIES: **Luminosity? Why don't we just say collision rate?** In: (Mar.  
1741 2011). URL: [http://cds.cern.ch/record/1997001](https://cds.cern.ch/record/1997001) (see p. 26).

- 1742 [67] BY HARRIET JARLETT and HARRIET KIM JARLETT: **LHC pushes limits of performance.**  
 1743 In: (Aug. 2016). URL: <http://cds.cern.ch/record/2212301> (see p. 26).
- 1744 [68] CMS COLLABORATION. Okt 2017. URL: [https://twiki.cern.ch/twiki/bin/view/CMSPublic/LumiPublicResults#Online\\_Luminosity\\_AN2](https://twiki.cern.ch/twiki/bin/view/CMSPublic/LumiPublicResults#Online_Luminosity_AN2) (see p. 27).
- 1746 [69] **Technical proposal.** LHC Tech. Proposal. Cover title : CMS, the Compact Muon  
 1747 Solenoid : technical proposal. Geneva: CERN, 1994. URL: <https://cds.cern.ch/record/290969> (see p. 27).
- 1749 [70] G. L. BAYATIAN et al.: **CMS physics: Technical design report.** In: (2006) (see p. 27).
- 1750 [71] G L BAYATIAN, S CHATRCHYAN, G HMAYAKYAN, et al.: **CMS Physics: Technical Design**  
 1751 **Report Volume 1: Detector Performance and Software.** Technical Design Report  
 1752 CMS. There is an error on cover due to a technical problem for some items. Geneva:  
 1753 CERN, 2006. URL: <https://cds.cern.ch/record/922757> (see pp. 27, 32, 57).
- 1754 [72] CMS COLLABORATION: **Detector Drawings.** CMS Collection. Mar. 2012. URL: <https://cds.cern.ch/record/1433717> (see p. 28).
- 1756 [73] S CHATRCHYAN, V KHACHATRYAN, A M SIRUNYAN, et al.: **Performance of the CMS Drift**  
 1757 **Tube Chambers with Cosmic Rays.** In: *J. Instrum.*, 5:arXiv:0911.4855. CMS-CFT-  
 1758 09-012 (Nov. 2009), T03015 . 47 p. URL: <http://cds.cern.ch/record/1223944> (see  
 1759 pp. 30–31).
- 1760 [74] TOM DODINGTON: **News from the CMS experimental site: 22 November 2013.** Nov.  
 1761 2013. URL: <http://cms.web.cern.ch/news/news-point-5-22-november-2013> (see  
 1762 p. 31).
- 1763 [75] INSTITUTE OF RESEARCH INTO THE FUNDAMENTAL LAWS THE UNIVERSE: **The CMS**  
 1764 **detector superconducting solenoid.** Jan. 2006. URL: [http://irfu.cea.fr/en/Phoebe/Vie\\_des\\_labos/Ast/ast\\_visu.php?id\\_ast=839](http://irfu.cea.fr/en/Phoebe/Vie_des_labos/Ast/ast_visu.php?id_ast=839) (see p. 33).
- 1766 [76] FERGUS WILSON: **Experimental Particle Physics.** Apr. 2012. URL: <http://slideplayer.com/slide/794631/> (see p. 33).
- 1768 [77] EMRAH TIRAS, BURAK BILKI, and YASAR ONEL: **Commissioning of CMS Forward**  
 1769 **Hadron Calorimeters with Upgraded Multi-anode PMTs and μTCA Readout.** In:  
 1770 (2016). arXiv: 1611.05232 [physics.ins-det] (see p. 34).
- 1771 [78] LUCAS TAYLOR: **Experimental Particle Physics.** Nov. 2011. URL: <http://cms.web.cern.ch/news/electromagnetic-calorimeter> (see p. 34).
- 1773 [79] **Proceedings, 34th International Conference on High Energy Physics (ICHEP 2008)**  
 1774 URL: <http://www.slac.stanford.edu/econf/C080730> (see p. 34).
- 1775 [80] L. BRIANZA: **Precision crystal calorimetry in LHC Run II with the CMS ECAL.** In:  
 1776 *Journal of Instrumentation*, 12:01 (2017), p. C01069. URL: <http://stacks.iop.org/1748-0221/12/i=01/a=C01069> (see pp. 35, 38).
- 1778 [81] SERGUEI CHATRCHYAN, KHACHATRYAN, et al.: **Description and performance of track**  
 1779 **and primary-vertex reconstruction with the CMS tracker.** In: *J. Instrum.*, 9:arXiv:1405.6569  
 1780 CERN-PH-EP-2014-070. CMS-TRK-11-001 (May 2014). Comments: Replaced with  
 1781 published version. Added journal reference and DOI, P10009. 80 p. URL: <http://cds.cern.ch/record/1704291> (see pp. 35, 58).

- 1783 [82] BY CHRISTINE SUTTON: **Chronicles of CMS: the saga of LS1**. In: (May 2015). URL:  
1784 <http://cds.cern.ch/record/2024986> (see p. 36).
- 1785 [83] **A beautiful barrel for CMS**. In: (Mar. 2014). URL: <http://cds.cern.ch/record/1998635> (see p. 36).
- 1787 [84] VARDAN KHACHATRYAN et al.: **The CMS trigger system**. In: *JINST*, **12**:01 (2017),  
1788 P01020. DOI: [10.1088/1748-0221/12/01/P01020](https://doi.org/10.1088/1748-0221/12/01/P01020). arXiv: [1609.02366 \[physics.ins-det\]](https://arxiv.org/abs/1609.02366) (see p. 37).
- 1790 [85] BY CORINNE PRALAVORIO and CORINNE PRALAVORIO: **Major work to ready the LHC  
1791 experiments for Run 2**. In: (May 2015). URL: <http://cds.cern.ch/record/2024977> (see p. 37).
- 1793 [86] LUIGI GUIDUCCI: **CMS muon system towards LHC Run 2 and beyond**. Tech. rep.  
1794 CMS-CR-2014-333. Geneva: CERN, Oct. 2014. URL: <https://cds.cern.ch/record/1966038> (see p. 38).
- 1796 [87] CARLO BATTILANA: **The CMS muon system status and upgrades for LHC run-2 and  
1797 performance of muon reconstruction with 13 TeV data**. Tech. rep. CMS-CR-2016-  
1798 437. Geneva: CERN, Dec. 2016. URL: <http://cds.cern.ch/record/2239185> (see  
1799 p. 38).
- 1800 [88] SERGUEI CHATRCHYAN et al.: **Energy Calibration and Resolution of the CMS Elec-  
1801 tronagnetic Calorimeter in  $pp$  Collisions at  $\sqrt{s} = 7$  TeV**. In: *JINST*, **8**: (2013).  
1802 [*JINST8,9009(2013)*], P09009. DOI: [10.1088/1748-0221/8/09/P09009](https://doi.org/10.1088/1748-0221/8/09/P09009). arXiv: [1306.2016 \[hep-ex\]](https://arxiv.org/abs/1306.2016) (see p. 38).
- 1804 [89] **Cool running for CMS tracker**. In: (Mar. 2014). URL: <http://cds.cern.ch/record/1998606> (see p. 38).
- 1806 [90] L. CADAMURO: **The CMS Level-1 trigger system for LHC Run II**. In: *Journal of  
1807 Instrumentation*, **12**:03 (2017), p. C03021. URL: <http://stacks.iop.org/1748-0221/12/i=03/a=C03021> (see p. 38).
- 1809 [91] DAVID AARON MATZNER DOMINGUEZ, D. ABBANEO, K. ARNDT, et al.: **CMS Technical  
1810 Design Report for the Pixel Detector Upgrade**. In: (2012) (see p. 39).
- 1811 [92] HANNO CHRISTOPHER PERREY: **Plans and Status of the Phase I Upgrade of the  
1812 CMS Pixel Tracker**. Tech. rep. CMS-CR-2014-005. Geneva: CERN, Jan. 2014. URL:  
1813 <http://cds.cern.ch/record/1644757> (see p. 39).
- 1814 [93] CLAUDIO GRANDI, DAVID STICKLAND, LUCAS TAYLOR, ACHILLE PETRILLI, and ALAIN  
1815 HERVÉ: **CMS Computing Model: The "CMS Computing Model RTAG"**. Tech. rep.  
1816 CMS-NOTE-2004-031. CERN-LHCC-2004-035. LHCC-G-083. Geneva: CERN, Dec.  
1817 2004. URL: <http://cds.cern.ch/record/814248> (see p. 39).
- 1818 [94] CHRISTOPH ECK, J KNOBLOCH, LESLIE ROBERTSON, et al.: **LHC computing Grid: Tech-  
1819 nical Design Report. Version 1.06 (20 Jun 2005)**. Technical Design Report LCG.  
1820 Geneva: CERN, 2005. URL: <https://cds.cern.ch/record/840543> (see p. 39).
- 1821 [95] WORLDWIDE LHC COMPUTING GRID: **WorldWide LHC Computing Gird - 2017**. Oct.  
1822 2017. URL: <http://wlcg-public.web.cern.ch> (see p. 40).

- 1823 [96] JOHN C. COLLINS, DAVISON E. SOPER, and GEORGE F. STERMAN: **Factorization of Hard**
- 1824 **Processes in QCD.** In: *Adv. Ser. Direct. High Energy Phys.*, **5**: (1989), pp. 1–91. doi:
- 1825 [10.1142/9789814503266\\_0001](https://doi.org/10.1142/9789814503266_0001). arXiv: [hep-ph/0409313](https://arxiv.org/abs/hep-ph/0409313) [hep-ph] (see p. 41).
- 1826 [97] RINGAILE PLACAKYTE: **Parton Distribution Functions.** In: *Proceedings, 31st International Conference on Physics in collisions (PIC 2011): Vancouver, Canada, August 28–September 1, 2011.* 2011. arXiv: [1111.5452](https://arxiv.org/abs/1111.5452) [hep-ph]. URL: <https://inspirehep.net/record/954990/files/arXiv:1111.5452.pdf> (see p. 41).
- 1830 [98] RICHARD D. BALL, VALERIO BERTONE, STEFANO CARRAZZA, et al.: **Parton distributions**
- 1831 **for the LHC run II.** In: *Journal of High Energy Physics*, **2015**:4 (2015), p. 40. doi:
- 1832 [10.1007/JHEP04\(2015\)040](https://doi.org/10.1007/JHEP04(2015)040) (see p. 41).
- 1833 [99] JON BUTTERWORTH et al.: **PDF4LHC recommendations for LHC Run II.** In: *J. Phys.*,  
1834 **G43**: (2016), p. 023001. doi: [10.1088/0954-3899/43/2/023001](https://doi.org/10.1088/0954-3899/43/2/023001). arXiv: [1510.03865](https://arxiv.org/abs/1510.03865)  
1835 [hep-ph] (see pp. 41–42).
- 1836 [100] H. ABRAMOWICZ and A. CALDWELL: **HERA collider physics.** In: *Rev. Mod. Phys.*, **71**:  
1837 (1999), pp. 1275–1410. doi: [10.1103/RevModPhys.71.1275](https://doi.org/10.1103/RevModPhys.71.1275). arXiv: [hep-ex/9903037](https://arxiv.org/abs/hep-ex/9903037)  
1838 [hep-ex] (see p. 42).
- 1839 [101] STEPHEN HOLMES, RONALD S. MOORE, and VLADIMIR SHILTSEV: **Overview of the Tevatron Collider Complex: Goals, Operations and Performance.** In: *JINST*, **6**: (2011),  
1840 T08001. doi: [10.1088/1748-0221/6/08/T08001](https://doi.org/10.1088/1748-0221/6/08/T08001). arXiv: [1106.0909](https://arxiv.org/abs/1106.0909) [physics.acc-ph]  
1841 (see p. 42).
- 1843 [102] JUAN ROJO et al.: **The PDF4LHC report on PDFs and LHC data: Results from Run I**  
1844 **and preparation for Run II.** In: *J. Phys.*, **G42**: (2015), p. 103103. doi: [10.1088/0954-3899/42/10/103103](https://doi.org/10.1088/0954-3899/42/10/103103). arXiv: [1507.00556](https://arxiv.org/abs/1507.00556) [hep-ph] (see p. 42).
- 1846 [103] ALAN D. MARTIN: **Proton structure, Partons, QCD, DGLAP and beyond.** In: *Acta Phys. Polon.*, **B39**: (2008), pp. 2025–2062. arXiv: [0802.0161](https://arxiv.org/abs/0802.0161) [hep-ph] (see p. 42).
- 1848 [104] J. PUMPLIN, D. STUMP, R. BROCK, et al.: **Uncertainties of predictions from parton distribution functions. 2. The Hessian method.** In: *Phys. Rev.*, **D65**: (2001), p. 014013.  
1849 doi: [10.1103/PhysRevD.65.014013](https://doi.org/10.1103/PhysRevD.65.014013). arXiv: [hep-ph/0101032](https://arxiv.org/abs/hep-ph/0101032) [hep-ph] (see p. 42).
- 1851 [105] FRANZ MANDL and GRAHAM G SHAW: **Quantum field theory; 2nd ed.** New York, NY:  
1852 Wiley, 2010. URL: <https://cds.cern.ch/record/1236742> (see p. 44).
- 1853 [106] S BANERJEE: **CMS Simulation Software.** In: *Journal of Physics: Conference Series*,  
1854 **396**:2 (2012), p. 022003. URL: <http://stacks.iop.org/1742-6596/396/i=2/a=022003>  
1855 (see p. 44).
- 1856 [107] M HILDRETH, V N IVANCHENKO, D J LANGE, and M J KORTELAINEN: **CMS Full Simu-**  
1857 **lation for Run-2.** In: *Journal of Physics: Conference Series*, **664**:7 (2015), p. 072022.  
1858 URL: <http://stacks.iop.org/1742-6596/664/i=7/a=072022> (see p. 44).
- 1859 [108] S. AGOSTINELLI, J. ALLISON, K. AMAKO, et al.: **Geant4-a simulation toolkit.** In: *Nuclear*  
1860 *Instruments and Methods in Physics Research Section A: Accelerators, Spectrometers,*  
1861 *Detectors and Associated Equipment*, **506**:3 (2003), pp. 250–303. doi: [https://doi.org/10.1016/S0168-9002\(03\)01368-8](https://doi.org/10.1016/S0168-9002(03)01368-8) (see pp. 44, 46).

- 1863 [109] MICHAEL H. SEYMOUR and MARILYN MARX: **Monte Carlo Event Generators**. In: *Proceedings, 69th Scottish Universities Summer School in Physics : LHC Phenomenology (SUSSP69): St.Andrews, Scotland, August 19-September 1, 2012.* 2013, pp. 287–319. DOI: [10.1007/978-3-319-05362-2\\_8](https://doi.org/10.1007/978-3-319-05362-2_8). arXiv: [1304.6677 \[hep-ph\]](https://arxiv.org/abs/1304.6677) (see p. 44).
- 1864  
1865  
1866
- 1867 [110] TORBJORN SJÖSTRAND: **Monte Carlo Tools**. In: *Proceedings, 65th Scottish Universities Summer School in Physics: LHC Physics (SUSSP65): St. Andrews, UK, August 16-29, 2009.* 2009, pp. 309–339. DOI: [10.1201/b11865-14](https://doi.org/10.1201/b11865-14). arXiv: [0911.5286 \[hep-ph\]](https://arxiv.org/abs/0911.5286) (see p. 44).
- 1868  
1869  
1870
- 1871 [111] STEFAN HÖCHE: **Introduction to parton-shower event generators**. In: *Proceedings, Theoretical Advanced Study Institute in Elementary Particle Physics: Journeys Through the Precision Frontier: Amplitudes for Colliders (TASI 2014): Boulder, Colorado, June 2-27, 2014.* 2015, pp. 235–295. DOI: [10.1142/9789814678766\\_0005](https://doi.org/10.1142/9789814678766_0005). arXiv: [1411.4085 \[hep-ph\]](https://arxiv.org/abs/1411.4085) (see pp. 44–45).
- 1872  
1873  
1874  
1875
- 1876 [112] ADAM ALLOUL, NEIL D. CHRISTENSEN, CÉLINE DEGRANDE, CLAUDE DUHR, and BENJAMIN FUKS: **FeynRules 2.0 - A complete toolbox for tree-level phenomenology**. In: *Comput. Phys. Commun.*, **185**: (2014), pp. 2250–2300. DOI: [10.1016/j.cpc.2014.04.012](https://doi.org/10.1016/j.cpc.2014.04.012). arXiv: [1310.1921 \[hep-ph\]](https://arxiv.org/abs/1310.1921) (see p. 44).
- 1878  
1879
- 1880 [113] CELINE DEGRANDE, CLAUDE DUHR, BENJAMIN FUKS, et al.: **UFO - The Universal FeynRules Output**. In: *Comput. Phys. Commun.*, **183**: (2012), pp. 1201–1214. DOI: [10.1016/j.cpc.2012.01.022](https://doi.org/10.1016/j.cpc.2012.01.022). arXiv: [1108.2040 \[hep-ph\]](https://arxiv.org/abs/1108.2040) (see p. 44).
- 1884  
1885
- 1886 [114] JOHAN ALWALL, MICHEL HERQUET, FABIO MALTONI, OLIVIER MATTELAER, and TIM STELZER: **MadGraph 5 : Going Beyond**. In: *JHEP*, **06**: (2011), p. 128. DOI: [10.1007/JHEP06\(2011\)128](https://doi.org/10.1007/JHEP06(2011)128). arXiv: [1106.0522 \[hep-ph\]](https://arxiv.org/abs/1106.0522) (see pp. 45, 48).
- 1887  
1888  
1889
- 1890 [115] MICHELANGELO L. MANGANO, MAURO MORETTI, FULVIO PICCININI, and MICHELE TREC-CANI: **Matching matrix elements and shower evolution for top-quark production in hadronic collisions**. In: *JHEP*, **01**: (2007), p. 013. DOI: [10.1088/1126-6708/2007/01/013](https://doi.org/10.1088/1126-6708/2007/01/013). arXiv: [hep-ph/0611129 \[hep-ph\]](https://arxiv.org/abs/hep-ph/0611129) (see p. 45).
- 1891  
1892
- 1893 [116] TORBJORN SJOSTRAND, STEFAN ASK, JESPER R. CHRISTIANSEN, et al.: **An introduction to {PYTHIA} 8.2**. In: *Computer Physics Communications*, **191**: (2015), pp. 159–177. DOI: <http://dx.doi.org/10.1016/j.cpc.2015.01.024> (see pp. 45–46).
- 1894  
1895
- 1896 [117] TORBJORN SJOSTRAND, STEPHEN MRENNA, and PETER Z. SKANDS: **PYTHIA 6.4 Physics and Manual**. In: *JHEP*, **0605**: (2006), p. 026. DOI: [10.1088/1126-6708/2006/05/026](https://doi.org/10.1088/1126-6708/2006/05/026). arXiv: [hep-ph/0603175 \[hep-ph\]](https://arxiv.org/abs/hep-ph/0603175) (see pp. 45–46).
- 1897  
1898
- 1899 [118] TORBJORN SJOSTRAND, STEFAN ASK, JESPER R. CHRISTIANSEN, et al.: **An Introduction to PYTHIA 8.2**. In: *Comput. Phys. Commun.*, **191**: (2015), pp. 159–177. DOI: [10.1016/j.cpc.2015.01.024](https://doi.org/10.1016/j.cpc.2015.01.024). arXiv: [1410.3012 \[hep-ph\]](https://arxiv.org/abs/1410.3012) (see pp. 45–46, 48–49).
- 1900  
1901  
1902
- 1900 [119] JOHAN ALWALL et al.: **Comparative study of various algorithms for the merging of parton showers and matrix elements in hadronic collisions**. In: *Eur. Phys. J.*, **C53**: (2008), pp. 473–500. DOI: [10.1140/epjc/s10052-007-0490-5](https://doi.org/10.1140/epjc/s10052-007-0490-5). arXiv: [0706.2569 \[hep-ph\]](https://arxiv.org/abs/0706.2569) (see pp. 45, 48).

- 1903 [120] J. ALWALL, R. FREDERIX, S. FRIXIONE, et al.: **The automated computation of tree-level**  
 1904 **and next-to-leading order differential cross sections, and their matching to parton**  
 1905 **shower simulations.** In: *JHEP*, **07:** (2014), p. 079. doi: [10.1007/JHEP07\(2014\)079](https://doi.org/10.1007/JHEP07(2014)079).  
 1906 arXiv: [1405.0301](https://arxiv.org/abs/1405.0301) [hep-ph] (see p. 45).
- 1907 [121] STEFANO FRIXIONE and BRYAN R. WEBBER: **Matching NLO QCD computations and**  
 1908 **parton shower simulations.** In: *JHEP*, **06:** (2002), p. 029. doi: [10.1088/1126-6708/2002/06/029](https://doi.org/10.1088/1126-6708/2002/06/029). arXiv: [hep-ph/0204244](https://arxiv.org/abs/hep-ph/0204244) [hep-ph] (see pp. 45, 48).
- 1910 [122] RIKKERT FREDERIX and STEFANO FRIXIONE: **Merging meets matching in MC@NLO.**  
 1911 In: *JHEP*, **12:** (2012), p. 061. doi: [10.1007/JHEP12\(2012\)061](https://doi.org/10.1007/JHEP12(2012)061). arXiv: [1209.6215](https://arxiv.org/abs/1209.6215)  
 1912 [hep-ph] (see p. 45).
- 1913 [123] SIMONE ALIOLI, PAOLO NASON, CARLO OLEARI, and EMANUELE RE: **A general frame-**  
 1914 **work for implementing NLO calculations in shower Monte Carlo programs: the**  
 1915 **POWHEG BOX.** In: *Journal of High Energy Physics*, **2010**:6 (2010), p. 43. doi: [10.1007/JHEP06\(2010\)043](https://doi.org/10.1007/JHEP06(2010)043) (see pp. 45, 48).
- 1917 [124] SIMONE ALIOLI, PAOLO NASON, CARLO OLEARI, and EMANUELE RE: **NLO single-top**  
 1918 **production matched with shower in POWHEG: s - and t -channel contributions.**  
 1919 In: *Journal of High Energy Physics*, **2009**:09 (2009), p. 111. URL: <http://stacks.iop.org/1126-6708/2009/i=09/a=111> (see pp. 45, 48).
- 1921 [125] STEFANO FRIXIONE, PAOLO NASON, and CARLO OLEARI: **Matching NLO QCD com-**  
 1922 **putations with parton shower simulations: the POWHEG method.** In: *Journal of*  
 1923 *High Energy Physics*, **2007**:11 (2007), p. 070. URL: <http://stacks.iop.org/1126-6708/2007/i=11/a=070> (see pp. 45, 48).
- 1925 [126] SIMONE ALIOLI, PAOLO NASON, CARLO OLEARI, and EMANUELE RE: **A general frame-**  
 1926 **work for implementing NLO calculations in shower Monte Carlo programs: the**  
 1927 **POWHEG BOX.** In: *JHEP*, **06:** (2010), p. 043. doi: [10.1007/JHEP06\(2010\)043](https://doi.org/10.1007/JHEP06(2010)043). arXiv:  
 1928 [1002.2581](https://arxiv.org/abs/1002.2581) [hep-ph] (see pp. 45, 48).
- 1929 [127] STEFANO FRIXIONE, PAOLO NASON, and CARLO OLEARI: **Matching NLO QCD com-**  
 1930 **putations with Parton Shower simulations: the POWHEG method.** In: *JHEP*, **11:**  
 1931 (2007), p. 070. doi: [10.1088/1126-6708/2007/11/070](https://doi.org/10.1088/1126-6708/2007/11/070). arXiv: [0709.2092](https://arxiv.org/abs/0709.2092) [hep-ph] (see  
 1932 pp. 45, 48).
- 1933 [128] PAOLO NASON: **A New method for combining NLO QCD with shower Monte Carlo**  
 1934 **algorithms.** In: *JHEP*, **11:** (2004), p. 040. doi: [10.1088/1126-6708/2004/11/040](https://doi.org/10.1088/1126-6708/2004/11/040).  
 1935 arXiv: [hep-ph/0409146](https://arxiv.org/abs/hep-ph/0409146) [hep-ph] (see pp. 45, 48).
- 1936 [129] ANDREI V. GRITSAN, RAOUL RÖNTSCH, MARKUS SCHULZE, and MENG XIAO: **Constraining**  
 1937 **anomalous Higgs boson couplings to the heavy flavor fermions using matrix**  
 1938 **element techniques.** In: *Phys. Rev.*, **D94**:5 (2016), p. 055023. doi: [10.1103/PhysRevD.94.055023](https://doi.org/10.1103/PhysRevD.94.055023). arXiv: [1606.03107](https://arxiv.org/abs/1606.03107) [hep-ph] (see pp. 45, 48).
- 1940 [130] IAN ANDERSON et al.: **Constraining anomalous HVV interactions at proton and**  
 1941 **lepton colliders.** In: *Phys. Rev.*, **D89**:3 (2014), p. 035007. doi: [10.1103/PhysRevD.89.035007](https://doi.org/10.1103/PhysRevD.89.035007). arXiv: [1309.4819](https://arxiv.org/abs/1309.4819) [hep-ph] (see pp. 45, 48).
- 1943 [131] SARA BOLOGNESI, YANYAN GAO, ANDREI V. GRITSAN, et al.: **On the spin and parity of**  
 1944 **a single-produced resonance at the LHC.** In: *Phys. Rev.*, **D86:** (2012), p. 095031.  
 1945 doi: [10.1103/PhysRevD.86.095031](https://doi.org/10.1103/PhysRevD.86.095031). arXiv: [1208.4018](https://arxiv.org/abs/1208.4018) [hep-ph] (see pp. 45, 48).

- 1946 [132] YANYAN GAO, ANDREI V. GRITSAN, ZIJIN GUO, et al.: **Spin determination of single-produced resonances at hadron colliders.** In: *Phys. Rev.*, **D81**: (2010), p. 075022. doi: [10.1103/PhysRevD.81.075022](https://doi.org/10.1103/PhysRevD.81.075022). arXiv: [1001.3396 \[hep-ph\]](https://arxiv.org/abs/1001.3396) (see pp. 45, 48).
- 1947  
1948  
1949 [133] PIERRE ARTOISENET, RIKKERT FREDERIX, OLIVIER MATTELAER, and ROBBERT RIETKERK: **Automatic spin-entangled decays of heavy resonances in Monte Carlo simulations.** In: *JHEP*, **03**: (2013), p. 015. doi: [10.1007/JHEP03\(2013\)015](https://doi.org/10.1007/JHEP03(2013)015). arXiv: [1212.3460 \[hep-ph\]](https://arxiv.org/abs/1212.3460) (see p. 46).
- 1950  
1951  
1952  
1953 [134] V. KHACHATRYAN and ETAL: **Event generator tunes obtained from underlying event and multiparton scattering measurements.** In: *The European Physical Journal C*, **76**:3 (Mar. 17, 2016), p. 155. doi: [10.1140/epjc/s10052-016-3988-x](https://doi.org/10.1140/epjc/s10052-016-3988-x) (see p. 46).
- 1954  
1955  
1956 [135] RICHARD D. BALL et al.: **Parton distributions with LHC data.** In: *Nucl. Phys.*, **B867**: (2013), pp. 244–289. doi: [10.1016/j.nuclphysb.2012.10.003](https://doi.org/10.1016/j.nuclphysb.2012.10.003). arXiv: [1207.1303 \[hep-ph\]](https://arxiv.org/abs/1207.1303) (see p. 46).
- 1959 [136] YUE ZHANG, BO HUA LI, CHONG SHENG LI, JUN GAO, and HUA XING ZHU: **Next-to-leading order QCD corrections to the top quark associated with  $\gamma$  production via model-independent flavor-changing neutral-current couplings at hadron colliders.** In: *Phys. Rev.*, **D83**: (2011), p. 094003. doi: [10.1103/PhysRevD.83.094003](https://doi.org/10.1103/PhysRevD.83.094003). arXiv: [1101.5346 \[hep-ph\]](https://arxiv.org/abs/1101.5346) (see p. 47).
- 1960  
1961  
1962  
1963  
1964 [137] J ALWALL, R FREDERIX, S FRIXIONE, et al.: **The automated computation of tree-level and next-to-leading order differential cross sections, and their matching to parton shower simulations.** In: *JHEP*, **07**:arXiv:1405.0301. CERN-PH-TH-2014-064. CP3-14-18. LPN14-066. MCNET-14-09. ZU-TH 14-14 (May 2014), 079. 158 p. URL: <http://cds.cern.ch/record/1699128> (see p. 48).
- 1965  
1966  
1967  
1968  
1969 [138] RIKKERT FREDERIX and STEFANO FRIXIONE: **Merging meets matching in MC@NLO.** In: *JHEP*, **12**:arXiv:1209.6215. CERN-PH-TH-2012-247. ZU-TH 21-12 (Sept. 2012). Comments: 40 pages, 14 figures, 061. 40 p. URL: <http://cds.cern.ch/record/1481985> (see p. 48).
- 1970  
1971  
1972  
1973 [139] **CMS Monte Carlo Generator Group** (see pp. 48–49).
- 1974 [140] T. GEHRMANN, M. GRAZZINI, S. KALLWEIT, et al.:  **$W^+W^-$  Production at Hadron Colliders in Next to Next to Leading Order QCD.** In: *Phys. Rev. Lett.*, **113**:21 (2014), p. 212001. doi: [10.1103/PhysRevLett.113.212001](https://doi.org/10.1103/PhysRevLett.113.212001). arXiv: [1408.5243 \[hep-ph\]](https://arxiv.org/abs/1408.5243) (see p. 49).
- 1975  
1976  
1977  
1978 [141] A. HOECKER, P. SPECKMAYER, J. STELZER, et al.: **TMVA - Toolkit for Multivariate Data Analysis.** In: *ArXiv Physics e-prints*, (Mar. 2007). eprint: [physics/0703039](https://arxiv.org/abs/physics/0703039) (see p. 50).
- 1979  
1980 [142] R. BRUN and F. RADEMAKERS: **ROOT: An object oriented data analysis framework.** In: *Nucl. Instrum. Meth.*, **A389**: (1997), pp. 81–86. doi: [10.1016/S0168-9002\(97\)00048-X](https://doi.org/10.1016/S0168-9002(97)00048-X) (see p. 50).
- 1981  
1982  
1983 [143] A. MAYR, H. BINDER, O. GEFELLER, and M. SCHMID: **The Evolution of Boosting Algorithms - From Machine Learning to Statistical Modelling.** In: *ArXiv e-prints*, (Mar. 2014). arXiv: [1403.1452 \[stat.ME\]](https://arxiv.org/abs/1403.1452) (see p. 51).
- 1984  
1985  
1986 [144] OLAF BEHNKE, KEVIN KRONINGER, GREGORY SCHOTT, and THOMAS SCHORNER-SADENIUS: **Data Analysis in High Energy Physics: A Practical Guide to Statistical Methods.** 1st. Wiley-VCH, 2013 (see p. 51).

- 1989 [145] CHRISTIAN BÖSER, SIMON FINK, and STEFFEN RÖCKER: **Introduction to Boosted Decision Trees: A multivariate approach to classification problems.** Presented at the 'KSETA Doktoranden' workshop, Lauterbad. July 2014. URL: <https://indico.scc.kit.edu/indico/event/48/session/4/contribution/35/material/slides/0.pdf> (see p. 51).
- 1994 [146] SERGUEI CHATRCHYAN et al.: **Combined results of searches for the standard model Higgs boson in  $pp$  collisions at  $\sqrt{s} = 7$  TeV.** In: *Phys. Lett.*, **B710**: (2012), pp. 26–48. DOI: [10.1016/j.physletb.2012.02.064](https://doi.org/10.1016/j.physletb.2012.02.064). arXiv: [1202.1488 \[hep-ex\]](https://arxiv.org/abs/1202.1488) (see p. 52).
- 1997 [147] GLEN COWAN, KYLE CRANMER, EILAM GROSS, and OFER VITELLS: **Asymptotic formulae for likelihood-based tests of new physics.** In: *Eur. Phys. J.*, **C71**: (2011). [Erratum: *Eur. Phys. J.* C73,2501(2013)], p. 1554. DOI: [10.1140/epjc/s10052-011-1554-0](https://doi.org/10.1140/epjc/s10052-011-1554-0), [10.1140/epjc/s10052-013-2501-z](https://doi.org/10.1140/epjc/s10052-013-2501-z). arXiv: [1007.1727 \[physics.data-an\]](https://arxiv.org/abs/1007.1727) (see pp. 52–53).
- 2002 [148] **Observation of a new boson with a mass near 125 GeV.** Tech. rep. CMS-PAS-HIG-12-020. Geneva: CERN, 2012. URL: <https://cds.cern.ch/record/1460438> (see p. 52).
- 2005 [149] **Procedure for the LHC Higgs boson search combination in Summer 2011.** Tech. rep. CMS-NOTE-2011-005. ATL-PHYS-PUB-2011-11. Geneva: CERN, Aug. 2011. URL: [http://cds.cern.ch/record/1379837](https://cds.cern.ch/record/1379837) (see p. 52).
- 2008 [150] HIGGS WORKING GROUP: **Documentation of the RooStats based statistics tools for Higgs PAG.** Aug. 2017. URL: <https://twiki.cern.ch/twiki/bin/viewauth/CMS/SWGuideHiggsAnalysisCombinedLimit> (see p. 52).
- 2011 [151] LORENZO MONETA, KEVIN BELASCO, KYLE S. CRANMER, et al.: **The RooStats Project.** In: *PoS, ACAT2010*: (2010), p. 057. arXiv: [1009.1003 \[physics.data-an\]](https://arxiv.org/abs/1009.1003) (see p. 52).
- 2013 [152] GLEN COWAN, KYLE CRANMER, EILAM GROSS, and OFER VITELLS: **Asymptotic formulae for likelihood-based tests of new physics.** In: *The European Physical Journal C*, **71**:2 (Feb. 2011). DOI: [10.1140/epjc/s10052-011-1554-0](https://doi.org/10.1140/epjc/s10052-011-1554-0). arXiv: [1007.1727 \[hep-ph\]](https://arxiv.org/abs/1007.1727) (see p. 52).
- 2017 [153] THOMAS JUNK: **Confidence level computation for combining searches with small statistics.** In: *Nuclear Instruments and Methods in Physics Research Section A: Accelerators, Spectrometers, Detectors and Associated Equipment*, **434**:2 (1999), pp. 435–443. DOI: [https://doi.org/10.1016/S0168-9002\(99\)00498-2](https://doi.org/10.1016/S0168-9002(99)00498-2) (see p. 52).
- 2021 [154] AL READ: **Presentation of search results: the CL s technique.** In: *Journal of Physics G: Nuclear and Particle Physics*, **28**:10 (2002), p. 2693. URL: <http://stacks.iop.org/0954-3899/28/i=10/a=313> (see p. 52).
- 2024 [155] A. M. SIRUNYAN et al.: **Particle-flow reconstruction and global event description with the CMS detector.** In: *JINST*, **12**: (2017), P10003. DOI: [10.1088/1748-0221/12/10/P10003](https://doi.org/10.1088/1748-0221/12/10/P10003). arXiv: [1706.04965 \[physics.ins-det\]](https://arxiv.org/abs/1706.04965) (see pp. 56–60, 62).
- 2027 [156] R. FRÜHWIRTH: **Application of Kalman filtering to track and vertex fitting.** In: *Nuclear Instruments and Methods in Physics Research Section A: Accelerators, Spectrometers, Detectors and Associated Equipment*, **262**:2 (1987), pp. 444–450. DOI: [http://dx.doi.org/10.1016/0168-9002\(87\)90887-4](https://doi.org/10.1016/0168-9002(87)90887-4) (see p. 57).

- 2031 [157] PIERRE BILLOIR: **Progressive track recognition with a Kalman like fitting proce-**  
 2032 **dure.** In: *Comput. Phys. Commun.*, **57**: (1989), pp. 390–394. DOI: [10.1016/0010-4655\(89\)90249-X](https://doi.org/10.1016/0010-4655(89)90249-X) (see p. 57).
- 2034 [158] SERGUEI CHATRCHYAN et al.: **Performance of CMS muon reconstruction in  $pp$  col-**  
 2035 **lision events at  $\sqrt{s} = 7$  TeV.** In: *JINST*, **7**: (2012), P10002. DOI: [10.1088/1748-0221/7/10/P10002](https://doi.org/10.1088/1748-0221/7/10/P10002). arXiv: [1206.4071 \[physics.ins-det\]](https://arxiv.org/abs/1206.4071) (see p. 57).
- 2037 [159] W ADAM, R FRÜHWIRTH, A STRANDLIE, and T TODOROV: **Reconstruction of electrons**  
 2038 **with the Gaussian-sum filter in the CMS tracker at the LHC.** In: *Journal of Physics*  
 2039 *G: Nuclear and Particle Physics*, **31**:9 (2005), N9. URL: <http://stacks.iop.org/0954-3899/31/i=9/a=N01> (see p. 57).
- 2041 [160] **Performance of electron reconstruction and selection with the CMS detector in**  
 2042 **proton-proton collisions at  $\sqrt{s} = 8\text{TeV}$ .** In: *Journal of Instrumentation*, **10**:06 (2015),  
 2043 P06005. URL: <http://stacks.iop.org/1748-0221/10/i=06/a=P06005> (see p. 58).
- 2044 [161] **Electron and photon performance in CMS with the full 2016 data sample.** In: (Mar.  
 2045 2017). URL: <http://cds.cern.ch/record/2255497> (see pp. 58, 62, 64).
- 2046 [162] K. ROSE: **Deterministic annealing for clustering, compression, classification, re-**  
 2047 **gression, and related optimization problems.** In: *Proceedings of the IEEE*, **86**:11  
 2048 (Nov. 1998), pp. 2210–2239. DOI: [10.1109/5.726788](https://doi.org/10.1109/5.726788) (see p. 58).
- 2049 [163] WOLFGANG WALTENBERGER: **Adaptive Vertex Reconstruction.** Tech. rep. CMS-NOTE-  
 2050 2008-033. Geneva: CERN, July 2008. URL: <https://cds.cern.ch/record/1166320> (see  
 2051 p. 58).
- 2052 [164] ANDREAS KORNMAYER: **The CMS Pixel Luminosity Telescope.** Tech. rep. CMS-CR-  
 2053 2015-121. Geneva: CERN, June 2015. URL: <https://cds.cern.ch/record/2039978> (see  
 2054 p. 59).
- 2055 [165] **CMS Luminosity Measurements for the 2016 Data Taking Period.** Tech. rep. CMS-  
 2056 PAS-LUM-17-001. Geneva: CERN, 2017. URL: <http://cds.cern.ch/record/2257069>  
 2057 (see p. 59).
- 2058 [166] **Measurement of the inelastic proton-proton cross section at  $\sqrt{s} = 13$  TeV.** Tech.  
 2059 rep. CMS-PAS-FSQ-15-005. Geneva: CERN, 2016. URL: <https://cds.cern.ch/record/2145896> (see p. 60).
- 2061 [167] **Muon Identification and Isolation efficiency on full 2016 dataset.** In: (Mar. 2017).  
 2062 URL: <http://cds.cern.ch/record/2257968> (see pp. 60–61).
- 2063 [168] **Effective areas used for Summer16 samples.** 2017. URL: [https://indico.cern.ch/event/482673/contributions/2187022/%20attachments/1282446/1905912/talk\\_electron\\_ID\\_spring16.pdf](https://indico.cern.ch/event/482673/contributions/2187022/%20attachments/1282446/1905912/talk_electron_ID_spring16.pdf) (see p. 63).
- 2066 [169] MATTEO CACCIARI, GAVIN P. SALAM, and GREGORY SOYEZ: **The Anti-k(t) jet clustering**  
 2067 **algorithm.** In: *JHEP*, **04**: (2008), p. 063. DOI: [10.1088/1126-6708/2008/04/063](https://doi.org/10.1088/1126-6708/2008/04/063). arXiv:  
 2068 [0802.1189 \[hep-ph\]](https://arxiv.org/abs/0802.1189) (see p. 63).
- 2069 [170] **Jet algorithms performance in 13 TeV data.** Tech. rep. CMS-PAS-JME-16-003.  
 2070 Geneva: CERN, 2017. URL: <http://cds.cern.ch/record/2256875> (see p. 63).

- 2071 [171] V. KHACHATRYAN et al.: **Jet energy scale and resolution in the CMS experiment in**  
 2072 **pp collisions at 8 TeV.** In: *Journal of Instrumentation*, **12**:02 (2017), P02014. URL:  
 2073 <http://stacks.iop.org/1748-0221/12/i=02/a=P02014> (see pp. 65–66).
- 2074 [172] **Jet energy scale and resolution performances with 13TeV data.** In: (June 2016).  
 2075 URL: <http://cds.cern.ch/record/2160347> (see pp. 65–66).
- 2076 [173] THE CMS COLLABORATION: **Identification of b-quark jets with the CMS experiment.**  
 2077 In: *Journal of Instrumentation*, **8**:04 (2013), P04013. URL: <http://stacks.iop.org/>  
 2078 [1748-0221/8/i=04/a=P04013](http://1748-0221/8/i=04/a=P04013) (see p. 66).
- 2079 [174] **Identification of b quark jets at the CMS Experiment in the LHC Run 2.** Tech. rep.  
 2080 CMS-PAS-BTV-15-001. Geneva: CERN, 2016. URL: <http://cds.cern.ch/record/2138504> (see pp. 66, 68).
- 2082 [175] NAZAR BARTOSIK: **Diagram showing the common principle of identification of jets**  
 2083 **initiated by b-hadron decays.** 2016. URL: [http://bartosik.pp.ua/hep\\_sketches/btagging](http://bartosik.pp.ua/hep_sketches/btagging) (see p. 67).
- 2085 [176] **Identification of b quark jets at the CMS Experiment in the LHC Run 2.** Tech. rep.  
 2086 CMS-PAS-BTV-16-001. unpublished. Geneva: CERN, 2017 (see pp. 68–69).
- 2087 [177] **Performance of missing energy reconstruction in 13 TeV pp collision data using**  
 2088 **the CMS detector.** Tech. rep. CMS-PAS-JME-16-004. Geneva: CERN, 2016. URL:  
 2089 <http://cds.cern.ch/record/2205284> (see pp. 69, 74–75).
- 2090 [178] JORDAN DAMGOV: **Missing Et Optional Filters Run 2.** 2017. URL: <https://twiki.cern.ch/twiki/bin/viewauth/CMS/MissingETOptionalFiltersRun2> (see p. 74).
- 2092 [179] **EGM corrections for Moriond17.** URL: [https://indico.cern.ch/event/613162/contributions/2472046/attachments/1410308/2156822/EGMSmearerAndRegression\\_PPD\\_022017.pdf](https://indico.cern.ch/event/613162/contributions/2472046/attachments/1410308/2156822/EGMSmearerAndRegression_PPD_022017.pdf) (see p. 79).
- 2095 [180] **Misalignment and Muon Scale corrections.** URL: [https://www-cdf.fnal.gov/~jyhan/cms\\_momscl/rochcor\\_cmsnote.pdf](https://www-cdf.fnal.gov/~jyhan/cms_momscl/rochcor_cmsnote.pdf) (see p. 80).
- 2097 [181] **Rochestor Correction.** Accessed: 2017-05-20. URL: <https://twiki.cern.ch/twiki/bin/viewauth/CMS/RochcorMuon> (see p. 80).